UC San Diego

UC San Diego Electronic Theses and Dissertations

Title

Manipulation of Magnetic Textures in Thin Films and Devices

Permalink

https://escholarship.org/uc/item/87h5908s

Author

Tolley, Robert Douglas

Publication Date

2017

Supplemental Material

https://escholarship.org/uc/item/87h5908s#supplemental

Peer reviewed|Thesis/dissertation

eScholarship.org Powered by the California Digital Library
University of California

UNIVERSITY OF CALIFORNIA, SAN DIEGO

Manipulation of Magnetic Textures in Thin Films and Devices

A dissertation submitted in partial satisfaction of the requirements for the degree Doctor of Philosophy

in

Electrical Engineering (Nanoscale Devices and Systems)

by

Robert Douglas Tolley

Committee in charge:

Professor Eric Fullerton, Chair
Professor Drew Hall
Professor Zhaowei Liu
Professor Vitaliy Lomakin
Professor Donald Sirbuly

2017

©

Robert Douglas Tolley, 2017

All rights reserved.

The Dissertation of Robert Douglas Tolley is approved, and it is acceptable in quality and form for publication on microfilm and electronically:

_____

_____

_____

_____

_____

Chair

University of California, San Diego

2017

DEDICATION

To all of us who have or will.

TABLE OF CONTENTS

SIGNATURE PAGE iii

DEDICATION iv

TABLE OF CONTENTS v

LIST OF ABBREVIATIONS vii

LIST OF SUPPLEMENTAL FILES viii

LIST OF FIGURES ix

PREFACE xiii

ACKNOWLEDGEMENTS xiv

VITA xv

ABSTRACT xvii

Chapter 0: Magnetism and Magnetic Materials 1

Chapter 0, Section 1: Sources and Interactions of Magnetism 4

Chapter 1: Magnetic Materials And How To Grow Them. 19

Chapter 1, Section 1: Fullerton Lab Sputter Equipment 20

Chapter 1, Section 2: Sputtering Background 22

Chapter 1, Section 3: Lithography and Patterning Processes 31

Chapter 2: Measurement Techniques and Methods 35

Chapter 2, Section 1: Vibrating Sample Magnetometry 36

Chapter 2, Section 2: Magneto-Optical Kerr Microscopy 42

Chapter 2, Section 3: Evico Magnetics Kerr Effect Microscope 48

Chapter 2, Section 4: A Mathematical Basis for Kerr Microscopy 49

Chapter 2, Section 5: Kerr Microscopy Imaging Techniques. 58

Chapter 3: You, Me, and Co-Tb. 64

Chapter 3, Section 1: Alloy to Multilayer Transition and Properties 67

Chapter 3, Section 2: Thermal Domain Wall Propagation 76

Chapter 3, Section 4: CoTb in Review 85

Chapter 4: The Wonderful Wizard of Os. 87

Chapter 4, Section 1: Probing DMI via Asymmetric Domain Wall Growth 96

Chapter 4, Section 2: Novel Behavior of Pt/Co/Os2A/Pt 108

Chapter 4, Section 4: Tracking Nucleation Dynamics of Current-Forced Skyrmions 125

Chapter 4, Section 5: Theories of Stripe to Skyrmion Transition 139

Chapter 4, Section 6: Skyrmions in Review 144

Special Section 1: 3D Printing in Instrumentation Applications 146

Special Section 1, Subsection 1: Design and Fabrication of Kerr Microscope Pulser 148

Special Section 2: Lithography Mask Design 152

Conclusion: 157

Special Section X: Quick Reference Card 158

THANKS TO THE READER 159

BIBLIOGRAPHY 160

LIST OF ABBREVIATIONS

AOS: All Optical (magnetization) Switching

AO-HDS: (All Optical Helicity Dependent (magnetization) Switching

DMI: Dzyaloshinskii-Moriya Interaction

HAMR: Heat Assisted Magnetic Recording

MAMR: Microwave Assisted Magnetic Recording

MOKE: Magneto Optic Kerr Effect

PMA: Perpendicular Magnetic Anisotropy

PPMS: Physical Property Measurement System

RHEED: Reflection High-Energy-Electron-Diffraction

RKKY: Ruderman–Kittel–Kasuya–Yosida

STT: Spin Transfer Torque

SOT: Spin Orbit Torque

VSM: Vibrating Sample Magnetometry

XRD: X-Ray Diffraction

XRR: X-Ray Reflectivity

LIST OF SUPPLEMENTAL FILES

Supp Video 1 – CoTb Domain Wall Motion

Supp Video 2 – PtCoOsPt Stripe Phase

Supp Video 3 – PCoOsPt Skyrmions in close paced lattice

Supp Video 4 – PtCoOsPt Skyrmions at low (0,5mA) drive

Supp Video 5 – PtCoOsPt Skyrmions at high (4mA) drive

Supp Video 6 – PtCoOsPt Skyrmions at high (4mA) drive inverted field

Supp Vidoe 7 – PtCoOsPt Skyrmions in full film hopping motion

Supp Video 8 – PtCoOsPt Skyrmions in full film stripe breaking

LIST OF FIGURES

Figure 1: Families of magnetic materials and their responses to external magnetic field. 6

Figure 2: DMI acting across the "third" atom. 8

Figure 3: Easy / hard axis illustration for a cubic structure. 10

Figure 4: Magnetic domain walls in a material. 15

Figure 5: Kittel calculation of multi-domain state configurations and their energies. 16

Figure 6: Example Kerr microscopy images showing magnetic domains and contrast. 18

Figure 7: ATC Orion sputter tool by AJA International. 20

Figure 8: Cross sectional view of sputter gun. 22

Figure 9: Schematic of deposition of material. 24

Figure 10: Roughness due to lattice shift. 25

Figure 11: Incident B atom disrupts deposited A specie. 25

Figure 12: Deposition on layer of different spacing. 26

Figure 13: Roughness as caused by lattice mismatch. 26

Figure 14: Raw X-Ray Reflectivity curve for thick Silicon calibration sample. 29

Figure 15: Negative resist lithography process. 31

Figure 16: Process of sputter deposition and lift-off. 32

Figure 17: Positive photoresist etch process. 33

Figure 18: Quantum Design Versalab with Vibrating Sample Magnetometer module. 38

Figure 19: Mounting of a VSM sample in the plastic straw. 39

Figure 20: Data before (black) and after (red) diamagnetic subtraction. 40

Figure 21: Representation of Polar, Longitudinal and Transverse MOKE. 45

Figure 22: Example Kerr microscopy image showing background and subtraction. 58

Figure 23: Example Kerr microscopy image showing subtraction of lithography features. 59

Figure 24: Example of Kerr microscopy image showing magnetization in lithography feature.. 59

Figure 25: Effect of motion of the sample stage. 61

Figure 26: Aberrant signal from a non-magnetic silicon sample. 62

Figure 27: Optically Induced Switching ranges in CoTb films. 65

Figure 28: Alloy to multilayer transition example. 68

Figure 29: VSM data showing CoTb edge deposition effect. 69

Figure 30: VSM moment versus field for $Co_{78}Tb_{22}$ alloy sample. 71

Figure 31: VSM moment versus temperature for a Co87%, Tb12% multilayer. 72

Figure 32: Finding compensation temperature from selected shoulder moments. 73

Figure 33: Compensation temperature (T_M) versus layer thickness for $Co_{76}Tb_{24}$. 73

Figure 34: Helicity dependent movement of domain wall in Pt/$[Co/Pt]_{x3}$/Pt. 75

Figure 35: Current application movement of thermal gradient in 2μm $Co_{78}Tb_{22}$ alloy device. ... 77

Figure 36: Three regions approximation. 78

Figure 37: Nucleation and annihilation behavior versus field and heating. 79

Figure 38: Formation / Annihilation curves for Sample 1. 80

Figure 39: Additional test geometries and curves. 82

Figure 40: Controllable placement of domain wall using thermal gradients. 83

Figure 41: Basic racetrack memory schematic. 88

Figure 42: Two types of skyrmion. 90

Figure 43: Symmetry breaking of a Néel wall. 98

Figure 44: Symmetry-broken domain wall propagation in Pt/Co/Ir/Pt. 99

Figure 45: Finding asymmetry in one direction for Pt/Co/Os0.1nm/Pt. 100

Figure 46: Coilset systems for symmetry breaking measurement. 101

Figure 47: Asymmetry in all 4 field pairings for Pt/Co/Pt and Pt/Co/Os0.1nm/Pt..... 102

Figure 48: Domain walls at room temperature for Pt/Co/Os/Pt films. 104

Figure 49: VSM magnetometry loops for various Pt/Co/Os/Pt films..... 105

Figure 50: OOP VSM magnetometry data showing saturation moment for Pt/Co/Os/Pt films. 106

Figure 51: VSM saturation moment versus temperature for standard and invert layers. 107

Figure 52: Field-induced stripe collapse to skyrmions in Os=0.2nm films..... 108

Figure 53: Collapse of stripe phase to close-packed skyrmion lattice at room temperature. 109

Figure 54: Out of plane VSM loops for Pt/Co/Os0.2nm/Pt around the skyrmion transition..... 110

Figure 55: Magnetization and domain behavior of Pt/Co/Os0.2nm/Pt. 112

Figure 56: Tracking a skyrmion path..... 116

Figure 57: Field induced nucleation of skyrmions from saturated film over time. 117

Figure 58: Two methods of lithographically defining geometry..... 119

Figure 59: Skyrmion propagation in 20 micrometer hall crosses..... 121

Figure 60: Velocity of skyrmions in 20 micrometer hall cross versus applied current density.. 122

Figure 61: Observation of skyrmion chirality-based deflection. 123

Figure 62: Skyrmions in 100 micrometer hall cross lead, patterned by etching..... 126

Figure 63: Population and density of skyrmions at low (0.5mA) current. 127

Figure 64: Velocity tracking of skyrmions. 129

Figure 65: Example current induced nucleation of at multiple current amplitudes..... 130

Figure 66: Current nucleated behavior for an applied current of 4mA..... 131

Figure 67: Skyrmion Hall alignment of different chirality of skyrmions..... 134

Figure 68: Stripes and skyrmions formed from defect site (tip of orange triangle). 135

Figure 69: Skyrmion tracking at -0.9 Oe across application of current. 136

Figure 70: Current induced nucleation of skyrmions during the application of current. 137

Figure 71: Field based collapse of stripes to skyrmions. 138

Figure 72: Stripe phase collapsing into skyrmions due to field. 139

Figure 73: Stripe collapse as driven by population density. 140

Figure 74: Transverse stripe shattering in open film. 141

Figure 75: Pulse coil setup (center) installed in Evico Magnetics in-plane coilset. 149

Figure 76: Pulse coil system for the Kerr microscope. 150

Figure 77: Standard large hall crosses for transport measurement. 152

Figure 78: Small hall crosses for confined geometries and VSM sized samples. 153

Figure 79: Angled lithography mask geometry for membrane design. 154

Figure 80: Sample thermal gradient chokes. 155

PREFACE

“The nation that controls magnetism will control the universe”

-Dick Tracy

ACKNOWLEDGEMENTS

I would like to acknowledge all of those who have made this work possible. Without their support, this document and the work it represents would not exist. Thank you to my family, those of blood and those of history. Thank you to the Fullerton group members, those old and those new. Thank you to my friends, those near and far.

I am here,

this is here,

because of you.

Chapter 3 in part is taken from research published as "Generation and manipulation of domain walls using a thermal gradient in a ferrimagnetic TbCo wire." R. Tolley, T. Liu, Y. Xu, S. Le Gall, M. Gottwald, T. Hauet, M. Hehn, F. Montaigne, E. E. Fullerton, and S. Mangin in Applied Physics Letters 106, 242403 (2015). The dissertation author was the primary investigator and author of this paper.

Chapter 4 in part is taken from research submitted to be published as "Room-temperature observation and current control of skyrmions in Pt/Co/Os/Pt thin films." R. Tolley, S. A. Montoya, and E. E. Fullerton in Physical Review Materials, (ML10007), and is currently under review. The dissertation author was the primary investigator and author of this paper.

VITA

Educational Experience

- 2017 – University of California, San Diego in San Diego, CA.
  - PhD Electrical Engineering (Nanoscale Devices and Systems)

- 2013– PhD research exchange at Institut Jean Lamour in Nancy, France.

- 2012 – Miami University in Oxford, Ohio.
  - M.S. Physics.

- 2010 – Miami University in Oxford, Ohio.
  - Bachelor of Arts Physics and East Asian Languages & Culture.
  - Cum Laude, University Honors w/Distinction.

Conference Presentations

- 2017 – Oral presentation at 2017 MMM, Pittsburgh
  - Current Driven Skyrmions In Pt/Co/Os/Pt Thin Films

- 2016 – Oral presentation at 2016 MMM, New Orleans
  - Observation of DMI and Skyrmions in Pt/Co/Os/Pt thin films

- 2016 – Poster presentation at 2016 joint MMM / INTERMAG, San Diego
  - Nitrogen Reactive Sputtering of (Co70Fe30)(1-X)NX for Write Pole Shields

- 2015 – Oral presentation of work given by S. Mangin at 2015 INTERMAG, Beijing
  - Control and Generation of Domain Walls Near Magnetic Compensation in Ferrimagnetic CoTb via Applied Thermal Gradient

- 2014 – Oral presentation at MMM, Honolulu
  - Control and Generation of Domain Walls Near Magnetic Compensation in Ferrimagnetic CoTb via Applied Thermal Gradient.

- 2014 – Poster presentation at 2014 MSNOWS conference in Nancy, France
  - Generation and Manipulation of Domain Walls Using a Thermal Gradient in a Ferrimagnetic CoTb Wire.

- 2014 – Oral presentation at INTERMAG, Dresden, Germany
  - Generation and Control of Domain Walls using a Thermal Gradient in Ferrimagnetic CoTb Thin Films.

- 2012 – Oral presentation at INTERMAG, Vancouver, Canada

- Independent Magnetization Switching and Magnetoresistance in a Bilayer of Two Ferromagnetic Materials without a Non-magnetic Spacer

Papers

- 2017 – R. Tolley, S. A. Montoya, and E. E. Fullerton. Room-temperature observation and current control of skyrmions in Pt/Co/Os/Pt thin films. Physical Review Materials, (arXiv 1711.07101), under review.

- 2015 –Generation and manipulation of domain walls using a thermal gradient in a ferrimagnetic TbCo wire. R. Tolley, T. Liu, Y. Xu, S. Le Gall, M. Gottwald, T. Hauet, M. Hehn, F. Montaigne, E. E. Fullerton, and S. Mangin. Appl. Phys. Lett. 106, 242403 (2015).

- 2013 – Conductance quantization: A laboratory experiment in a senior-level nanoscale science and technology course. R. Tolley, A. Silvidi, C. Little, and K. F. Eid. American Journal of Physics, January 2013. Volume 81, Issue 1, pp. 14.

ABSTRACT OF THE DISSERTATION

Manipulation of Magnetic Textures in Thin Films and Devices

by

Robert Douglas Tolley

Doctor of Philosophy in Electrical Engineering (Nanoscale Devices and Systems)

University of California, San Diego, 2017

Professor Eric Fullerton, Chair

Control and manipulation of magnetic textures is promising for the development of next-generation data storage, memory and processing technologies. Towards this goal, domain wall manipulation in two materials systems are presented here and thoroughly evaluated. Domain walls in ferrimagnetic Cobalt-Terbium alloys and multilayers are created, moved and stabilized via thermal gradients and a static magnetic field and exploit the unique properties of the system across the magnetic compensation point. The response of the systems to thermal gradients is observed via Kerr microscopy and used to determine the positioning of domain walls within patterned devices. Magnetic skyrmions are discovered in thin-film multilayered stacks using an Pt/Co/Os/Pt

heterostructures where the thin Osmium layer is used to break interfacial symmetry and enhance the Dzyaloshinskii-Moriya interaction. The resulting skyrmions are manipulated using temperature, magnetic field, and electric current, and special attention is paid to their motion and nucleation behavior. Skyrmions are observed to be formed by low applied currents from nucleation sites and by collapse of stripe textures. Patterned wires allow for the observation of skyrmion nucleation behavior in free space, as well as defect sites, and real-time Kerr microscopy imaging is presented of skyrmion and stripe dynamics. These systems are evaluated from a perspective of their growth, patterning, measurement, and the novel behavior of the magnetic textures.

Chapter 0:
Magnetism and Magnetic Materials

Magnetic materials first gained interest for their novelty. A lodestone behaved strangely compared to other common rocks – attracting iron and orienting itself within the Earth's magnetic field. Lodestone compasses and needle compasses for navigation were the first major uses of the phenomenon. At the dawn of the electrical age, the ability of magnetism to affect its partner field led to the generation of electricity and a boom in both power generation and signal transmission. The information age grew upon the speed of electronic synapses, but magnetism filled the need for memory and storage. Now as information becomes more and more dense and processing becomes more and more powerful, there is additional need for new materials and novel interactions to drive the future forward. This dissertation will detail the work done by Robert Tolley over the course of his 5-year study of the fabrication of ferrimagnetic and ferromagnetic layers, imaging of magnetic domain patterns within those materials, and control over the formation and propagation of these magnetic textures with external stimulus. Work composed primarily of domain wall manipulation in ferrimagnetic Cobalt-Terbium alloys and multilayers, as well as the formation and manipulation of skyrmions in ferromagnetic Pt/Co/Os/Pt thin magnetic multilayers.

The study of magnetic materials exists at several critical length scales. [1] At the shortest of length scales, individual electrons and their motion form the basis of magnetism. Electron spin and orbit interactions within an atom determine not only the atom's structure, but also the magnetic state of that atom. At tenths of nanometers (an atom's spacing) the exchange interaction governs the behavior of adjacent atomic moments, coupling neighboring atoms together. At slightly longer length scales, the Ruderman–Kittel–Kasuya–Yosida (RKKY) [2] interaction couples conduction

spin moments over the range of several nanometers to several tens of nanometers At those ranges and longer, the magnetostatic exchange links the behavior of the magnetic moments with the field that they create – giving rise to shape terms depending on the structure of the material. The emergent behavior of magnetism is due to a rich interplay of atomic, orbital, lattice, structural and shape terms with control over these terms of significant importance to the manipulation of spin, charge and moment.

Magnetism at the mesoscale is due to the interaction of charge and spin in strongly correlated systems [3] [1]. This ordering, driven at several length scales by the interactions of spin, electrons and the crystal lattice, can be affected in a myriad of ways. Layers of different materials may perform differently than their bulk systems might suggest. Materials that would otherwise be non-magnetic on their own can be influenced by proximity effects of thin layers, or two magnetic materials may align antiferromagnetically to change the resulting behavior of their alloy. Growth of one layer on top of another may lead to stress and strain due to lattice mismatch. Due to the process of growth, an inverted layer stack may display significantly different properties than the original growth direction.

Coupling between atoms and layers is a prime area for the development of new material properties. In this modern world, new materials are needed to create, transport, process and store data. The emergence of magnetic properties that exist at fast timescales, or small arrangements of magnetism in domain wall textures and skyrmions offer the potential for novel data manipulation technologies. Domain wall logic and memory devices have been proposed, and some of the first commercial magnetic random-access memory has recently been produced. These systems are incredibly complex, and rely upon a delicate manipulation of material and structural properties.

At its basis, magnetism is a result of the movement of charged particles. Each atom is composed of protons, neutrons, and electrons. While the nucleons at the center of an atom create a small field, the moving electrons in the outermost shell are by far the greater source of atomic magnetism. Each electron has its own gyroscopic spin, and orbits the center of the atom at a prescribed energy level. Traversing the periodic table, correspondingly more electrons orbit an atom as its nuclear core size increases. These electrons occupy specific orbital, given by their distribution, angular momentum and the occupied energy levels below them. As electrons are fermions, no two electrons with the same spin can occupy the same orbital. As each electron possesses either a +1/2 or a -1/2 spin, it is possible for two electrons of different spins to occupy the same level. According to the Hund rule, electrons will first occupy the available empty shells, and only when the empty shells are occupied with one spin will the shells begin to fill with the other spin [4]. The existence of unpaired electrons in the outermost shells will give rise to a net angular and orbital motion of that atom, and atomic scale magnetism.

While any individual atom may be itself magnetic, the long-range order of many spins create the basic forms of magnetic materials. Magnetic systems (and even “non-magnetic systems”) are described on the basis of two types of order – how they order in response to their own structure and inherent field, and how they behave under the application of an external magnetic field. Several different general classifications of system exist: diamagnetism, paramagnetism, ferromagnetism, antiferromagnetism and ferrimagnetism all describe the net behavior of a magnetic system. These are driven by a rich series of interactions, which will be addressed in overview here.

Chapter 0, Section 1:
Sources and Interactions of Magnetism

There are several different broad classes of magnetic material, described by their behavior alone and in a magnetic field. Diamagnetism and diamagnetic materials order in opposition to an external magnetic field, and experience no magnetic ordering on their own. Ferromagnetic, ferrimagnetic, and antiferromagnetic materials all order internally on their own, but respond to an external field differently. Paramagnetic materials are disordered on their own, but can be brought into order by an external magnetic field. These general families of magnetic behavior can be applied to cover the net behavior of systems large and small.

The source of diamagnetism comes from the orbit of the electrons around the nucleus. When exposed to an external magnetic field, an electron orbiting the nucleus will experience a Lorentz force of $F = q\vec{V} \times \vec{B}$ [5]. For electrons of different orbital direction, this will result in their orbits either being pushed toward the nucleus, or pulled away from the nucleus. As this orbit is either expanded or reduced, the magnetic field created by the orbiting electron will be lowered or increased, respectively. While present in all systems, this effect is only truly observable in the absence of unpaired spins (the source of paramagnetism). For purely diamagnetic systems there are no unpaired electrons in the material, so it lacks any other more dominant magnetic response. Thus, for a purely diamagnetic material it will have no magnetic moment of its own. When put in an external magnetic field, a diamagnetic material will generate a small magnetic field opposite to the external magnetic field. While this orbital response is present in all materials, it is much smaller than any other effect, and is only observable in purely diamagnetic systems.

Paramagnetic materials are different from diamagnetic materials in that they have an unpaired electron that creates its own magnetic field. Thus, for a paramagnetic system, these moments will tend to align themselves in an external magnetic field. This effect enhances the external magnetic field, if one is present. However, a paramagnetic system lacks any form of internal order imposed by shape, crystal lattice or other parameters. Therefore, the disordered alignment of the individual moments of the system produces no net magnetic effect of the paramagnetic object, unless ordered by an external magnetic field.

Ferromagnetic systems have the unpaired atomic spins of the paramagnetic systems, but also tend to orient their spins with respect to each other. Interactions between neighboring spins creates a net order to the system, even in the absence of an externally applied field. Thus, a ferromagnetic object will typically have some magnetic field of its own, or will have a residual magnetic orientation after being aligned in an external field even if that field is removed.

Antiferromagnetic systems behave analogously to ferromagnetic systems, but where the order of a ferromagnetic system will attempt to align adjacent spins parallel, the order of an antiferromagnetic system will align adjacent spins antiparallel. This will result in a net zero magnetic moment of the material, even though the individual spins will have a magnetic moment.

Ferrimagnetic systems exist as a pairing of two spin systems that are antiferromagnetically aligned. A ferrimagnet will express a long range order, with atoms of each sublattice aligned parallel to that sublattice, however the two sublattices are aligned opposite to each other. Thus, a ferrimagnetic system will appear to behave similarly to a ferromagnetic system, having a net moment in the absence of external field, and aligning to an external field. However, due to the two oppositely aligned and competing magnetic orders within the material, the net moment from a ferrimagnetic system will be lower than that of the system if it had ferromagnetic order.

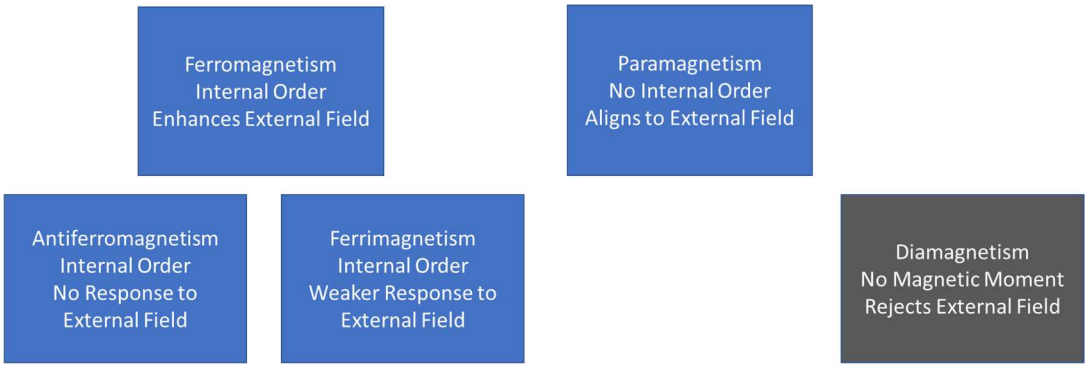

Figure 1: Families of magnetic materials and their responses to external magnetic field.

Magnetic materials themselves are described by how they order in response to their own internal energies and any applied external field. These internal interactions are rich and varied, and their strength is determined by the materials, and their structure both local and large scale. In general, the four major families of interaction are related to the four energies of the system. Each will seek to minimize the total energy of the system with respect to its orientation. These four major interactions are: Zeeman energy, Dipole energy, Anisotropy energy and Exchange interaction. The sum of these interactions will determine the local and far ranging order of the system.

The exchange interactions are the basic source of magnetic order. It will seek to align the individual atomic magnetic moments either parallel or antiparallel to each other. Electrons with spin ½ are subject to Pauli exclusion – which prevents two electrons with the same spin from occupying the same orbit in the electron shell. For the example of two atoms with a single electron each, if the atoms are sufficiently close that their electron waveforms overlap, these electrons will interact. If the atoms are close enough that the Coulomb interaction is minimal, this will force the two electrons into the same waveform such that they are prevented from having the same spin. This gives rise to antiferromagnetic or diamagnetic order of the sample by either forming paired spins (diamagnetism) or by aligning the spins in the opposite direction (antiferromagnetism). This

is what gives a hydrogen molecule (H_2) its diamagnetism. For systems where the atomic cores are sufficiently far apart, the electrons will instead align parallel – giving rise to ferromagnetic order. Depending primarily on the distance of one atomic core from another and the overlap of the wave functions of those electrons, the exchange interaction can be either positive, negative, or zero. Positive interactions (as in cobalt), will result in the system being ferromagnetic, while negative interactions (as in manganese or chromium) will result in antiferromagnetic order. The energy term for the exchange interactions is $E = -J_{ex}\vec{S}_1 \cdot \vec{S}_2$, with $\vec{S}$ describing the vector orientation of the spin, and J_{ex} describing the strength of the exchange interaction between those two orbits. As can be seen from the energy statement, a positive J_{ex} will result in a minimization of the energy when the neighboring moments are parallel aligned (ferromagnetism), and for a negative J_{ex}, this energy will minimize with antiparallel moments giving rise to antiferromagnetic order.

The exchange interaction presented above is complicated slightly when describing materials with little direct overlap between electron shells. In the case of metals, a cloud of electrons is shared freely among the atoms in the lattice. An individual magnetic ion creates a spin polarization in the nearby conduction electrons. This electron sharing gives rise to an interaction with a wider reach than the direct exchange picture as the electrons move from atom to atom. Indirect exchange also known as RKKY interaction, creates a coupling similar to the direct exchange, but that oscillates across the lattice of neighboring atoms [2]. This oscillatory coupling starts positive and decays with distance, and is capable of creating ferromagnetic or antiferromagnetic alignment based on the separation of the two linked atoms. This produces a longer range interaction than just the direct exchange.

As a special case of the exchange interaction that will become useful later, the Dzyaloshinskii-Moriya interaction (DMI) or (DM interaction) involves two competing

interactions [6] [7]. With the direct exchange linking two magnetic atoms, the addition of a third atom that is linked to the other two may complicate the picture. Instead of involving nearest-neighbor interactions, this will add an additional term that describes the coupling of two atoms across the intermediary. Where the direct exchange term is $E = -J_{ex}\vec{S}_1 \cdot \vec{S}_2$ that acts to drive spins either parallel or antiparallel, the expression for DMI creates an effective field $H_{DM} = D_{1,2} \cdot \left(\vec{S}_1 \times \vec{S}_2\right)$ that will seek to align the two atoms at 90 degrees (cross) to each other. The sign of the DM interaction also determines at which orientation (right or left) the system would prefer to orient the spins. As will be seen later, this gives rise to a "handedness" or chiral nature where the magnetic system would prefer to wind the spins in the same orientation.

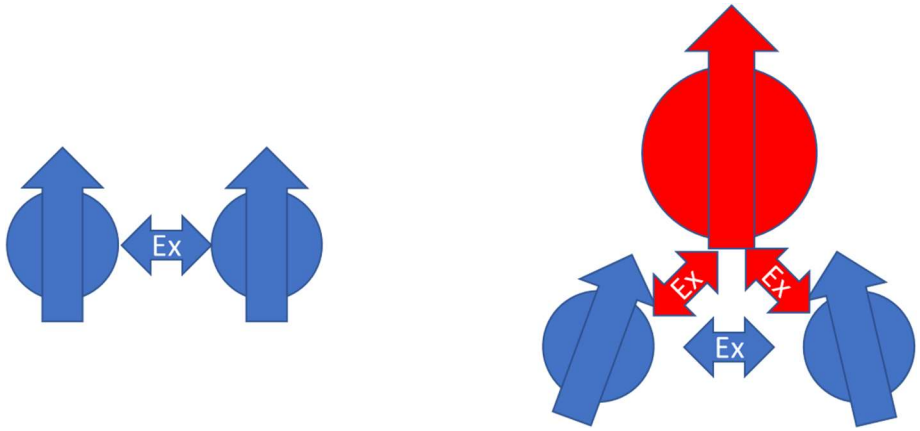

Figure 2: DMI acting across the "third" atom. The exchange interaction (left) aligns the two atoms to each other, but when involving a strong spin-orbit coupling material (right), the additional interactions will cause the system to cant with respect to each other.

With magnetic materials describes by how atomic moments order to themselves and applied external field, the Zeeman energy term is the next to be evaluated. This represents the energy of a magnetic object within an external applied magnetic field. With an energy term taken over volume V of: $E_{Zeeman} = -\mu_0 \int_V \vec{M} \cdot \vec{H}_{applied} dV$, where $\vec{M}$ is the magnetization of the material and $\vec{H}$ is an external magnetic field. This energy is minimized for paramagnetic, ferromagnetic and ferrimagnetic systems when the magnetization of the material is aligned to the

external applied magnetic field. For magnetic systems, a common way of switching their magnetic state is by the application of an external magnetic field. A magnetic material that is not aligned to the external magnetic field will experience some torque, which if it overcomes the anisotropy terms of the material, may result in the magnetic orientation switching.

Magnetic anisotropy terms deal with the preferential ordering of the magnetic material along certain directions. These terms may be due to the long range crystal structure of the material, the shape of the magnetic object, tension or strain acting on the lattice, or interaction of multiple different layers of the system. The typical expression of the energy per volume is as:

$$E_K = V(K_1(\alpha_1^2\alpha_2^2 + \alpha_2^2\alpha_3^2 + \alpha_3^2\alpha_1^2) + K_2(\alpha_1^2\alpha_2^2\alpha_3^2 + \cdots) + \cdots$$

Where K_1 corresponds to the first order term of the anisotropy, K_2 to the second order and so on. The most common case of anisotropy is a uniaxial one where only the first order term of the anisotropy will be left, the others being either inexistent either neglected. In that case a magnetic system with sufficient magnetic anisotropy will exhibit a preferred axis for spontaneous magnetic order (known as the easy axis). This is one of the sources of large-scale long range order in the system as the spins order along the (or one of the) easy axis for the system. [1]

Magnetocrystalline anisotropy is due to the orientation of the atomic lattice within the material. The electrons within the crystal lattice are shaped by spin-orbit interactions and align along the bonding directions within the lattice. Taking as an example the primitive cubic or body-centered-cubic type of crystal lattice, the magnetization will have a preferential alignment along the lattice toward the nearest-neighbor. This would correspond to having an easy axis along any of the Miller indicies oriented in the (100), (010) or (001) directions, and a hard axis along (110), (101) or (011) directions. The easy axis indicates the preferred crystallographic orientation for the

material's magnetization. A system may have multiple easy axes, or a more complicated orientation of the crystalline direction, but for systems that exhibit long-range crystalline order, the easy axis will typically lie along one of the crystal axes. One important factor for the magnetocrystalline anisotropy is for the system to have sufficient crystalline order to generate long range order of spins. Systems may be crystalline (with large scale order), polycrystalline with many microscopic crystals that do not necessarily share an order, or amorphous (in which no long-range periodic structure exists).

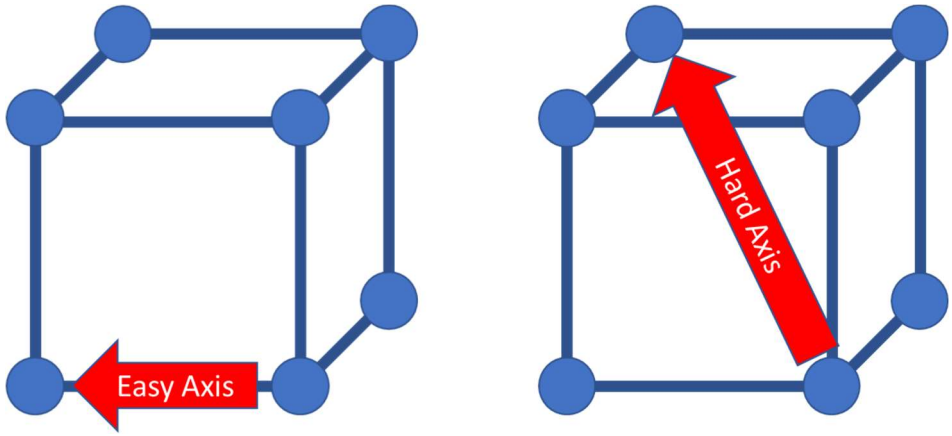

Figure 3: Easy / hard axis illustration for a cubic structure.

So far, discussion has primarily dealt with systems without regard to their shape. However, there is a significant effect from the shape of the object into which the magnetic material has been patterned. For a non-infinite object with uniform magnetization, there will north poles at one end of the object and south poles at the other. If taken as an internal picture, from the north poles at one end to the south pole at the other, there will be an effective internal field that acts to demagnetize the system. This demagnetizing field inside the material acts to reduce the magnetization within the sample, and can reorient the magnetic structure of the system to a more favorable direction. Take for example, a spherical magnetic particle with a uniform magnetization – it will produce an internal demagnetizing field that is the same no matter in which direction along

the sphere it is oriented. However, if that sphere were stretched to a cylindrical wire, there would be two potential axes – either along the wire or perpendicular to it. For this case, instead of the isotropic sphere, there would be an easy axis along the wire, and a hard axis perpendicular to the wire – an anisotropic system. H_{demag} can be expressed as a tensor of the form:

$$\vec{H}_{demag} = -4\pi\bar{\bar{N}}.\vec{M}$$

$\bar{\bar{N}}$ is a tensor of the second order depending of the form of the magnetic material. The energy associated to this field is homogeneous with the anisotropy energy so it is common to gather them into the same term called effective anisotropy that is decisive for the orientation of the magnetization in the ground state.

A special, but critical example of the shape anisotropy lies in the thin film case. For a sufficiently thin plate, there will be the easy plane (in-plane) and the hard axis (perpendicular to the plane). The demagnetizing energy of this system will be as $E_{demag} = \frac{1}{2}\mu_0 M^2 \sin^2\theta$ where M is the magnetization, and θ is the angle between the film surface and the magnetization. Thus, for a sample of magnetization M, there will be a demagnetizing field of the strength $K_u = \frac{1}{2}\mu_0 M^2$. The system will attempt to pull the magnetization of the system in-plane. However, magnetic layers with perpendicular magnetic anisotropy are critical to the storage of information. Fortunately there is also a set of surface and volume contributions to the anisotropy that allow for perpendicular magnetic materials. The basic equation for the thin film magnet anisotropy is $K_{eff} = K_u + K_{vol} + 2\frac{K_s}{t}$, where K_u is the $K_u = \frac{1}{2}\mu_0 M^2$ from the thin film calculation, K_{vol} is a volume contribution, and $\frac{K_s}{t}$ is a surface term contribution for each of the top and bottom interfaces.

Finally, the magnetic field generated by an object has its own energy. This energy is given by $E_{magnetostatic} = \frac{1}{2}\frac{1}{4\pi}\int_{\infty} \vec{H}_s^2 \, dV$ if solved over all space, but can be simplified to $E_{magnetostatic} = -\frac{1}{2}\int_{sample} \vec{H}_d \vec{M} \, dV$ for just the sample. This energy, while related to the Zeeman energy, is due solely to the field generated by the sample. This term will attempt to minimize the amount of field emitted by the sample.

Thus, it is possible to write out an energy of the entire system as a sum of the individual energies. The Landau-Lifshitz energy equation summarizes them as thus:

$$E = E_{exchange} + E_{magnetostatic} + E_{magnetocrystalline} + E_{Zeeman}$$

Thus, for any system, there is the possibility to determine the theoretical magnetic state of the system through ab initio calculation from the magnetic parameters of the system. Micromagnetic simulation is a rich area of research that can provide models for the behavior of magnetic systems.

Coming one step closer to real systems, we have thus far ignored the effects of temperature on the system. The thermal energy of the system is $K_B T$ with K_B as the Boltzmann constant and T as the temperature. In a real system, the thermal energy acts against the order brought by the rest of the system. Increasing the temperature of a material increases the competing energy of randomization. As magnetism is inherently a coordinative effect, introducing a competing energy form will reduce the interaction between magnetic systems. As the thermal competition grows larger, the net magnetic moment of the material will decrease. At sufficiently high temperatures, the system will lose all long range magnetic order and become paramagnetic. This is known as the Curie temperature. The Curie-Weiss law with the equation:

$$\chi \sim \frac{C}{T - T_C}$$

Where χ is the magnetic susceptibility, C is a material specific Curie constant, T is the temperature and T_c is the Curie temperature of the material [8]. If χ is finite and positive, the material can be paramagnetic – where it will either exhibit spontaneous magnetic order, or the application of a magnetic field will produce such order. If χ is negative, then application of an external field will weaken the magnetic order within the material, and it may be a diamagnetic material.

For ferrimagnetic systems composed of two different sublattices of material, both sublattices can have their own Curie temperature. This could lead to an exchange of dominance as the system is heated up. With one system falling off in magnetization versus temperature faster than the other system, the net magnetization of the material could appear to decrease toward zero, and then increase briefly as the system crosses a point where the two sublattices are equal in magnitude but opposite in direction (the compensation point). This will be used in Chapter 3: You, Me and CoTb to perform switching of a ferrimagnetic film via the application of a thermal gradient.

The competition between these different energies and interactions gives rise to a rich and complex variety of behaviors. Strong exchange and anisotropy energies will give rise to a large domain system aligned along the anisotropy axis. Reversing such a system will require the application of an external field or perturbation. A system with large anisotropy will require a larger field to reverse for the same given net magnetization. A system with a lower anisotropy will reverse much more readily in the presence of either an external field or thermal energy.

The competition of between the exchange and magnetostatic energies will create a compromise between them. For a ferromagnetic system, while exchange energies attempt to align all spins in parallel, the demagnetization field will attempt to reduce the poles at the surface. If neither energy is sufficiently large to be completely dominant, magnetic domains will form and between them, magnetic domain walls. A magnetic domain is a region of similar magnetic orientation – where the spins are aligned collinear. At the boundary between two regions of dissimilar orientation, there is a domain wall which is a transition between one state (for the ease of nomenclature will be discussed as "up") and the other state (here "down"). These domain walls are the result of a competition between the magnetostatic energy and the exchange energies – where the overall energy of the system is reduced by changing the system from a single large domain with large magnetostatic energy, to multiple domains. At the boundary between these domains, there will be a smooth transition from one orientation to the other. These domain walls have a characteristic length and energy. The width of the domain wall is a competition between the anisotropy energy. The width of the domain wall is given by $\pi S \sqrt{\frac{2J_{ex}}{K_u a}}$ where J_{ex} is the exchange energy and K_u is the uniaxial anisotropy. Thus, the competition between the two energies determines the width of the domain walls, but for certain states it is also possible to form a multi-domain state with multiple walls.

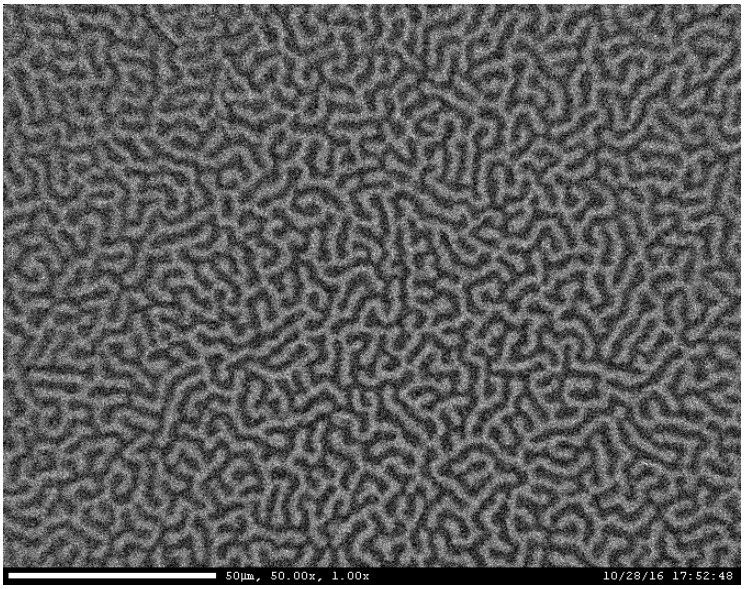

Figure 4: Magnetic domain walls in a material. Domains are areas of similar contrast, and the boundaries between them are domain walls.

In certain systems, it is possible to form a series of different domain patterns. Kittel suggests in his paper "Theory of the Structure of Ferromagnetic Domains in Films and Small Particles" [9] three possible orientations of domain wall structures in thin film magnetic systems. Taking into account a sufficiently thin film with uniaxial anisotropy, there are three possible suggested states. As previously shown, the anisotropy terms and magnetostatic energies are in conflict – one attempting to unify the system and the other attempting to reduce the field generated by the system. Three potential models are shown by Kittel below: where the system forms flux closure domains at the surface and multiple domains internally, where the system forms multiple domains that extend between both surfaces of the thin film, and where the system has overcome the anisotropy and is in-plane. He addresses the balance between the three energies and finds that for realistic arbitrary parameters that the energy will create one of three general cases. These cases vary with film thickness, but for thin films case I will be most likely. For systems with high uniaxial anisotropy, case II will be more likely, and for thicker films where the volume magnetostatic term dominates the system is more likely to be in the plane (case III).

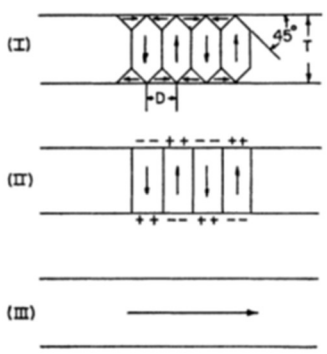

FIG. 1. Domain configurations in films.

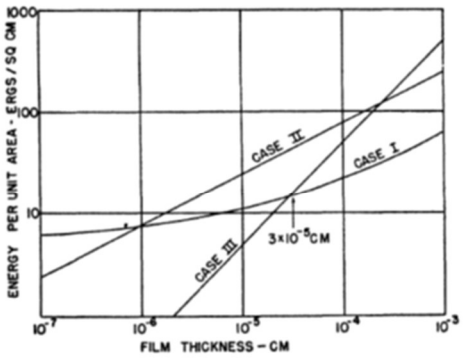

FIG. 2. Energy of various domain configurations in films.

Figure 5: Kittel calculation of multi-domain state configurations and their energies. Left shows three potential formations of magnetic domain walls within a thin film PMA, and right shows the energy of these domain configurations in the sample as a function of sample layer thickness.

For thin film samples used in research for magnetic recording and other magnetic logic systems, typical thickness of the films are on the order of a few nanometers to several tens of nanometers. At these thicknesses, the volume terms from the magnetostatic energy are sufficiently small for the other terms to bring the system out-of-plane. However, as suggested by the crossover point between case I and case III, at sufficient thicknesses, or at low surface energies, there is a crossover between when the system is perpendicularly aligned in a multi-domain state, and when it transitions to an in-plane configuration.

In discussion of this magnetic domain state, the systems have been addressed as if they are Bloch type domain walls with the simplest of exchange energies. For systems with Néel type walls, or including the effects of DMI, the picture becomes slightly more complicated. Néel type domain walls rotate the magnetization of the system out-of-plane, and are more common in thin film magnetic materials where the exchange length of the system is large in comparison to the thickness of the sample. With the addition of DMI, the formation of domain walls becomes more favorable, and it is more likely that the system will form a multi-domain state to reduce its energy. At certain non-zero temperatures, this may lead to the formation of fluctuating domains as the sample

attempts to switch between one state and another. This competition can be seen in the highly critical behavior of Pt/Co/Os/Pt films near a room temperature spin reorientation transition, and gives rise to skyrmions in Chapter 4: The Wizard of Os.

Control of both magnetic domains and domain walls is critical for applications such as magnetic recording. Soft magnetic materials (low anisotropy) which switch readily are useful in carrying magnetic flux or for shielding from magnetic influence. Hard magnetic materials (high anisotropy) which are resistant to thermal effects are critical for storing information. The smaller a domain and its wall can be made and remade, the more information can be stored in the same area. At the same time, many of the energy parameters are related by volume, and thus a delicate balancing act must be struck. Thin and small structures will tend to enforce their own parameters by controlling the volume, surface and shape energies. Material parameters will determine anisotropy, strength of exchange interaction, and any additional energetic modifications. The real systems will tend toward richness of behavior.

So far, these systems have been discussed as generalities. The growth and synthesis of real systems adds another significant layer to the behavior of magnetic structures. Finite sized elements create boundaries which can drive domain wall formation. Intermixing between two different types of material can produce alloys with modified behavior and reduce the effect of interfacial boundaries. Defects in crystal growth lattices can change anisotropy axes and create areas with differential magnetization within the layer. Point defects or debris or scratches on the substrate can create areas of lessened anisotropy or nucleation sites for domain walls. Measuring systems versus temperature will lead to new domain behavior as the material properties change.

The exploration of the behavior of these materials will begin with the general fabrication of the systems, and then move towards the characterization of these materials. Interesting domain

behaviors will be examined in a variety of material systems, through several lenses. The origin of the study of magnetic materials begins with systems behaving in novel ways – with iron unexpectedly attracted to the lodestone. This tradition will be continued, with the examination of systems that change orientation due to temperature, and systems that form novel magnetic textures.

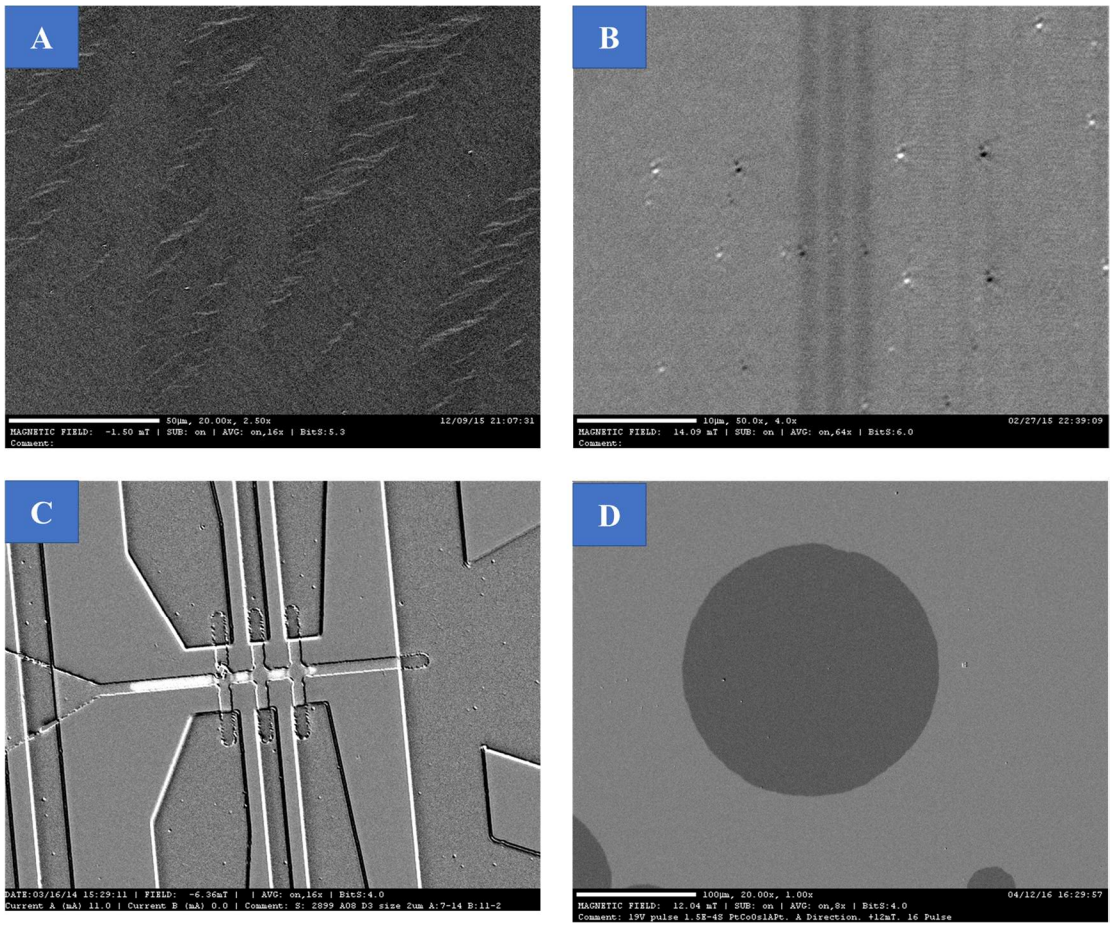

Figure 6: Example Kerr microscopy images showing magnetic domains and contrast. A: CoFeN thin film in longitudinal Kerr geometry showing multiple stipe domain geometries. B: Hard Disk Drive servo track in polar Kerr geometry observed by movement of sample showing regular magnetization domains for orientation of hard drive head. C: Thermally nucleated domain wall (white) in CoTb thermal gradient device – more in Chapter 3. D: Pt/Co/Os/Pt thin film with circular domain expansion from a defect site – more in Chapter 4.

Chapter 1:
Magnetic Materials And How To Grow Them.

Thin film magnetic material structures can be created in a number of ways. In general, high vacuum processes involve creation of a plume of energetic atomic material that is directed toward the substrate. This can be done by thermal evaporation, pulsed laser deposition, or magnetron sputtering. Work in this dissertation was done primarily by magnetron sputtering with an AJA corporation ATC Orion AC/DC magnetron sputter tool (Figure 7).

Magnetron sputtering works by generating an energetic plasma above a target of source material. This target, when bombarded by the energetic process gas ions, ejects a plume of material. The material follows a ballistic path through the high vacuum area of the chamber (although thermalization via collisions with process gas does occur) before landing on the desired substrate. Magnetron sputtering is a well-established and industrially used technique, especially for complex heterostructures including metals, oxides, nitrides, carbides, etc. and can be used to produce a wide variety of films of pure, alloyed, and multilayer materials. [10] General techniques for sputtering used through this dissertation will be outlined here.

Chapter 1, Section 1:
Fullerton Lab Sputter Equipment

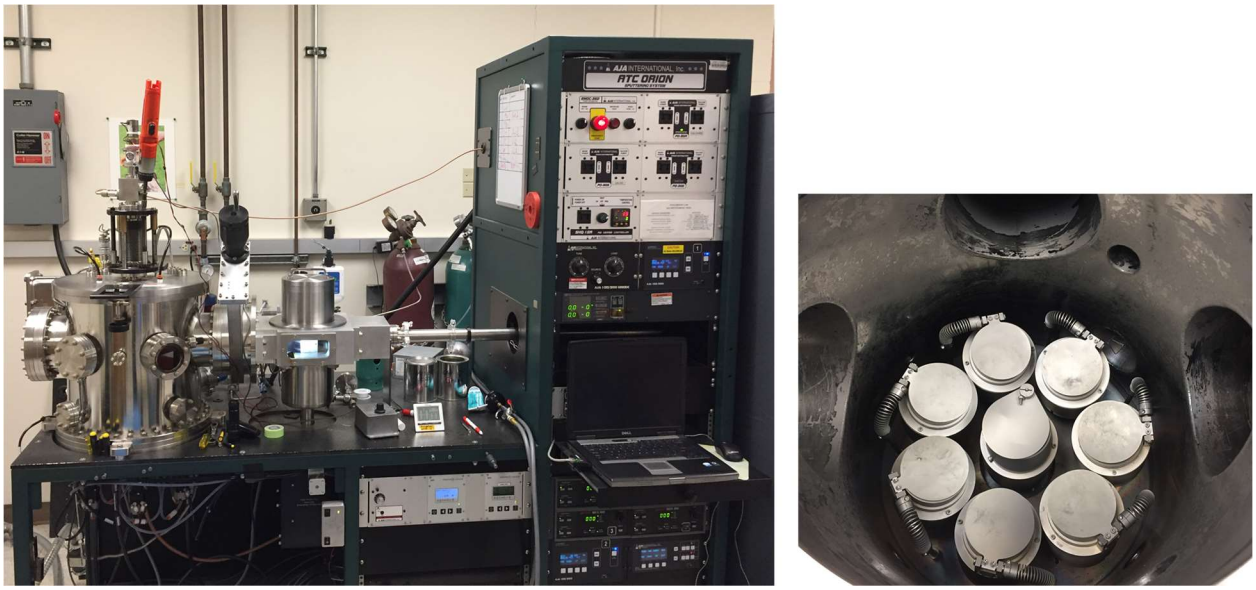

Figure 7: ATC Orion sputter tool by AJA International. Left shows the entire machine, while right shows a view of the sample chamber from the top (where the sample would be mounted). Visible are is the 7+1 sputter gun configuration.

The ATC Orion sputter tool in the Fullerton lab at UCSD mounts 7 + 1 guns in a confocal ring configuration (7 angled perimeter guns + 1 center source). All guns are built for a 2 inch target, and can accept both unbonded and bonded targets. Each source has the capacity for both DC and RF plasma generation. Four 500 W DC power supplies are available, with automatic network matching and short detection. A 300 W RF power supply is available to drive a gun, but can also be run through the top stack of the sputter chamber (on the sample holder) with a power of 50w. Two sets of mass flow controllers allow a mixture of reactive and inert process gasses, with Argon (Ar) being the choice inert process gas. Typical reactive process gasses include Nitrogen (as N_2) and Oxygen (as O_2). Process gas is introduced through several ports in the top and bottom of the chamber, with Argon introduction near the base of each gun, and any reactive process gas introduction through either the top or bottom ports. Gas is removed by a turbo pump

backed by a roots pump, and the pressure is controlled by a combination of the position of the gate valve and the input MFC setting. Base pressures of 10^{-8} Torr are easily accessible, with 10^{-9} Torr or better accessible after a chamber bake process. Two 1000 W halogen lamps in the top of the chamber are intended for heating the sample holder/substrate, but also have found use in baking the chamber to remove adsorbed gasses and water from the chamber walls. A cassette loading system allows 6 sample holders (pucks) to be placed in the load lock for rapid exchange.

In the function of the Fullerton sputter tool, the system processes were standardized by mass flow and gate position to provide a process pressure of 3mTorr. At an MFC setting of 50 standard cubic centimeters per minute (SCCM), with a gate valve at 55% of total flow, the pressure in the chamber comes to 3 mTorr. This 3 mTorr process pressure is the standard for all samples that do not require reactive sputtering or special pressure considerations. While low background pressures are critical for certain types of films, others are sufficiently unaffected by a pressure of 10^{-7} Torr or better. In this work, unless specifically stated, background pressure was not a significant consideration for the growth of the films, as long as it was 10^{-7} Torr or better. While the system is capable of heating the substrate for deposition, in practice nearly all depositions were carried out at ambient room temperature (unless otherwise specifically noted).

Samples have two basic geometries as commonly grown – a 4.1 mm x 3.8 mm substrate used for VSM techniques, and a 10 mm x 8 mm substrate more commonly used for lithography. The total surface area for the VSM technique is 15.6 mm^2 which will be covered by the deposited sample material. Typical thicknesses of the entire deposited layer will be between 1 and 50 nanometers. Calculations of magnetic moment per material volume will depend on choice of magnetic material, but will be important in determining the strength of the magnetic order.

Chapter 1, Section 2:
Sputtering Background

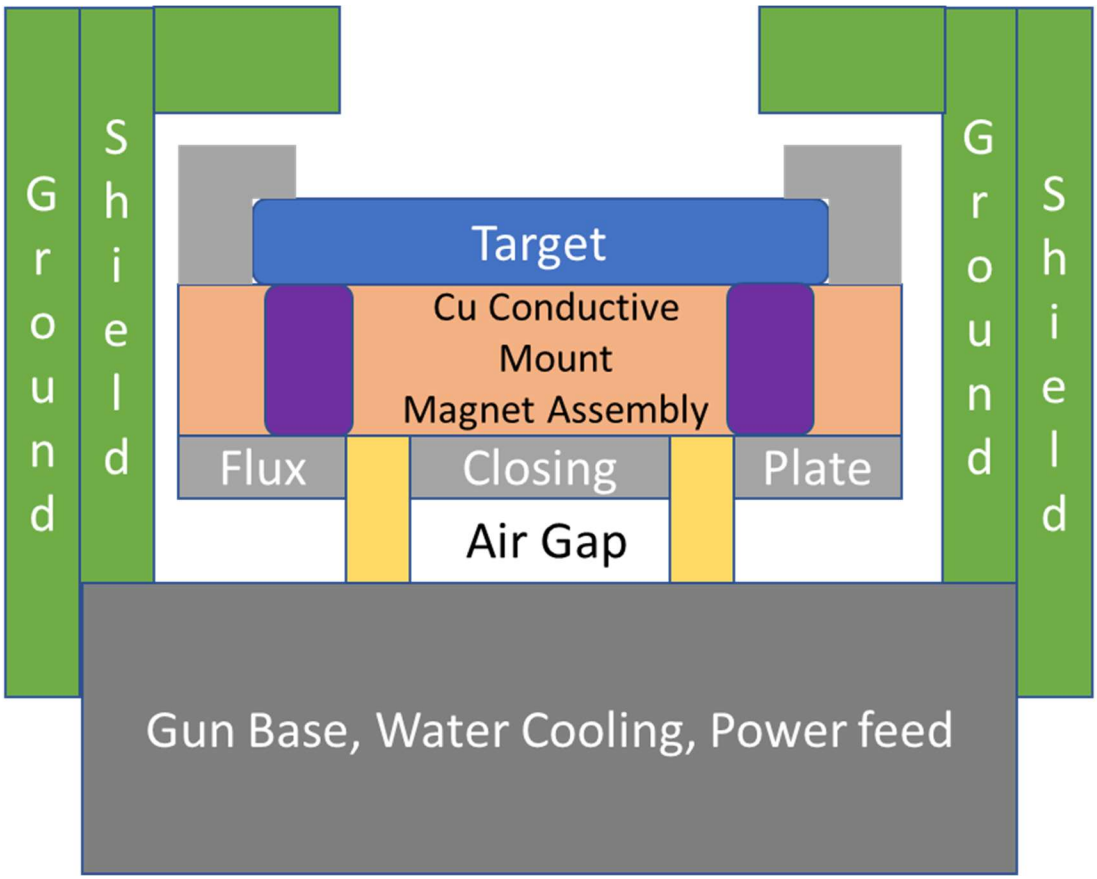

Figure 8: Cross sectional view of sputter gun. The target is clamped to the conductive plate (orange), which houses the magnets that will confine the plasma (purple). This assembly is electrically insulated from the gun base and ground shield assembly by ceramic insulators (yellow) and an air gap.

Shown in Figure 8 is a cross-sectional schematic of a sputtering source. The target is first mounted to the electrically isolated component of the gun with a target clamping ring. Over this assembly is placed a grounding ring and a combination chimney / shutter assembly. Into the vacuum of the chamber, a small amount of neutral process gas (typically Ar) flows. A large

negative voltage is applied to the target. Once a Ar atom is ionized in the chamber it is accelerated to target knocking off an atom of target as well as electrons. The negative charged electrons are accelerated away from the negatively charged target but are confined to an area above the target by the magnetic field generated by the magnets below the target. These highly excited electrons ionize more Ar atoms which are accelerated to the target generating more sputtered atoms and electrons. This process avalanches to set up a plasma above the target confined by the magnetic field. The magnitude of the voltage on the target is reduced to a set value and the electrons emitted from the target are replaced by a current flowing from the power feed into the gun. Thus, the Ar ion is accelerated through the electric field and crashes into the surface of the target. This inelastic collision between the Ar ion and the target material transfers momentum to the atoms of the target. With enough energy, the effect can be akin to throwing a ball into a pile of sand – some of the target material can be ejected by the collision. This gaseous plume of target material is broadcast out from the gun and can be collimated and controlled by the chimney or shutter assemblies.

The neutral atoms from the target in the sputter plume will land upon either the chamber wall or the desired substrate. Landing upon the substrate, the target material atoms will shed the remainder of their kinetic energy into the already deposited layers and adhere to the sample. Thus, little by little, a layer of deposited target material of desired thickness can be created. The rate of the deposited atoms can be controlled by the power supplied to the gun. In sputter deposition the sputtered atoms have relatively high kinetic energy which increases the surface mobility of the deposited atoms. The growth surface can also become bombarded by reflected neutral gas (Ar) atoms, electrons and negatively charged ions that have significantly higher energy than the deposited atoms and provide the means to modify surfaces and interfaces. Due to the kinetic energy of the deposition plume, the atoms on the surface of the substrate can move and thermalize to a

lower energy state. Control of these energies, via sputter target voltage, Ar sputter gas pressure, target-to-substrate spacing, etc. can give significant tenability. Thus, when talking about structural details of interface between multiple layers and types of materials, deposition parameters can have a significant effect on the outcome of the process.

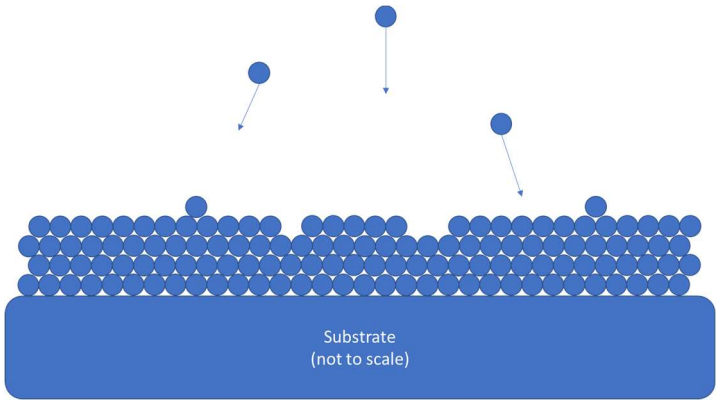

Figure 9: Schematic of deposition of material.

As seen in Figure 9, atoms of specie A will land on the substrate and adhere to the topmost layer. Depending on the type of material used, it may form a fully amorphous layer (with no long range crystalline ordering), a nanocrystalline layer, or a crystalline layer (which is ordered over a long distance). For most of the materials discussed here, the systems use amorphous layers and multilayers with no special attention paid to creating crystalline growth conditions. For a single layered system, the thickness of the material can change multiple properties due to the growth orientation. At high energies where each arriving atom brings enough energy to rearrange the local structure, the system will have sufficient energy to smooth the surface toward the desired lattice spacing of the deposited specie (as suggested in Figure 10). If instead the deposition energies are sufficiently low, roughness may build up in the system, creating ripples on a long length scale. This is suggested in the center of Figure 3, where a slight lattice shift has disrupted the local order of the blue specie. If deposition continues, the disruption may be reduced by encroaching order

from the rest of the system, or the lattice distortion could continue to propagate through the thickness of the film.

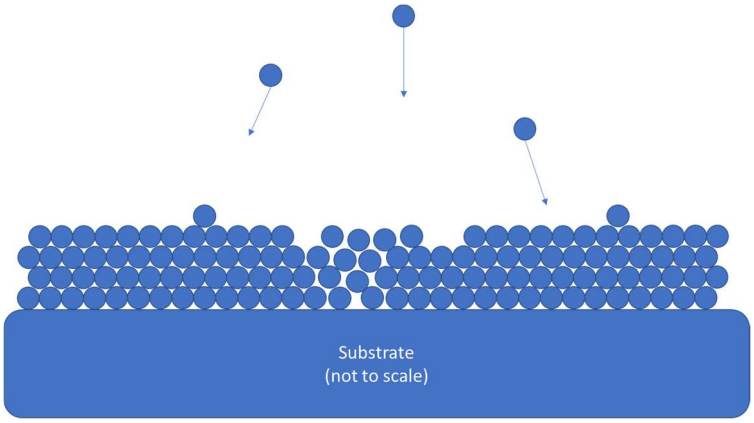

Figure 10: Roughness due to lattice shift.

This relatively simple explanation would be simple enough if only one type of material was being deposited in single layers of roughly the same thickness. However, this is rarely the case, and no one really cares about monolayers of a single type of material. When depositing two or more different types of material, either in multilayers or as an alloy, there are several potential issues exaggerated below.

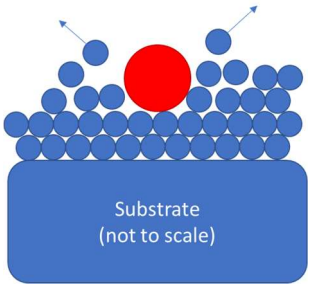

Figure 11: Incident B atom disrupts deposited A specie.

If depositing a material with a much larger atomic radii, or much higher mass, it is possible that the arrival of an atom with sufficiently high energy can disrupt the already deposited structure. This type of implantation can disrupt an already deposited layer and reduce that layer's

magnetization. At low fluence of incoming atoms (depositing a thin monolayer or sub-monolayer of the atoms), this may result in a dead layer at the interface.

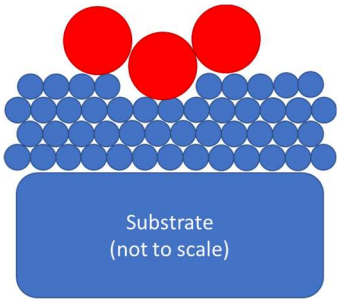

Figure 12: Deposition on layer of different spacing.

If the atoms arrive with a sufficiently low energy to not disrupt the underlayer, the top layer may still be affected by the structure of the bottom layer. Discrepancies in the underlayer can propagate through the top layer and any additional layers deposited on the surface. In addition, any defects in the underlayer will create a problem with the next layer on top of it.

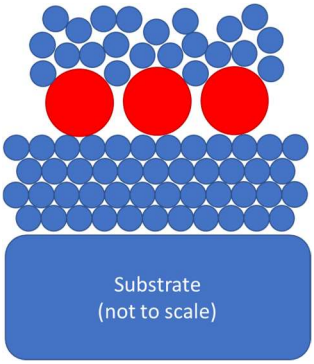

Figure 13: Roughness as caused by lattice mismatch.

Independent or less dependent on the growth parameters, is the possibility of lattice mismatch between the two deposited materials. In this case, the “B” specie has a much different preferred lattice spacing than the “A” type material. While “B” is being deposited on “A”, it will attempt to strike a minimum energy position between the preferred lattice spacing for “B” and the base spacing of material “A”. This will be neither the spacing for “B” nor the spacing for “A” but some compromise between the two. Obviously not as extreme as pictured in Figure 6, but there is

the definite possibility of tensile or compressive strain as “B” is grown upon “A”. If then, another layer of “A” is deposited on top of the “B” layer, it is possible that due to the aforementioned lattice mismatch, that the second “A” layer will have a different spacing and properties than the initial “A” layer.

An annealing process performed during or after the layers are deposited may improve or worsen the layer profile. For strongly ordered materials, an annealing process may allow the system to create a single crystal order across large areas. Interfaces between different material types will typically improve with annealing, allowing layers to fix energetically unfavorable discontinuities or stairstepping, eject interstitial atoms implanted by bombardment, and reduce roughness of the interface. However, annealing can also contribute to material intermixing at the layer boundaries if the two materials easily form an alloy. Deciding to use an annealing process, or avoiding annealing by keeping the system cool will depend on the process, layering and materials used.

As can be seen from the previous examples, deposition parameters and order matter while making any layered material. While typically less critical in amorphous materials (as opposed to those with high crystalline order), certain layer structures will produce a different result if grown in one orientation or the other. For example, later on in the dissertation, a layer stack of Ta/Pt/Co/Os/Pt/Ta will exhibit significantly different properties from a layer stack of Ta/Pt/Os/Co/Pt/Ta. Structures and material properties will change depending on the growth direction, deposition parameters, and equipment factors. Attention has been paid to the base pressure and target cleaning – with the chamber at atmospheric contact to replace targets, the system will adsorb water, oxygen and other contaminants. By heating the chamber and leaving the system pumped down, the various contaminants will slowly desorb from the chamber wall and be

removed by the vacuum pump system. While the system will gradually improve its base pressure without a bake, by increasing the temperature the process can be greatly accelerated. For material systems where base pressure is critical, a series of bake processes can be run that will swiftly improve the base pressure.

Designing the deposition process can also be important for the final result. Calibration of the guns is based on depositing a thick film of the target material from the gun in which it is loaded. As calibration rates for materials can vary over the lifetime of the target, between guns, and depending on deposition parameters (gas pressure, gun power output), it is critical to ensure that the correct deposition rate is used in designing the film process. While there are in-situ techniques for measuring the film as it is being deposited i.e. Reflection High-Energy-Electron-Diffraction (RHEED), crystal film thickness monitor, or in-situ X-Ray, these techniques have some limitations for high usage systems. Consequentially, the growth monitoring for the layers and structures produced here is done either pre-deposition or post-deposition.

Pre-deposition layer management is done by depositing a thick film from the target gun on a standard Si substrate. This film is significantly thicker than would ordinarily be deposited (typically a 1500 second or 2700 second deposition) and will be analyzed by X-Ray Reflectivity (XRR) for thickness. For such measurements, $\theta/2\theta$ XRR measurement was performed giving reflectivity peaks as shown:

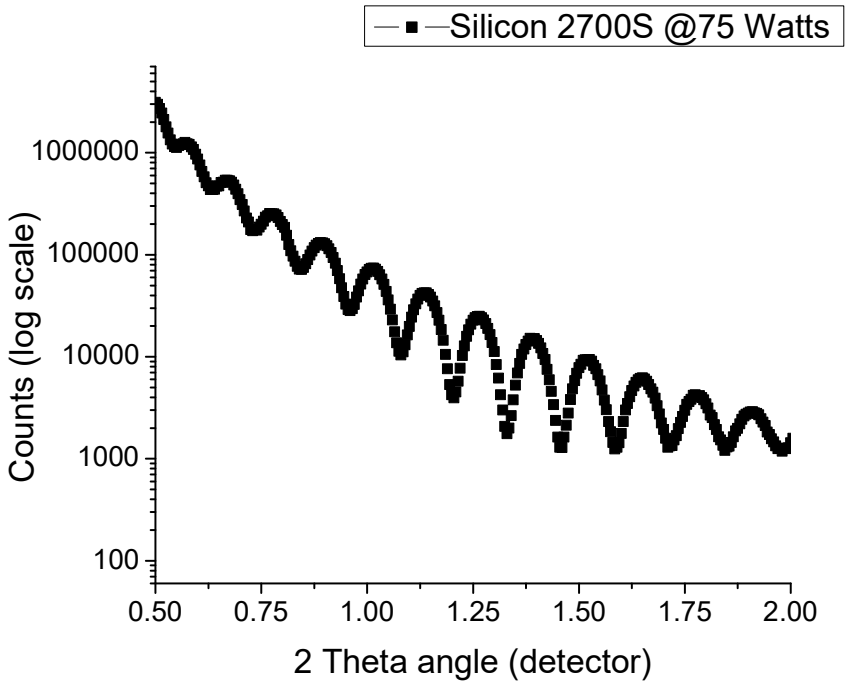

Figure 14: Raw X-Ray Reflectivity curve for thick Silicon calibration sample. Note the X-axis is from the 2 theta detector angle, while the Bragg's law will use the theta from the source.

By fitting the local minima and maxima to a modified Bragg's law formula, the film thickness can be found, and the deposition rate in nanometers/sec can be used. This results in a calibration rate for a given set of conditions. Fortunately, the deposition rate versus power output of the gun is fairly linear – this means that with one calibration in the nominal deposition conditions it is possible to change the power within a wide range and the deposition rate will be predictable. Thus for films like the CoTb alloys or other alloy materials deposited from two separate pure targets, it is possible to create different compositions by varying the output power of the two guns. This technique is known as cosputtering, and while it is possible to produce a much wider range of composition space than from a single composition target, the variability of an alloy layer will be significantly higher as highlighted later.

Full film systems are useful for measurement of the bulk magnetic properties (through VSM magnetometry measurements), or for localized domain observation (through Kerr

microscopy), but are a poor choice for electronic transport measurements. Thus, some form of patterning into device structures is useful for many applications. Special Section 2 will detail the design of these structures on an optical lithography photomask, while here is discussed the general procedure for deploying these features on a substrate. There are two general methods to accomplish lithography – either place a lithographic template on the surface and deposit into the template, or deposit a template on the completed film and etch away the material not covered by the template. Both procedures have their uses, advantages and disadvantages.

Chapter 1, Section 3:
Lithography and Patterning Processes

The most common lithography technique used in this dissertation is a lift-off photolithography technique using negative photoresist. The negative photoresist used is Futurrex NR9 1500/3000PY, a cyclohexane solvent based long-chain polymer that is developed by the standard 365nm wavelength exposure. Being a negative photoresist, exposure to the UV light changes the structure of the polymer so that it cannot be removed by the partnered developer. Thus to deposit a "blank" – a substrate ready for the deposition of magnetic material, the desired feature should be designed in a reflective metallic layer see Special Section 2 that will shield the desired area of the sample from the UV light emitted by the mask aligner.

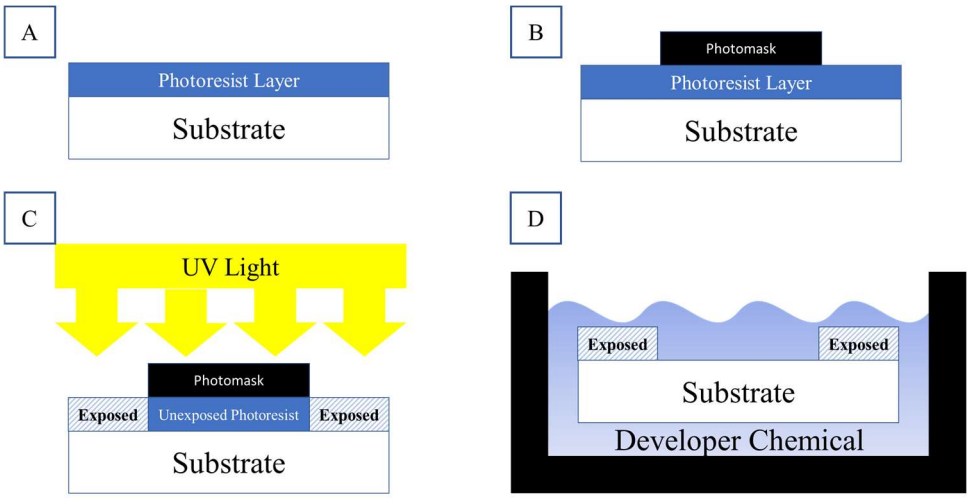

Figure 15: Negative resist lithography process. A. The photoresist is applied to the substrate layer. B. The photomask is oriented so that it will block light from the targeted area. C. The photoresist is exposed to UV light, setting the polymer. D. Unexposed photoresist is removed by dissolution in the developer. This same process applied to a positive photoresist would produce a substrate with an island in the center (inverted).

The above figure shows the lithography process involved in creating a blank. Once created, lithography blanks can be stored for several weeks in a vacuum desiccator before use. Thus it can be useful to have created a large number of lithography blanks at once and then use them throughout the course of a deposition. Depositing into a blank is done much the same as on an unpatterned substrate. Once the film material has been deposited onto a blank, the photoresist can be removed (in the lift-off step) by immersion in acetone and slight agitation or ultrasonic removal. Proper conditioning of the sample will result in the photoresist layer lifting off and removing the over-deposited thin film as in the figure below.

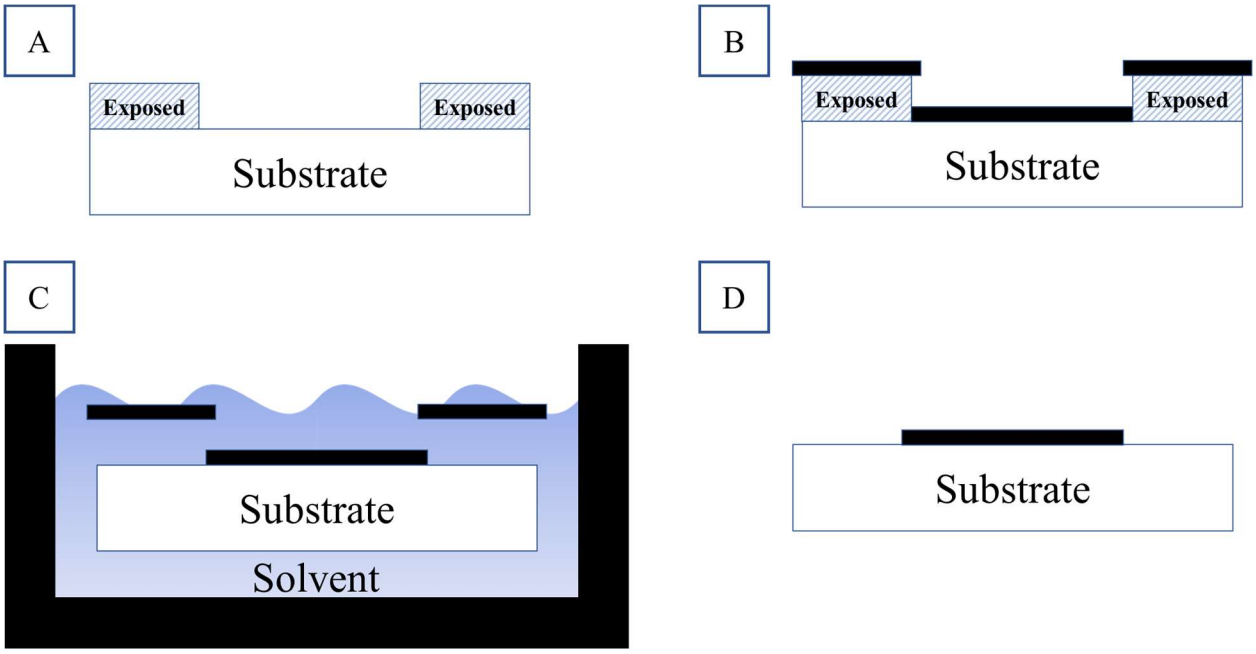

Figure 16: Process of sputter deposition and lift-off. A. Starts with a prepared blank, which has the sputtered layer (in black) deposited on top. In C. the photoresist is removed by a solvent, which also removes the material deposited atop the photoresist by mechanical action. D. The final result – the lithographically patterned wire.

Lift-off with photoresist is a useful technique for depositing films into structures, however it is not necessarily always efficient or practical to start with a sample blank. Some features, films or particular layer structures require starting with an as-deposited film and then patterning that film into a structure. For this, it is often more useful to perform an etching process (protecting a target

area and removing material not covered by the protection). While the photoresist deployment process is the same, for this technique a positive photoresist is used (for the same photomask). Thus, the feature that would have been a hole in the deposition/negative photoresist case is now a layer for the etch/positive photoresist.

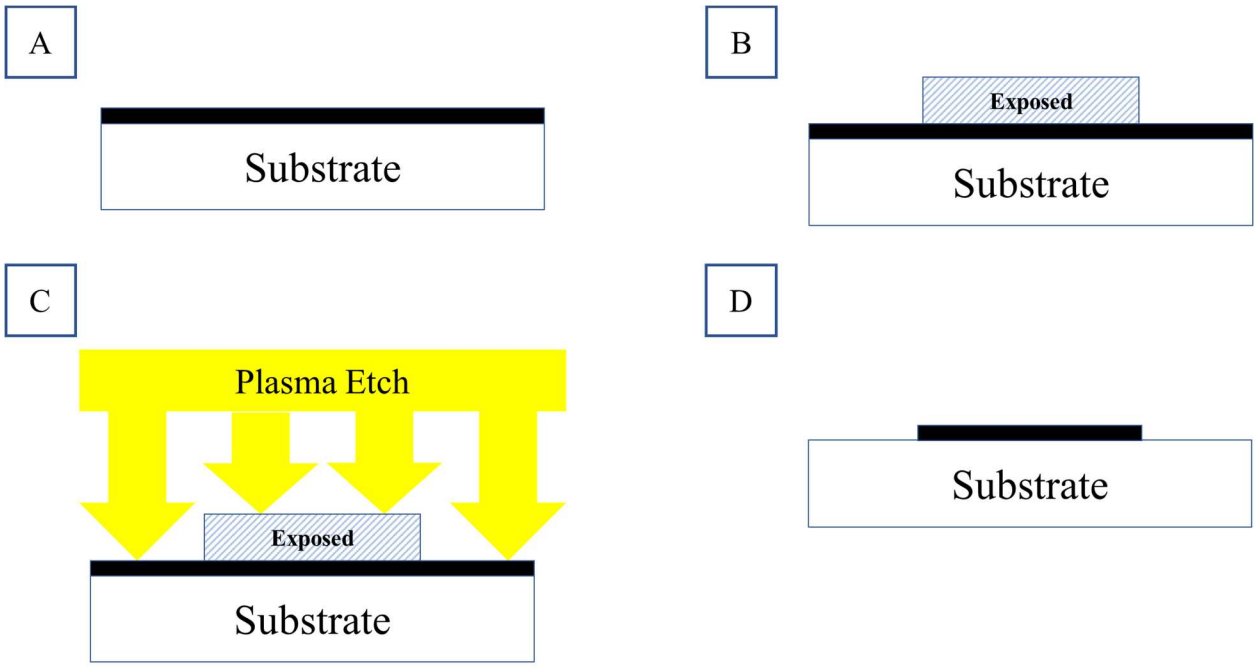

Figure 17: Positive photoresist etch process. A. Full film is deposited by sputtering (unpatterned). In B, a positive photoresist layer is deposited using the same process as previously outlined. C. A high energy plasma is used to etch and remove the metal layer unprotected by the resist coating. D. Left over photoresist is removed by solvent rinse.

Etching is accomplished by creating a high energy plasma at the surface of the sample. This plasma bombards the surface, attacking the deposited film and the protective layer of photoresist. Anything not covered by the photoresist will be removed given enough time, energy, and the proper composition of the process plasma. While Argon non-reactive plasmas are commonly used, there are also multiple different reactive process gasses available. Plasma type, energy and duration will all depend on the type of material being etched, the thicknesses of the layers, and if any additional design parameters are needed (a restricted etch depth, etc). One

occasionally overlooked element is the transfer of heat to the magnetic film during the etch. While the effective anneal will depend significantly on the process used, in films with a significant change between as-deposited and anneal, this must be addressed. In Chapter 4, this will be evaluated as a form of annealing the sample to modify the interface properties.

While most photolithography processes use far UV light around the 350 nanometer regime, the resolution of the system is inherently limited by the resolution limit of the light. Certain of the samples used in Chapter 3, were instead defined by electron beam (E-beam) lithography. The overall process of E-beam lithography is similar to photolithography, except that instead of using a combination of high energy light and a covering plate to pattern the photoresist, an electron beam is used to pattern the photoresist. While the photolithography relies upon exposing the entire sample at the same time, this is not possible with the point-source electron beam used in E-beam lithography. Instead, the exposure spot of the electron beam is raster scanned across the desired pattern. This produces high resolution patterns, with the caveat that care must be taken against overexposure in enclosed corners. One other significant issue with E-beam lithography is that the time to deposit a feature scales directly with the size of the feature. Thus, while E-beam lithography is an excellent candidate for creating sub-micrometer patterns, it becomes spectacularly inefficient at larger contacts or features that cover wide areas. In addition, in order to form the electron beam, the system must be at high vacuum. This, along with the focusing of the electron beam and imaging beam make upkeep and deployment of the E-beam system more intensive than a photolithography system.

These sample fabrication techniques are useful for creating constrained systems. While multi-stage processes are available and used, the work in this dissertation has attempted to avoid the complex fabrication processes as much as reasonably possible.

Chapter 2:
Measurement Techniques and Methods

Magnetic systems come with a wide variety of possible measurements. The interaction of magnetism, magnetic field, electromagnetic radiation, and electrical transport provide a wide variety of rich analysis methods across wide length scales. For modern thin-film magnetic materials used in data storage applications, the overall volume of the samples are small – around 10^{-8} to 10^{-7} cubic centimeters for some samples used in this lab. This limits the detection and measurement of certain volume sensitive measurements. As discussed, the detection of magnetic domains and domain walls is also of significant interest. For data storage, these length scales vary to optical wavelengths of light and below. This section will discuss several methods of the measurement and evaluation of magnetic materials used in this dissertation, including Vibrating Sample Magnetometry (VSM), and Magneto-Optical Kerr Effect Microscopy (MOKE Microscopy).

Chapter 2, Section 1:
Vibrating Sample Magnetometry

One critical measurement for the analysis of thin magnetic films is the magnetic moment of that film versus applied perturbations. Moment versus field measurements can provide critical information about the strength of the coupling between the magnetic layers, the anisotropy (if measured along different axes), and the possible reversal mechanism of the film. Moment versus temperature measurements can provide information about the relative strength of the different interactions that control the structure of magnetism.

Magnetometry measurements are significantly varied, and depend on a wide range of effects. Most modern cell phones have a Hall effect based magnetometer that provides a vector measurement of magnetic field strength. Geomagnetic sensing is used for everything from natural resource location to military detection of submarines and landmines. These techniques have a wide range of allowable field excitation and sensitivity. For magnetic recording thin films, with thicknesses on the order of tens of nanometers, the moment is incredibly small. With the high anisotropy necessary to store and retain information for long periods of time at the device temperatures, high magnetic fields are needed to fully probe the range of reversal. A combination of sensitivity, field range and ease of use is critical for laboratory measurements.

Of the available techniques for measuring small magnetic samples, vibrating sample magnetometry offers several significant advantages. The technique is capable of measuring very small moments to a good degree of accuracy. Coil based VSM systems use a wire pickup coil to measure changes in magnetic flux through the coil, while the magnetic sample is vibrated through

the coil. It is a robust technique first developed by Simon Foner at MIT Lincoln Laboratory [11]. The long history of the VSM technique comes from its basic nature that is rooted in the fundamental interactions of magnetism and electrodynamics [12].

Measurement of a static magnetic system is difficult, especially so at tiny volumes. Stray field measurements are even more difficult, as the formation of closure poles and sample geometry will often minimize stray field effects. However, from Maxwell's equations, there is potential solution. For a closed loop, whether of wire or as a mathematical abstraction, a change in the magnetic flux through that loop will induce a voltage in that loop.

$$\nabla \times \vec{E} = -\frac{\partial \vec{B}}{\partial t}$$

Thus, while it is difficult to measure a static magnetic flux, measuring a *changing* magnetic flux can be done with fairly simple techniques. Rotating a coil of wire within a constant magnetic field will produce a change in the flux through that coil. Alternatively, changing the magnetic field intensity will also produce a change in flux through the static coil. It is also possible to crate this change in flux by moving the magnetic source through the measurement coil. It is this last method that will be used by the Vibrating Sample Magnetometer (VSM). This measurement technique also has the advantage of being *insensitive* to a steady magnetic field, thus allowing for the sample to be magnetized in a homogeneous field.

For a sample moving along the z axis with a sinusoidal excitation (the most common VSM excitation), the movement of the sample has an equation

$$\frac{dz}{dt} = \hat{z} \cdot \omega \cos(\omega t)$$

This results in a variance in the magnetic flux through the pickup coil system, which creates a time-varying electric field within the coil. Through a lock-in measurement technique, very small voltages can be measured and amplified to a signal. Quantum Design corporation provides a VSM head and coilset attachment for their Versalab or PPMS systems. This system includes a linear motor capable of 2mm excitation at 40hz, a number of available coilset inserts, and a signal processing module [13].

Figure 18: Quantum Design Versalab with Vibrating Sample Magnetometer module.

This system is capable of measuring moments as small as low 10^{-6} emu which for the ferromagnetic materials of cobalt or iron corresponds to a 4.1mm X 3.8mm sample of a thickness of several angstroms. Temperature can be scanned from 50 to 400 K in the Versalab or 2 to 400K in the PPMS in the basic mode, or with a heater module the system can be used with in-plane configuration up to 1000K [13]. The VSM is capable of measuring in both in-plane and out-of-plane sample geometries depending on the sample mounting direction.

A critical consideration for the VSM moment is that the system will generate a signal from everything that is within the measurement bore. This includes not only the sample itself, but the substrate, the mounting device, any particulate contamination, and any inhomogeneities within these systems. In using the VSM system, some care must be taken in the mounting of the sample and the evaluation of the data. Because of the high sensitivity of the system and the small moment of the samples, any contamination of the samples will significantly impact the measurement. Non-ferrous tools should be used for the best sensitivity, and care should be taken to minimize edge and side deposition on the target substrate. In mounting the sample, certain techniques will provide more reliable results.

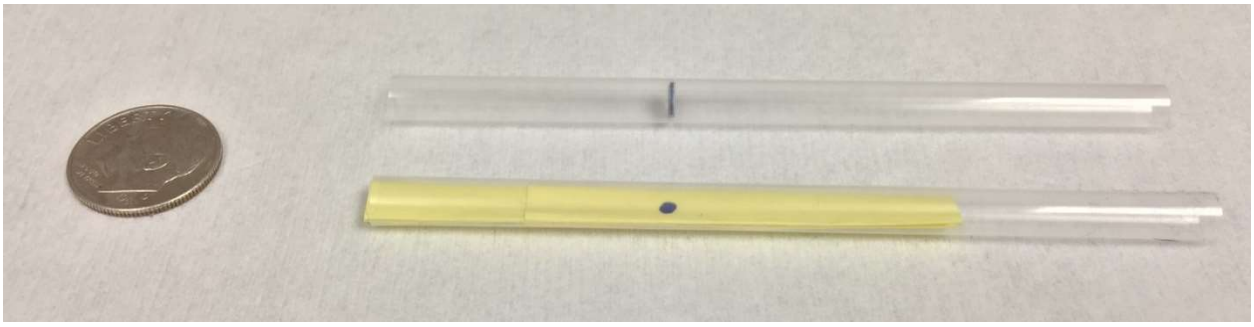

Figure 19: Mounting of a VSM sample in the plastic straw. Out-of-Plane orientation is shown at top, with sample 35mm from bottom (left). In-Plane orientation is shown at bottom, with sample position in the sticky note marked by a dot. Sample mounting rod will be inserted at top (right).

A standard method of mounting samples in an out-of-plane geometry is to use a paper sleeved plastic drinking straw. In handling all materials, gloves should be used to avoid contamination from dead skin and hand oils. After the straw has been removed from its protective paper sleeve and cut to an appropriate length for the system, the sample is inserted into the straw. For the out-of-plane geometry shown in Figure 19, the sample can be wedged into the flat orientation in the straw, using the edges of the sample to hold it in place. For the in-plane geometry, the sample is attached to a standard post-it sticky note and folded. The sticky note is cut to reduce

the total volume, and care is taken to keep the sticky note uniform throughout the length of the measurement axis.

By ensuring the relative uniformity of the mounting system, the contribution of the system is minimized. As the VSM technique uses a time-varying signal, if the value of the magnetic materials is constant across the actuation range of the motor, the lock-in technique will minimize the observed effect. This cannot completely eliminate the effect of the additional diamagnetic contribution of the drinking straw and post-it combination at high fields. As shown below in Figure 20 however, this contribution is diamagnetic, linear and can thus be safely fit and removed from each measurement.

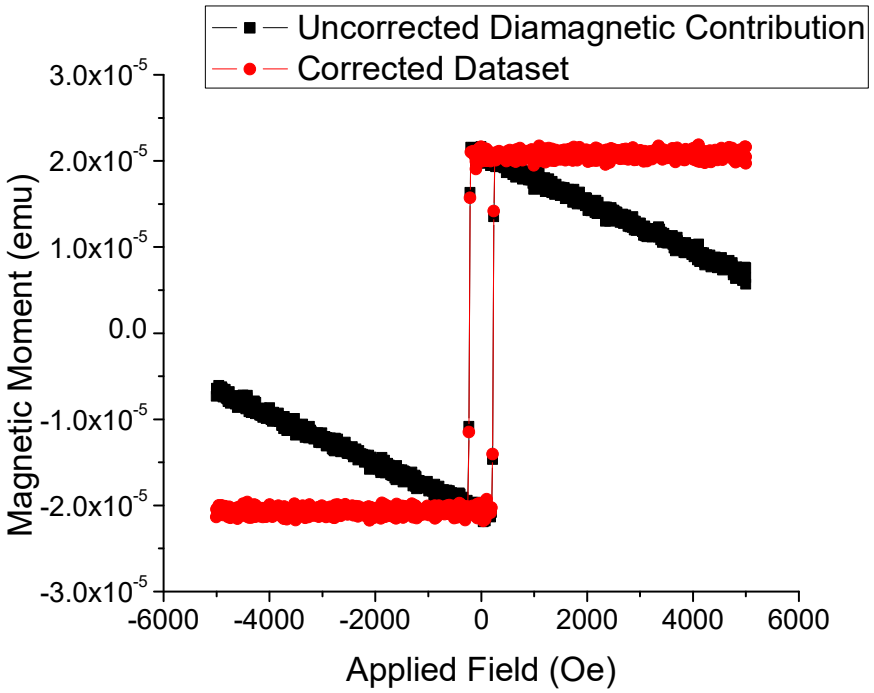

Figure 20: Data before (black) and after (red) diamagnetic subtraction. A linear fit to the tail of the data is used to find the diamagnetic contribution from the straw, substrate and any mounting.

The VSM technique for measuring the magnetic moment of the sample is robust and well realized. It provides a way to measure the magnetic moment versus applied field and temperature,

which can give critical information about the evolution of the magnetic system on a full-film level. By varying sample geometries, it is possible to calculate magnetic anisotropy from a combination of in-plane and out-of-plane measurements. For the growth of samples in the Fullerton lab, the measurement of a hysteresis loop versus magnetic field is often one of the first basic measurements undertaken of a film.

Chapter 2, Section 2:
Magneto-Optical Kerr Microscopy

Many magnetometry measurements techniques such as Vibrating Sample Magnetometry (VSM / SQUID VSM) measure the volume averaged magnetization of the entire sample. By sweeping the magnetic field a hysteresis loop is obtained that allows properties of the entire magnet (saturation magnetization, remnant magnetization, coercive field, etc.) to be determined. However, especially with interest in recording physics and magnetic microstructures, there is a need for local scale measurement of the magnetic state of a material rather than the volume averaged magnetic moment. By observing the local properties and domain morphology of the system, certain details and pathways of the magnetic state are exposed. To address this challenge there are many techniques like Atomic Force Microscopy and Magnetic Force Microscopy (AFM/MFM), X-Ray Microscopy, and PhotoEmission Electron Microscopy (PEEM) that are available for work at the nanoscale, but some require significant hardware investment. Magnetic imaging techniques generally separate into two types of technique, those that measure the stray magnetic fields out of the sample and those that directly image the magnetization. AFM/MFM is an example where the stray fields are imaged. While MFM has very high spatial resolution it however is it sometime difficult to uniquely determine the magnetization pattern from an MFM image, the imaging is taken by scanning over the sample and can be slow and it is difficult to image dynamics or in time-varying field.

A number of techniques can image the magnetization state of the material directly. Magnetism can be studied by resonant soft X-ray techniques. Resonant X-rays provide elemental, chemical, and magnetic sensitivity via the sharp core-level resonances available in the soft x-ray

range (e.g. L edges for the 3-d TMs and M edges for REs). Energy tuning provides element specificity and tuning the polarization provides sensitivity to magnetic properties. Circularly polarized x-rays can be used to probe ferro- or ferri-magnetic materials through magnetic circular dichroism. The resonant cross sections are quite large allowing quantitative measurements of monolayer films. Additional information can be gained on the spatial variations through magnetic imaging or scattering experiments. Linearly polarized x-rays are used to probe ferro- or ferri-magnetic materials by scattering, and probe antiferromagnetic order via magnetic linear dichroism. The typical wavelengths that set the scale of scattering and imaging techniques using soft x-rays are $\lambda \sim 1.5$ nm. However such studies generally require synchrotron light source centers (ALS, APS, SSRL, ESRF, LURE -now SOLEIL) to study magnetic materials. are limited by a requirement of space and or holding the sample under vacuum. AFM and MFM techniques can be severely limited in the speed of the measurements, and what perturbations can be applied to the sample during measurement.

In contrast to these techniques, Kerr effect microscopy offers an optical-light resolution microscopy technique capable of measuring the magnetic orientation of thin film materials. While lacking the several-nanometer-scale resolution of MFM or Full Field X-Ray Transmission Microscopy, the technique is fast, robust, and allows for the inclusion of many sample perturbations. It can be performed at a variety of temperatures, with and without continuous or pulsed magnetic fields, electrical currents, strain, or laser excitation. Measurements can occur in real time, and offer an immediate nondestructive imaging of the magnetic state of the surface of the film. While Kerr effect microscopy is used for measurements where the light is reflected from the sample, a similar measurement is available when light is transmitted through the sample. The Faraday effect is similar to the Kerr effect, however the polarization rotation is induced in the

material due to its propagation through the material. The mathematical differences between these two techniques will be addressed briefly in the mathematical treatment of the Kerr effect [3] [14] [15] [16].

Kerr microscopy works on the basis of the Magneto-Optical Kerr Effect (MOKE). The technique is sometimes also known as MOKE microscopy. The basis for MOKE is the interaction an optical light with magnetism. In the simplest terms MOKE measurements involves reflecting linearly polarized light reflected from a magnetic films/surface. Upon reflection the polarization of the electric field of the light is changed by the reflection from the magnetic surface by the Kerr effect and the light becomes elliptically polarized. This rotation of the polarization is small, and dependent on the material, but is also dependent on the incoming orientation of the light and the magnetic orientation of the sample. For imaging the incident light is directed through the standard optics of a microscope, where it is incident upon a magnetic film. The reflected, rotated polarization light is then passed back through the microscope optics and into another polarization filter (the "analyzer") that is crossed or nearly crossed with the first polarizer.

The handling of this section will also deal primarily with the Polar MOKE orientation, as most of the films addressed are perpendicularly magnetized films. The Polar MOKE is primarily sensitive to the magnetization vector that is perpendicular to the surface of the material (and thus in-plane with the incoming light). Other orientations of MOKE microscopy exist, and are useful for measuring the rotation of films that have a magnetization in the plane of the material. Longitudinal MOKE and Transverse MOKE geometries measure magnetization in the plane of the material by Where Polar MOKE uses incident light that is nominally perpendicular to the plane of incidence, Longitudinal and Transverse MOKE will work at a fixed angle to the normal of the surface. This angle is set by the hardware configuration of the system, and in microscopy

techniques is limited by the microscope objective aperture. Longitudinal MOKE is measured with the axis of the light and the axis of the magnetization sharing the same plane, as in Figure 21 below. It will be primarily sensitive to the axis of the magnetization along the path of the light, however the ellipticity values are lower than those of the Polar mode. Transverse MOKE is similar in appearance to Longitudinal, but instead of the light and magnetization paths sharing the same angle, the magnetization is crossed to the angle of light. This difference is illustrated in Figure 21. Transverse mode is primarily sensitive to the reflectivity from the surface (instead of an induced ellipticity change as in the Polar mode), where the Kerr vector either adds to or subtracts from the intensity of the reflected light. Transverse and Longitudinal sensitivity is typically lower than that of Polar mode, and due to lens and microscope geometries, special processing may be required to subtract out extra polar contributions to Transverse and Longitudinal modes.

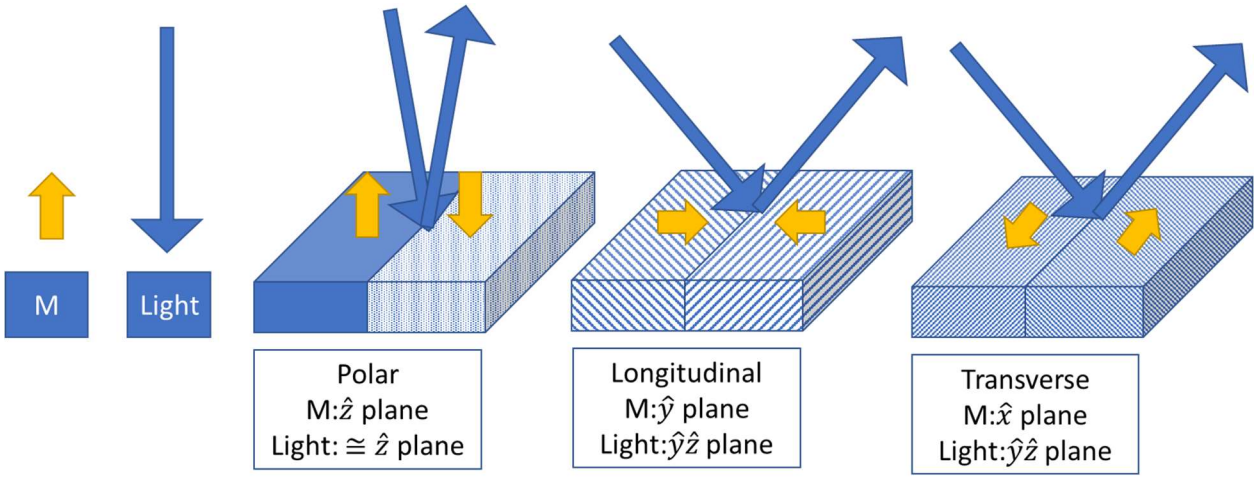

Figure 21: Representation of Polar, Longitudinal and Transverse MOKE.

For all of the modes, since the rotation of the polarization of light is proportional to the direction of the magnetization of the material, different magnetization directions give different rotations. With the crossed polarizer system, one of these rotations may be reduced in intensity (aligning the polarizer to cross exactly with this rotation). This will produce a “dark” area where

the polarization is exactly crossed with the reflected light, and a "light area" where the polarization is less crossed with the reflected light. These "dark" and "light" areas will correspond to the selected magnetic orientation and the opposing magnetic orientation – giving some idea as to the direction of magnetization of the material with the strongest Kerr effect.

As a convenient approximation, the analyzer is used to remove the background light of the microscope and leave only the rotated component of the illumination. This approximation and its implementation in technique will be addressed more fully in later components of this chapter. Unfortunately for the technique, signal sizes are small and there is still a certain amount of light coming through the optics and randomly scattered. To improve the signal to noise ratio and remove undesired background signals, an additional difference subtraction technique is also commonly used.

Along with the hardware based subtraction of the unrotated component of the incoming polarized light, a software and image processing technique is also used. This allows a sensitivity to any applied perturbation of the magnetic state. Typically, the system is magnetically saturated in order to remove any artifacts. Then with the perturbation applied, the change in the magnetic state of the material will be highlighted. When observing subtraction based Kerr imagery and data it is paramount to remember that this background and subtraction process can both enhance and hide detail, and draws only attention to what has changed since the background image was taken. In this work, typically images will be presented in this subtracted form (for better contrast). If of special interest, the background and un-subtracted image may be presented, but typically images will represent a system that has been either relaxed or perturbed from a saturated magnetic state. This does pose issues with sample drift and vibration, where over time the sample stage or optics may drift and create an erroneous subtraction signal. In principle, measurements are best done in

real time, or over the course of minutes. With special preparation, this can be extended to tens of minutes or an hour, but at that point it is often easier just to take smaller steps or reimage the background.

Chapter 2, Section 3:
Evico Magnetics Kerr Effect Microscope

In the Evico Magnetics Kerr Microscope system, there are 3 provided water-cooled high field custom electromagnets. One hollow core ring electromagnet capable of up to ± 107mT $\hat{z}$, a larger cone-bolt electromagnet capable of ± 900mT $\hat{z}$, and a rotatable in-plane electromagnet capable of ± 300mT $\hat{x}$. The in-plane magnet can be hand rotated through 360º which allows access to a variety of sample and field geometries. For the ring magnet and in-plane magnet, the sample is mounted on an X/Y/θ stage which allows translation and rotation of the sample. For the cone bolt high field magnet, only XY translation is available on a paddle stage. For temperature work, a sealed temperature stage is available. While it is capable of reaching temperatures up to 890K, it can also be used in open air mode to temperatures around 330K. The system provides high resolution imaging of magnetic domains with 660nm/pixel and 250nm/pixel at 20X and 50X magnifications respectively. Selectable illumination controls allow smooth transition between polar, longitudinal and transverse Kerr imaging modes.

Chapter 2, Section 4:
A Mathematical Basis for Kerr Microscopy

A ray of light is typically represented by the direction and phase of its electric field vector. In this case, for a ray of light traveling in the $\hat{z}$ direction, the light could be represented by the equation:

$$\vec{E} = (\hat{x}a + \hat{y}be^{i\delta})E_0 e^{-i\omega t - ikz}$$

Where E_0 is the magnitude of the electric field vector, a and b describe the relative strength of the electric field along the $\hat{x}$ and $\hat{y}$ axes (with the constraint that $|a|^2 + |b|^2 = 1$), and $e^{i\delta}$ describes phase delay information between the $\hat{x}$ and $\hat{y}$ components. The overall phase of the wave can be described by the $e^{-i\omega t - ikz}$ component, which describes common phase shared by a and b. If we aren't interested in the phase of the overall wave (and thus are only interested in the relative phase of the $\hat{x}$ and $\hat{y}$ components), it is possible to write the system in a Jones vector as:

$$\begin{pmatrix} \vec{x} \\ \vec{y} \end{pmatrix} \text{ which gives } \begin{pmatrix} a \\ be^{i\delta} \end{pmatrix}$$

In this formalism, it is also possible to write optical components as matrices. For example, a polarizer whose optical axis is aligned along the X-axis is represented by:

$$\begin{pmatrix} 1 & 0 \\ 0 & 0 \end{pmatrix}$$

Y axis polarizer: $\begin{pmatrix} 0 & 0 \\ 0 & 1 \end{pmatrix}$

Polarization rotator by θ: $\begin{pmatrix} \cos\theta & -\sin\theta \\ \sin\theta & \cos\theta \end{pmatrix}$

Retardation plate by δ: $\frac{1}{\sqrt{2}}\begin{pmatrix} e^{i\delta} & 0 \\ 0 & e^{-i\delta} \end{pmatrix}$

These matrix elements act upon the expression for the light as standard vector multiplication. When acted upon by an element, such as a linear polarizer, the action takes the form of

$$I_{out} = P_{polarizer} I_{in}$$

$$\begin{pmatrix} a \\ 0 \end{pmatrix}_{\substack{transmitted \\ light}} = \begin{pmatrix} 1 & 0 \\ 0 & 0 \end{pmatrix}_{polarizer} \begin{pmatrix} a \\ be^{i\delta} \end{pmatrix}_{\substack{incident \\ light}}$$

Thus, any optical element can be represented by a matrix describing its behavior along relevant axes. This may be a 2X2 matrix or 3X3 matrix depending on which elements are involved. We can now begin to describe the actions of a more complex surface upon the reflected light.

Below is the dielectric permittivity tensor that describes reflection from a surface involves the gyration vector $\vec{g}$:

$$\hat{\epsilon} = \begin{pmatrix} \varepsilon & ig_z & -ig_y \\ -ig_z & \varepsilon & ig_x \\ ig_y & -ig_x & \varepsilon \end{pmatrix}$$

When the system is a non absorbing medium, there is a requirement for $\vec{g}$ to be real. However, the Kerr reflection is not a lossless reflection, and occurs with a directionality that depends on the orientation of the magnetization of the surface of the film. Instead of a static, real gyration vector presented above, corrections must be made to include both the direction of magnetization ($\vec{m}$) and a complex parameter Q. This complex parameter is the Voight material constant that describes the magneto-optical rotation of the plane of the polarization of the light. This same constant addresses both the Faraday effect (while the light is in transmission), and the Kerr effect for reflection.

$$\vec{g} = Q \cdot \vec{M}$$

Replacing $\vec{g}$ with its new form, the above matrix representation can be rewritten, with the vector components of $\vec{m}$ expanded out:

$$\hat{\epsilon} = \begin{pmatrix} \varepsilon & iQm_z & -iQm_y \\ -iQm_z & \varepsilon & iQm_x \\ iQm_y & -iQm_x & \varepsilon \end{pmatrix}$$

As a note, for anisotropic materials, there is an additional term that can affect the reflection due to the square of the magnetization. This second order term is important for crystalline materials, or systems with long range structural order on the magnitude of the spot size. It is omitted here since the thin film materials discussed are amorphous. For the polar Kerr effect case, for just the reflection in the $\hat{z}$ direction, it is possible to write the dielectric permittivity tensor as:

$$\hat{\epsilon} = \begin{pmatrix} \varepsilon & iQm_z & 0 \\ -iQm_z & \varepsilon & 0 \\ 0 & 0 & \varepsilon \end{pmatrix}$$

According to the expression for the Maxwell's equations, the dielectric term often expressed as

$$\vec{D} = \varepsilon\vec{E}$$

Is normally used to link the electric flux density ($\vec{D}$) to the electric field vector ($\vec{E}$). In this case, coming from the complicated permittivity tensor expression, it is possible to write the term as:

$$\vec{D} = \varepsilon\left(\vec{E} + iQ\vec{m} \times \vec{E}\right)$$

Which shows up again with the equation for a beam of light. For a media with refractive index n and aforementioned propagation vector $\vec{k}$, the normal Maxwell equations for a plane wave in an anisotropic medium is:

$$\vec{H} = n\hat{k} \times \vec{E}$$

$$\vec{D} = -n\hat{k} \times \vec{H}$$

If simplified by inserting the expression for $\vec{H}$, the end result is

$$\vec{D} = n^2 \left(\vec{E} - \hat{k}\left(\hat{k} \cdot \vec{E}\right)\right)$$

With $\vec{E}$ and $\hat{k}$ perpendicular, and recalling the dielectric permittivity tensor earlier, we can express this set as:

$$\vec{D} = \begin{pmatrix} \varepsilon E_x & iQE_y & 0 \\ -iQE_x & \varepsilon E_y & 0 \\ 0 & 0 & \varepsilon E_z \end{pmatrix}$$

Which suggest that for a nontrivial solution, the determinant of the matrices must be zero. This leads to an expression for the refractive indices of:

$$(n^2 - \varepsilon)^2 + q^2 = 0$$

Solving for the refractive index gives us two available solutions for the positive and negative indices.

$$n_+^2 = \varepsilon - iq$$

$$n_-^2 = \varepsilon + iq$$

This set of actions decomposes the action of the magnetic reflective surface into a set of refractive index expressions. By treating a light wave as a sum of circularly polarized waves (left hand and right hand), it is possible to show that the net effect of this reflection is to change the light wave from linearly polarized light to elliptically polarized light. Now, instead of staying along

the $\hat{x}$ direction, the net electric field vector will appear to precess around the direction of propagation with a characteristic frequency. Treating the linearly polarized light now as a sum of two waves – one left circularly polarized, and the other right circularly polarized, we can write

$$\vec{E} = \begin{pmatrix} \sin \omega t \\ \cos \omega t \end{pmatrix} + \begin{pmatrix} -\sin \omega t \\ \cos \omega t \end{pmatrix}$$

If only for the sake of simplicity, we assign the refractive index equations as:

$$r_+ = \frac{1 - n_+}{1 + n_+} \qquad r_- = \frac{1 - n_-}{1 + n_-}$$

So when the waves are incident on the surface and are reflected, there is a change in the propagation of the LCP and RCP components of the system according to

$$\vec{E} = r_+ \begin{pmatrix} \sin \omega t \\ \cos \omega t \end{pmatrix} + r_- \begin{pmatrix} -\sin \omega t \\ \cos \omega t \end{pmatrix} = \begin{pmatrix} (r_+ - r_-) \sin \omega t \\ (r_+ + r_-) \cos \omega t \end{pmatrix}$$

Which now is no longer a linearly polarized system! This reflection from the magnetic surface has resulted in an ellipticity of the system. This ellipticity has a ratio of major/minor axis of:

$$\phi = \frac{(r_+ - r_-)}{(r_+ + r_-)} = \frac{n_- - n_+}{1 - n_+ n_-}$$

It is this angle – or more specifically this ellipticity in the reflected light, that will form the basis of the imaging of the sample. This is the signal, which is typically on the order of several thousandths of a degree. The signal rotation is very small, and must compete against the background counts that will pass through the microscope. It is important to realize that a normal MK1 eyeball and a CCD camera are not sensitive to the ellipticity of the light. In addition, a normal polarizing filter will not address the ellipticity of the light. So while a Kerr effect microscope has been described as being sensitive to the rotation of polarization of light from a magnetic surface,

that is not necessarily exact in its description. Instead, as seen by the mathematics above, the Kerr effect induces an ellipticity in the otherwise linearly polarized light. So this now elliptical polarized light (a superposition of circularly left and circularly right polarized light) must be corrected back to linearly polarized light.

Thus, instead of a simple "analyzer", a true Kerr effect microscopy system requires a compensator/analyzer pair. The compensator is an ordinary quarter wave plate on a rotation stage. This optical element forms an angle θ with respect to the horizontal plane, and on the microscope can be rotated through approximately $10°$ of angle by the mounted slider. The equation for the quarter wave plate with angle θ is;

$$e^{-i\frac{\pi}{2}}\begin{pmatrix}\cos^2\theta + i\sin^2 2\theta & (1-i)\sin\theta\cos\theta \\ (1-i)\sin\theta\cos\theta & \sin^2 2\theta + i\cos^2\theta\end{pmatrix}$$

With a light ray that has an induced ellipticity, picking a proper angle of θ will change the ellipticity of the light (from the two circularly polarized components) into a superposition of two linearly polarized components. From here, it is a simple matter to bring in the final crossed linear polarizer which will remove the initial unrotated light. Overall, the path of the beam through the active optical elements is:

$$Unpolarized \rightarrow Linear\ X\ polarizer\ ("Polarizer") \rightarrow Sample\ Reflection$$
$$\rightarrow {}^{1}/_{4}\ waveplate\ ("Compensator") \rightarrow Linear\ Y\ polarizer\ ("Analyzer")$$

However, the one element not yet considered is the final element in the system – the camera. With a CCD camera, there is a bit depth to the camera that is designed into the hardware. Essentially, each pixel is capable of detecting a number of levels equal to the $2^n$of its bit depth. So an 8 bit camera would be capable of detecting 256 (a 0-255 range) of different intensities. A 10 bit

camera would be capable to detecting 1024 (a 0-1023 range) different intensities. This becomes critical when it comes to discerning the Kerr signal from background noise. The measure of Dynamic Range (DR) indicates how many counts of signal a system will produce for a given input irradiance. DR is related to signal count by

$$Counts = \frac{Background\ Signal}{Dynamic\ Range}$$

So it is clear that simply creating more background signal will improve the number of counts on the camera. However, the camera has a saturation limit inherent to the binning of electrons within the pixel. "Simply" creating more light at the input has a hard limit on the detector end. If we take a look at the strength of the dynamic range within the system, we come up with a ratio of signal (rotated by the Kerr Effect):

$$DR = \frac{\left|\tilde{\tilde{E}}_o\right|^2}{\tilde{\tilde{E}}_o\tilde{\tilde{E}}_K^* + \tilde{\tilde{E}}_0^*\tilde{\tilde{E}}_K}$$

Which can be simplified without much loss of generality to a small angle approximation of:

$$DR \approx \frac{\sin\theta}{10^{-3}}$$

Where θ is the rotation of our analyzer to the incoming reflected light (already with Kerr signal in it). If we take for example a Kerr rotation of $0.001°$, with perfectly crossed polarizers ($\theta \approx 0$), the system will generate a Kerr signal irradiance level of approximately 10^{-6} (the Kerr signal is smaller than background by a factor of 10^{-6}). This is nearly undetectable by most non-specialized hardware, and expecting to configure a system in this way would likely be

exceptionally expensive. In order to generate 1 count of Kerr signal on the camera, the system would need 10^6 counts of background signal – likely well above the hardware limit of the camera. Stripping away another level of idealization, the camera is not a perfect noiseless system. A typical non-specialized CCD camera will have somewhere between 2-4 counts of noise on average per pixel. This corresponds to thermal noise, radiation noise, shot noise and other effects within the camera itself. Thus, a single count of Kerr signal would be completely lost within the noise.

However, not all is lost. If the polarizers are perfectly crossed, this creates an excellent extinction (reducing the signal from the background). However by slightly increasing the angle of the analyzer, it is possible to create a higher dynamic ratio. By opening the analyzer by 5 degrees, the system will generate a dynamic range of approximately 90 – and for a background count of 900 or so, this creates around 10 counts of actual Kerr signal. While increasing sample irradiance will obviously help, at a certain point, there is a limit to the maximum intensity that the camera can accept. Maximizing the contrast and available Kerr signal intensity takes a delicate adjustment of both the analyzer and compensator. For each sample, adjusting this pair for maximum contrast will be important for the microscopy technique.

The Faraday effect discussed earlier is similar in form and function to the Kerr effect. Again, where the Kerr effect is due to the reflection of light from the surface of the film, and is sensitive to the magnetization direction of the material with the highest Kerr rotation, the Faraday effect is due to the transmission of the light through the material. Similar to the above treatment of the mathematics of the Kerr effect, the magnetic permeability of the material used for the Faraday effect is shown below.

$$B(\omega) = \begin{pmatrix} \mu_1 & -i\mu_2 & 0 \\ i\mu_2 & \mu_2 & 0 \\ 0 & 0 & \mu_Z \end{pmatrix} H(\omega)$$

This is then applied to give the angle of rotation of the polarization in the material by:

$$\beta = \gamma B d$$

With β as the angle of rotation, d is the path length through the material, B is the magnetic flux density along the direction of propagation and γ is the Verdet constant for that particular material. As an aside, this effect may also be effective in observing the difference in circularly polarized light with different orientations (left-handed circular and right-handed circular).

So far, this section has concerned itself with the hardware and optics side of Kerr microscopy. In practice, this is often the least of one's concerns after the contrast has been set. If the system were limited to the raw image coming from the microscope CCD, evaluating the domain patterns would be a difficult task. However, with the advantage of computerized image processing, it is possible to perform a background and subtraction technique that will remove the background signal and isolate the change in the Kerr signal.

The addition of computer image analysis significantly improves the ability to observe and track domains. By taking a background image and then applying a perturbation, it is possible to track the change in domain walls due to the perturbation. This can be especially useful for a number of techniques, directly observing the local behavior of magnetic domains.

Chapter 2, Section 5:
Kerr Microscopy Imaging Techniques.

For the Kerr Microscope, techniques for observing magnetic domains are slightly different than an ordinary microscopy technique. [3] As the system must deal with low signal levels and materials dependent signal, it is primarily a subtraction technique. This can lead to several different potentially unintended effects, and may require discretion by the researcher or observer. Features may be emphasized, or deemphasized depending on the imaging choices for background and subtraction. This may have the effect of showing (Figure 22), or hiding (Figure 23) features, or can show features that are no longer present (Figure 25). This section will address some issues with the microscopy technique and present some options for reducing those issues.

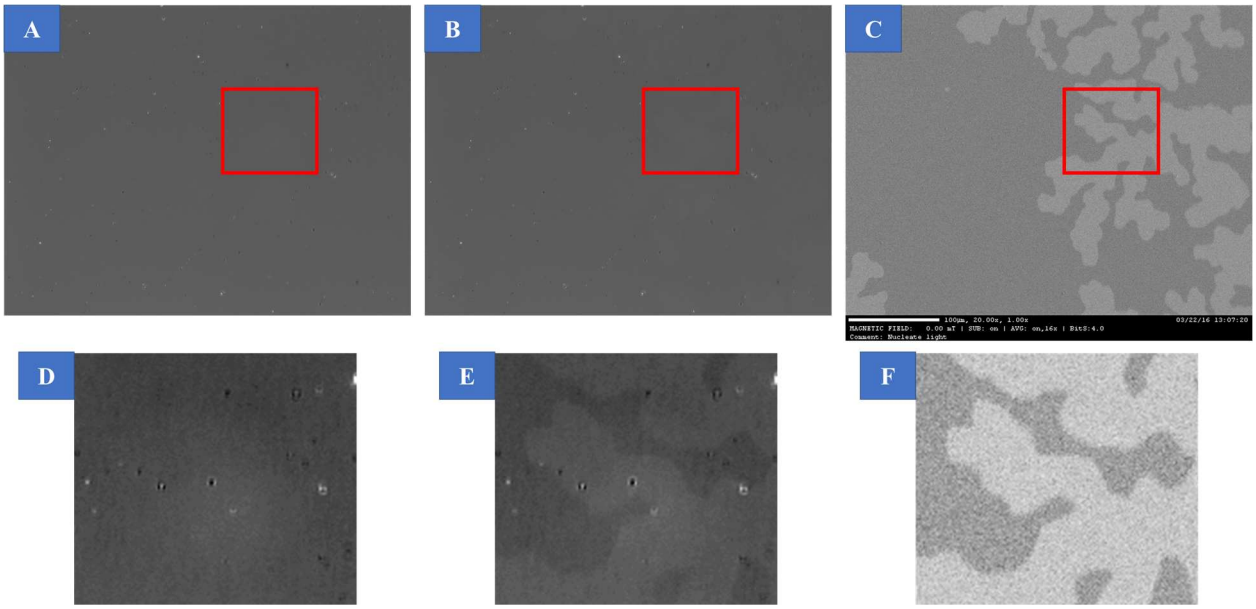

Figure 22: Example Kerr microscopy image showing background and subtraction. Kerr microscopy of Pt/Co/Os2A/Pt film showing Background: (A with enhanced contrast inset D) Unsubtracted: (B with enhanced contrast inset E), and Subtracted: (C with enhanced contrast inset F). Inset boxes in A-C are 100 micrometers square. Insets D-F have been enlarged 300% and contrast has been adjusted by hand.

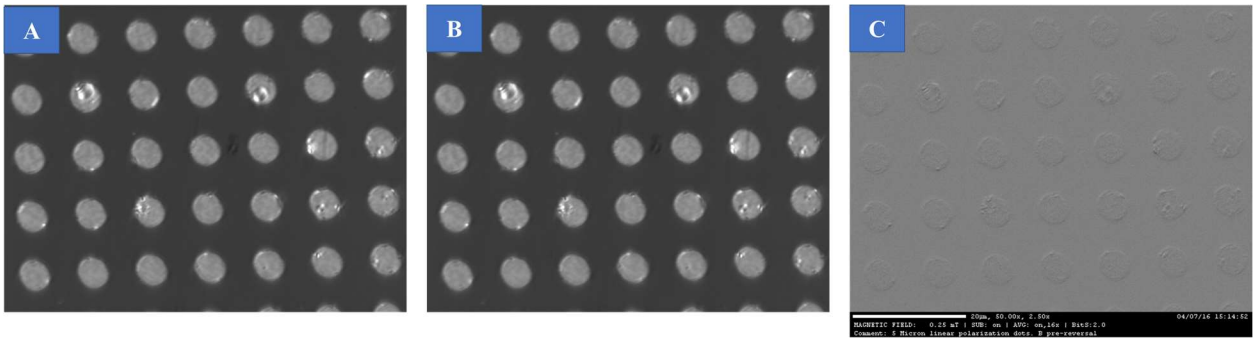

Figure 23: Example Kerr microscopy image showing subtraction of lithography features. Kerr microscopy of 5 micrometer dots. Background image (A), Current image (B), and resultant subtracted image (C). No perturbation has been applied to the system between the background and current images. 5 micometer dots were chosen to show the effect of image subtraction on lithography features under Kerr microscopy.

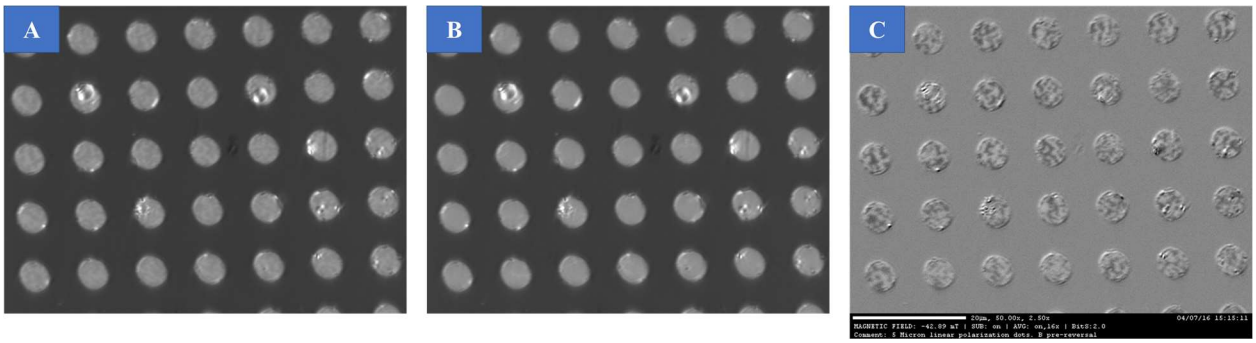

Figure 24: Example of Kerr microscopy image showing magnetization in lithography feature. Kerr microscopy of 5 micrometer dots. The same background image from Figure 21 was used (A), however a 45mT field has been applied in the -Z direction for the current image (B). This results in a magnetic switching of some regions of the dots, as seen in the subtraction (C). Small movements of the sample stage result in the outlines of the lithography features becoming more apparent in the subtracted image (C).

Figure 22 shows the importance of the subtraction technique. [3] The film as shown in the background image A has small defects that are due to either deposition defects or microscopic dust that has deposited on the sample. Some defects that reach into the film will affect the propagation and formation of magnetic domains, while other defects like surface dust may not. With the currently displayed image in B, a sharp eye may notice some change in the intensity of the image, but even with manually increased contrast in the case of E, the pattern is still murky. Additionally, simply increasing the contrast from B to E has resulted in the defect sites being emphasized. With the subtraction image C, the contrast for the magnetic domain has been significantly improved to

the point where the magnetic domains are visible even without additional adjustment. When such adjustment is done, as in F, the magnetic domains are even more apparent while the defect sites that were prominent in D and E have been removed.

However, even with increased contrast in an image that a domain pattern can be difficult to discern. Especially while printing in journals, or presenting at conferences, contrast levels for Kerr images can be challenging for the viewer to observe. Attempting to compare the unsubtracted background image to the post-perturbation unsubtracted image is difficult. However, once the subtraction process occurs, the signal is amplified significantly while the other background elements are suppressed. This is important for imaging, but also comes with a few caveats that are important to remember.

Due to the subtraction process, any motion of the optics or sample stage between the background image and the current image will produce a significant distortion in the image. False bright or dark spots will significantly reduce the visibility of any actual magnetic signal. With the inherent sensitivity necessary to amplify the small Kerr signal, signal drift becomes a significant problem. While hardware and software elements are available to perform physical stabilization (through piezo element positioning and image feedback), or through computational stabilization (through pattern identification and matching), there is still some level of motion that becomes impossible to correct. Some care must be taken in experiment design to ensure that the timescale of the measurement is shorter than the timescale of expected drift. Fortunately, with the drift on the order of several minutes, all but the most specialized of techniques will be available.

Another issue for the system is the design of the perturbation so that a single background image can be used for the analysis of a series of perturbations. In the example of Figure 22, a magnetic domain, oriented along $M^{\uparrow}$ is nucleated with the help of an application of magnetic field.

A background image taken at this point will show the domain nucleated as a light image on grey background. However, if a new background is taken, the current image will become a part of the grey background. Any perturbation will create a “donut” of change in the domain. If this causes a shrinkage in one wall and an expansion of the other, a slice of “bright” contrast and a slice of “dark” contrast may evolve, showing where the domain has shifted from its previous position.

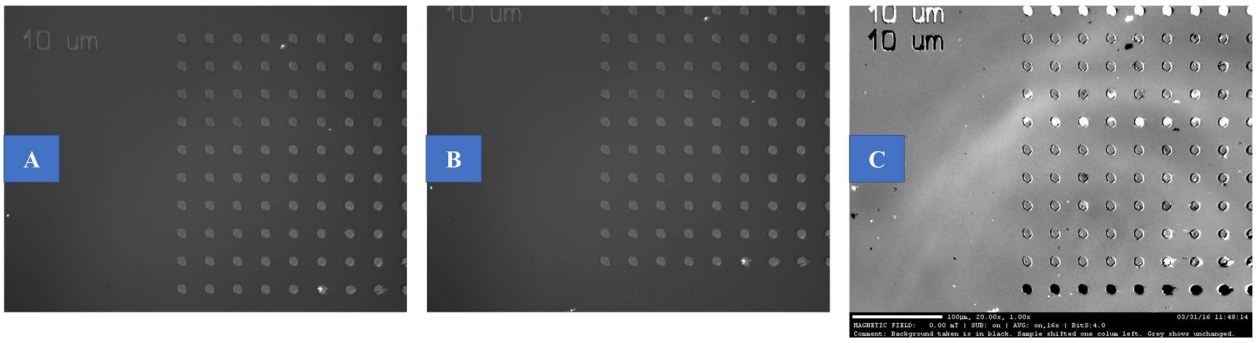

Figure 25: Effect of motion of the sample stage. Between the background (A) and current (B) image, the sample stage was moved upward 1 lattice period (20 micometers). This manifests as a set of dark textures in the now empty regions (bottom), and a light feature where the dots now are. This can also be seen in the two “10um” text features at the top left.

This can be addressed most easily by magnetically saturating the sample to a single direction, and then nucleating the domain walls from the saturated film. Thus, the new image will prominently display the domains that have formed as a result of the perturbation applied. This helps in subtracting the background artifacts resulting from any debris on the sample after lithography This can be quite useful for samples that are less than perfectly clean, but can also hide defect points which may be important for domain pinning or nucleation.

A set of high field electromagnets for in-plane and out-of-plane magnetic field is a common addition to the microscope. Two major considerations need to be addressed. The first is mechanical torque that can be exerted by the magnet on other magnetic components of the microscope or sample stage. While the magnetic moment of the thin film samples is insufficient to create deflection within the magnetic field of the coils, any microscope components with ferrous

components (set screws, optics components, sample stage) can cause issues with physical deflection of those components.

Another issue that can arise, especially with large out-of-plane fields, is that the optics components themselves can be susceptible to an induced magneto-optic rotation in the lens material. [3] This rotation, seen in the below magnetic hysteresis loop is an issue when trying to observe at large field ranges. One significant issue in using the Kerr microscope for large ranges of magnetic field is that this parasitic effect can be substantial – obliterating both signal and background range. Thus, it is common to either select the compensator/analyzer pair within a more linear range for the sample, do one transition edge at a time, or to attempt to balance the top and bottom ranges of the contrast. Moreover, fringing field effects from the large electromagnet can make this effect especially strong for low contrasts.

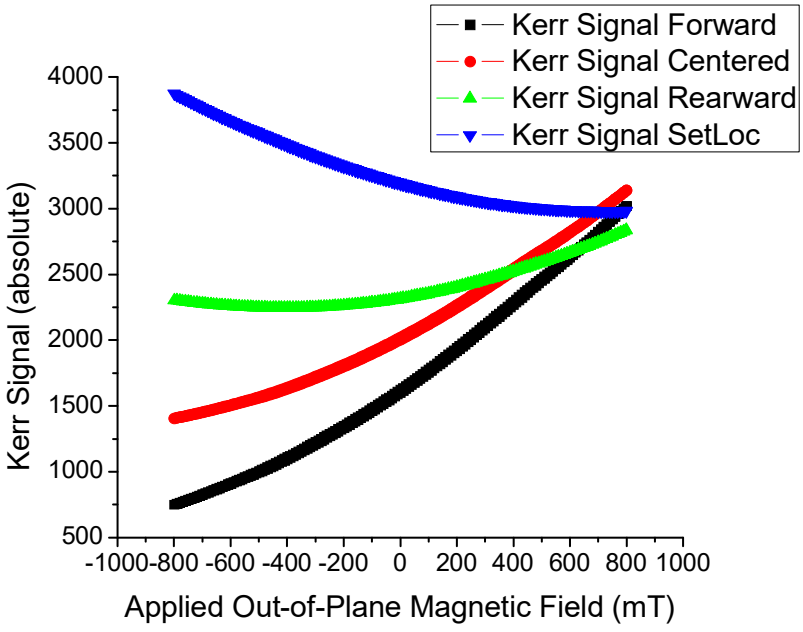

Figure 26: Aberrant signal from a non-magnetic silicon sample. 4 different compensator/analyzer positions are shown. This signal is primarily composed of nonlinear effects from the optics, and is not from the sample itself. Typical magnetic signal for actual samples may be between 100 and 400.

Another effect of the background-subtraction process is the reduction in the visibility of debris and lithography features as seen in Figure 23 and Figure 24. This can be beneficial at times by removing the visual cues of surface debris from the image. However, for nucleation defect sites like those presented in the below figure, or for constrained geometry lithography features, this can result in a confusing image.

With care as to the preparation of images, the Kerr microscope can be an excellent tool for displaying the local behavior of magnetic materials and systems. With good resolution, good sensitivity to perturbations, and high flexibility, the microscope forms the backbone of local scale magnetism measurements.

Chapter 3:
You, Me, and Co-Tb.

The controllable manipulation of magnetic domain states forms a crucial link in modern data storage technology. For spinning disk hard drives, magnetic information is stored by writing domains on the magnetic platter. For the next generation of magnetic nonvolatile memory or magnetic random-access memory, information is stored in magnetic domain walls. Thus, there is a need for control of both magnetic domains and their corresponding domain walls. [17] [18] [19]

In a hard drive, the writing of domains on the hard disk platter itself has been accomplished by the application of a magnetic field created by the write pole. This field-based effect acts on the moment of the recording grain and must overcome the anisotropy of the material. While certain effects may work to improve this efficiency, there is a hard limit in effect: namely that for a given moment and anisotropy of the material, a certain amount of raw field is required. The discovery of All-Optical magnetic switching through a short laser pulse changed this equation. Several papers by this group had proven that it was possible to reverse the magnetism with a pulse of light, but it was the discovery of All-Optical Helicity Dependent Switching (AO-HDS) that brought significant interest to HAMR based technologies. [20] [21] [22] [23]

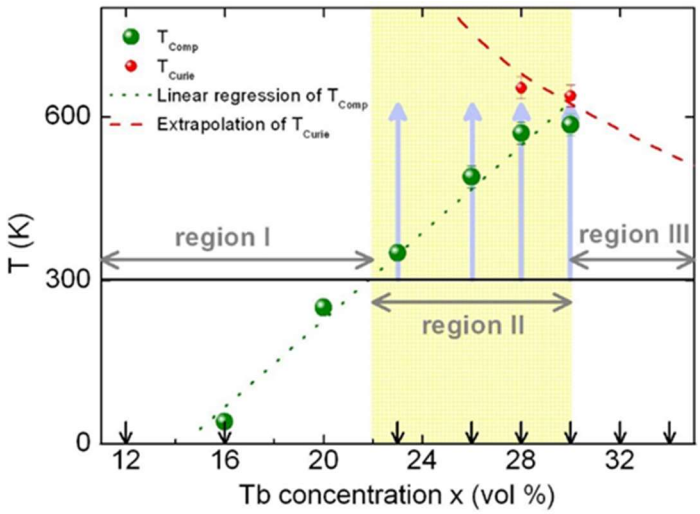

Figure 27: Optically Induced Switching ranges in CoTb films. Figure by Alebrand, S. *[24]*.

In this dissertation, the Cobalt-Terbium system will be evaluated from several angles. A study of the growth of the layers highlights the transition between alloy-like behavior and thicker multilayers. Previous work as seen in Figure 27 has confirmed a linkage between the HAMR and AOS behavior of the CoTb alloys and their composition. This composition effect is greatest with a range of CoTb compositions between 23%Tb and 29%Tb [25] [26]. As will be shown later, this composition dependent effect has a signature observable in the temperature dependence of the material.

Both cobalt and terbium are interesting materials in their own right. [27] Cobalt, along with iron, are some of the highest magnetic moment materials, and can be engineered for both extremely high and extremely low anisotropy. With a high Curie temperature of 1400K, cobalt is significantly useful in many magnetic applications. Terbium is ferromagnetic only below 219K (far below room temperature), and paramagnetic below 230K, which limits its use as a pure material in magnetic applications. By mixing the two materials, it is possible to involve the high moment with the Tb materials with the above room temperature Curie temperature of the Cobalt. However, when placed into multilayers or alloys, the two materials will form independent sublattices that are

oppositely aligned. This creates a ferrimagnetic film with two temperature dependent, antiparallel moment sublattices. Since, the magnetization are coupled anti-ferromagnetically, the net moment in the sample goes to zero. As a result of this differential temperature dependence, the overall film will have a temperature dependent effect known as a magnetic compensation point (T_M). When the moments of the two sublattices are equal in magnitude and opposite in direction (as enforced by the antiferromagnetic coupling of the Co and Tb sublattices), the film will have a zero net moment. At the compensation point, the magnetic moment becomes 0, but the anisotropy of the film is unaffected. Thus H_c diverges at the compensation point. Using these two effects – the change in the net moment of the film, as well as the diverging coercive field, the behavior of the multilayer and alloy samples can be quickly discerned. These systems are easy to study because of their high moment and excellent Kerr microscopy contrast, which makes them excellent candidates for both current generation and next generation material systems. [28] [29]

Chapter 3, Section 1:
Alloy to Multilayer Transition and Properties

For this dissertation work, a range of compositions and multilayer types was studied. This provides a look at the material properties from a range of compositions within the interesting area for HAMR/AOS, as well as a range of multilayer thicknesses from co-sputtered alloy to a range where the bulk effects begin to dominate layer behavior. [24] [30] The growth of these materials is of significant interest, as the growth processes outlined in Chapter 1 can affect the end result. While different deposition conditions and techniques were examined, the standard 3mTorr, 50SCCM Argon flow, 3mTorr process, room temperature conditions were used. A wide range of samples were evaluated, with a total layer thickness between 20 and 50nm (typically 25nm), compositions between 70% and 90% Tb, and a multilayer period stack of 2 to 18 Ångstrom. This transition from the alloy phase to thicker multilayers is apparent in the effect on the moment, coercive field, and compensation temperature of the samples. [31] [32] [33]

The overall phase-space for this system has two axes. At one axis, the composition of the samples, given in atomic % Co versus atomic % Tb. As the two different atomic layers prefer different growth configurations, an approximation is used to determine the amount of each atomic specie in the overall film. For the alloy samples, the gun calibration rates in Angstrom/sec were converted to an atomic % and the two materials were co-sputtered with the deposition rates controlled by adjusting the output power of the gun. In order to deposit multilayers, a set period of thicknesses of the Co layer were selected (I.E. 2Å Co, 4Å Co, 6Å Co and so on), and the proper ratio of the Tb layer thickness was calculated. The overall thickness of the sample was kept within the range of 25nm (250Å) but more attention was paid to an integer number of layer repeats of the

specific thickness. For very large layer thicknesses (around 20% of thickness), the number of layers becomes small and the material starts to lose coupling between the Co and Tb layers.

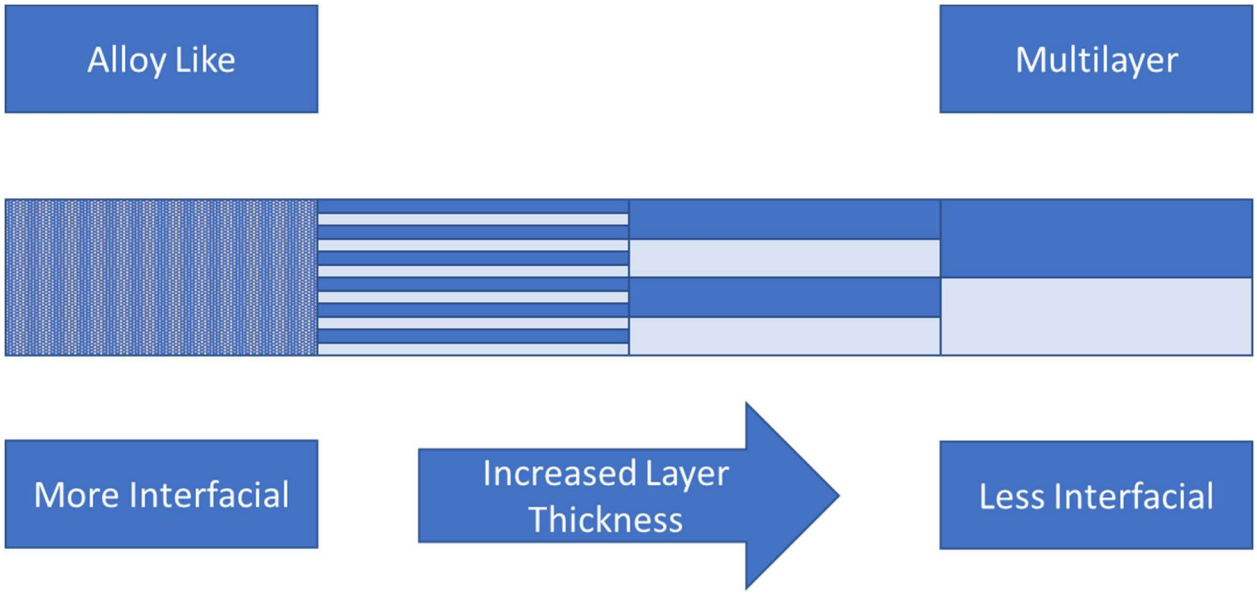

Figure 28: Alloy to multilayer transition example. This illustrates reduced interfacial effects as stacks become thicker. At very high thicknesses, layers will have reduced coupling and interaction, and the interfacial coupling will be reduced with respect to the rest of the system.

This can produce edge effects due to the uncoupled interfaces at the top and bottom. Nominally with the Co-Tb multilayers, each Co layer will be sandwiched by two identical interfaces to a Tb layer. For certain systems, the growth direction matters sufficiently to differentiate the two interfaces, but for the repeated Co/Tb/Co/Tb layers, these differences are not significant to the behavior of the sample. Tantalum was chosen for the surface capping layers because of its low effect on the magnetic properties of the sample. [34]

Magnetic hysteresis loops of the samples show a variety of interesting effects. One artifact to identify in the sample measurements is the two-step hysteresis loop with the second step around 0 mT as shown below in Figure 29. Much of this artifact is due to edge deposition on the side of the substrate, and can be removed in the analysis phase.

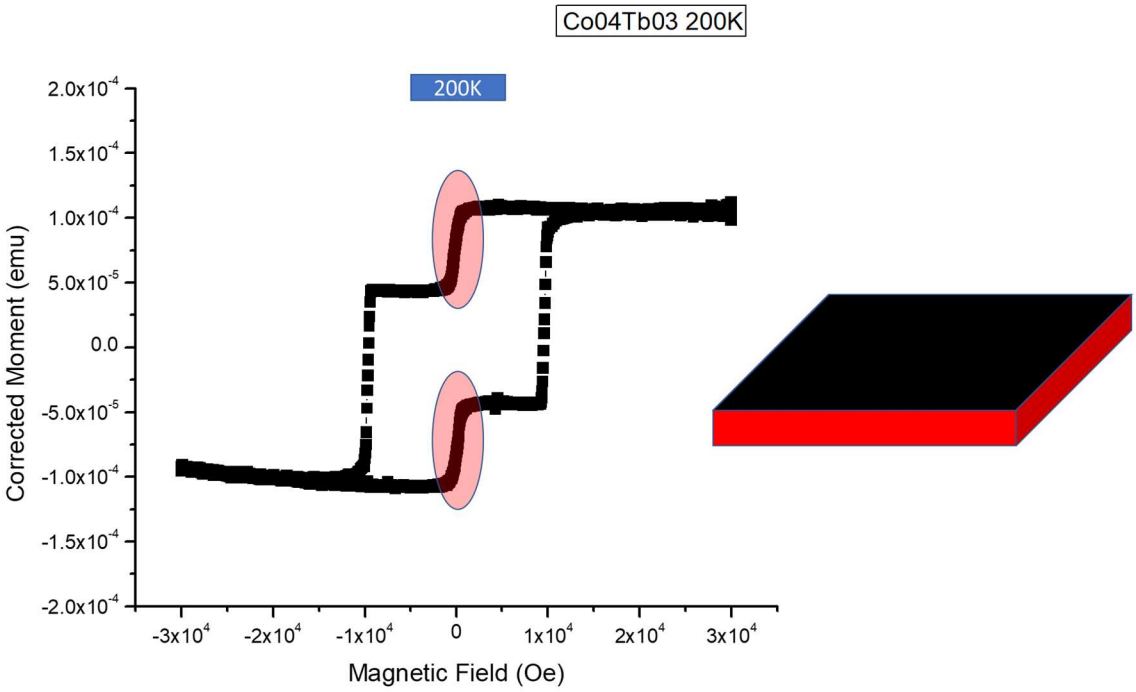

Figure 29: VSM data showing CoTb edge deposition effect. The step around 0 field is a result of deposition on the sides of the sample, as shown in red on the right image. This will result in incorrect magnetic moments versus volume, as well as the emergence of the soft phase as marked. This step is not observed in a Kerr microscope.

The edge deposition issue as shown above has been corrected for future samples by surrounding the VSM sized substrates with sacrificial pieces. As noted in the VSM measurements section, the VSM system will measure the moment of all material in the bore, including the sides and bottom of the substrate. By surrounding the sample to be measured in the VSM with additional substrates, the edges are protected from deposition of unwanted material. While substrate material intensive (requiring 8 total pieces to create 2 edge-protected pieces), this can produce samples without the edge deposition effects. Measuring the as grown samples with VSM, these effects can later be removed through data processing and fitting. This effect is not seen under Kerr microscopy, due to the local nature of the Kerr magnetometry measurement.

VSM measurement of the samples reveals a few interesting effects. As shown in Figures 31 and 33, the temperature dependence of the moment is linear for the samples through a wide

range including the compensation point. The samples were evaluated from 75K to 400K with the intent of finding the compensation temperature. The linearity of the moment versus temperature was also used to project the probable compensation points for the material.

Of specific interest is the sample as shown in Figure 30 where the compensation temperature exists around 350K – a little above room temperature. The linearity through the compensation point is most visible here. By plotting the "shoulders" of the hysteresis curve as shown in Figure 33, it is possible to remove the contribution of the side-deposited material. Fitting these shoulders to their intersection (points 1 and 4, and points 2 and 3), gives their convergence at 0 net moment. The convergence of the net moment also shows the divergence of H_c the coercive field. As the Zeeman energy of the film is due to

$$E_{zeeman} = \int_V \vec{M}_{net} \cdot \vec{H}_{applied}\, dV$$

and the reversal of the sample due to external field involves the Zeeman energy overcoming the anisotropy energies, a system exactly at the compensation point cannot be switched by external field. This can be seen as the system approaches compensation – where the coercive field will diverge due to the decrease of the net moment.

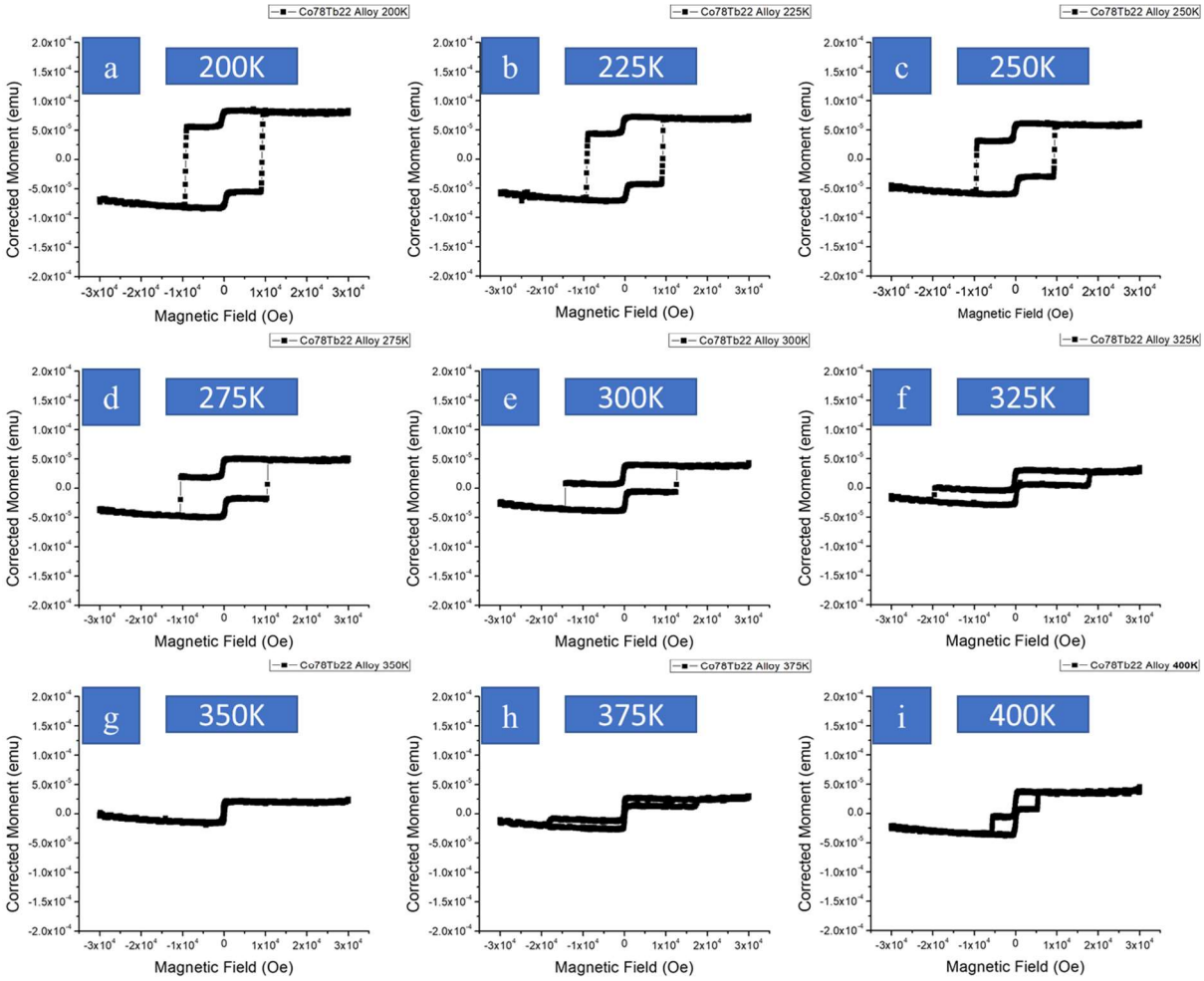

Figure 30: VSM moment versus field for $Co_{78}Tb_{22}$ alloy sample. Temperature is changed from 200 Kelvin to 400 Kelvin in steps of 25 Kelvin. Images (a) through (f) are below the compensation point – indicated by the divergence of the coercive field and absence of net moment around (g). As the system moves to the hot Cobalt dominant region of its magnetic phase map, the moment appears to re-open in (h) and (i). Magnetic moment is not corrected to moment per volume due to the ill-defined sample volume as previously discussed.

There has been interest in this particular behavior of the system as it relates to the optically induced switching of the film. As seen from the above critical field driven switching data, the system properties change dramatically with the application of heat.

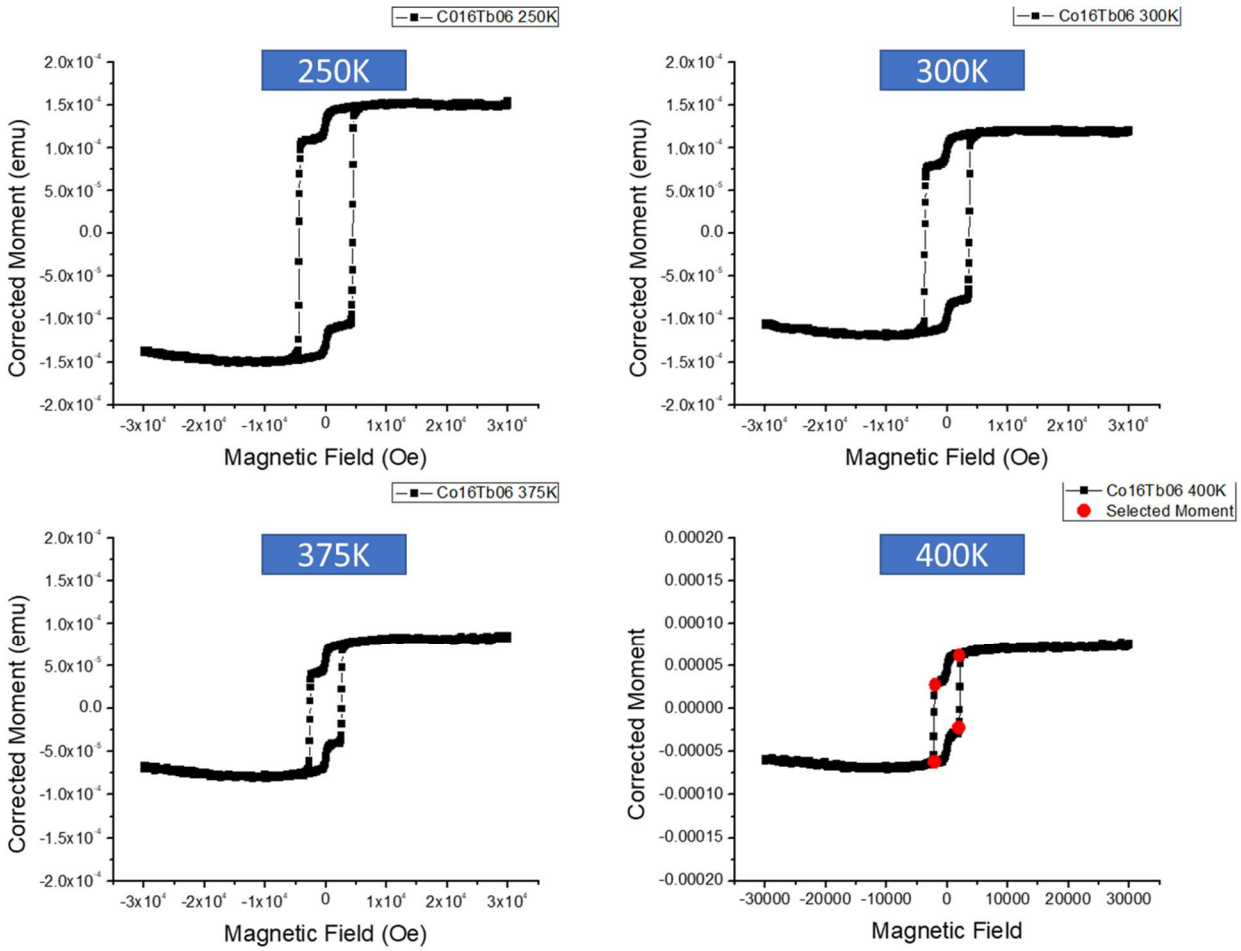

Figure 31: VSM moment versus temperature for a Co87%, Tb12% multilayer. Of note is the contribution from the edge deposition which creates a secondary step around 0 applied field. By selecting points on each side of this shoulder as denoted in red in the bottom right figure, it is possible to perform a comparison to find where the loop will close.

By fitting out the saturation moments versus temperature, it is possible to create a reasonable estimate of the compensation point of the material. This fitting was supported by both direct observation of the convergence, as well as the fitting of multiple samples as shown above. This allows for a wide ranging analysis of the temperature of the compensation point both above and below room temperature.

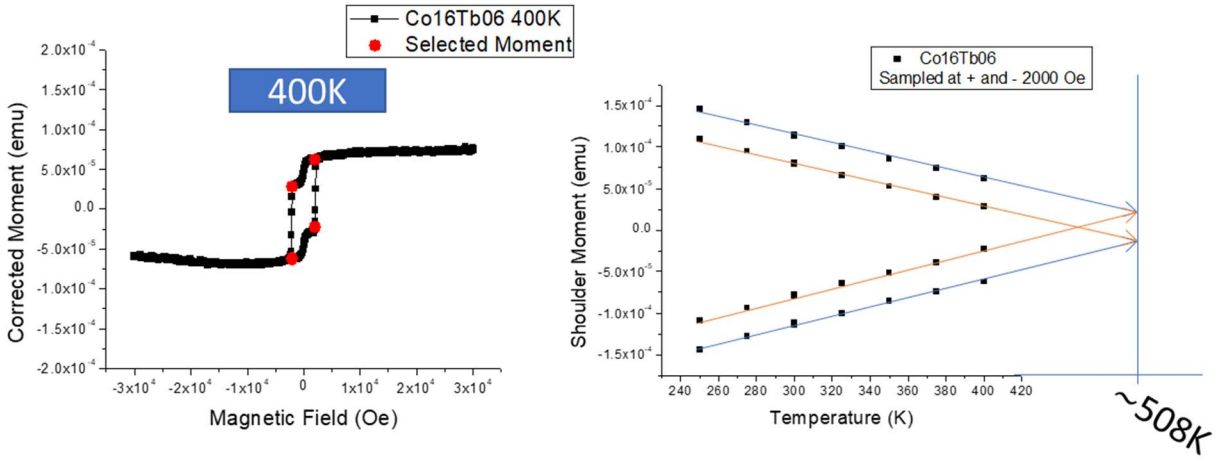

Figure 32: Finding compensation temperature from selected shoulder moments. The points as shown on the left image are linear fit versus temperature. This effectively removes the extra unwanted contribution from the extra side-deposited material.

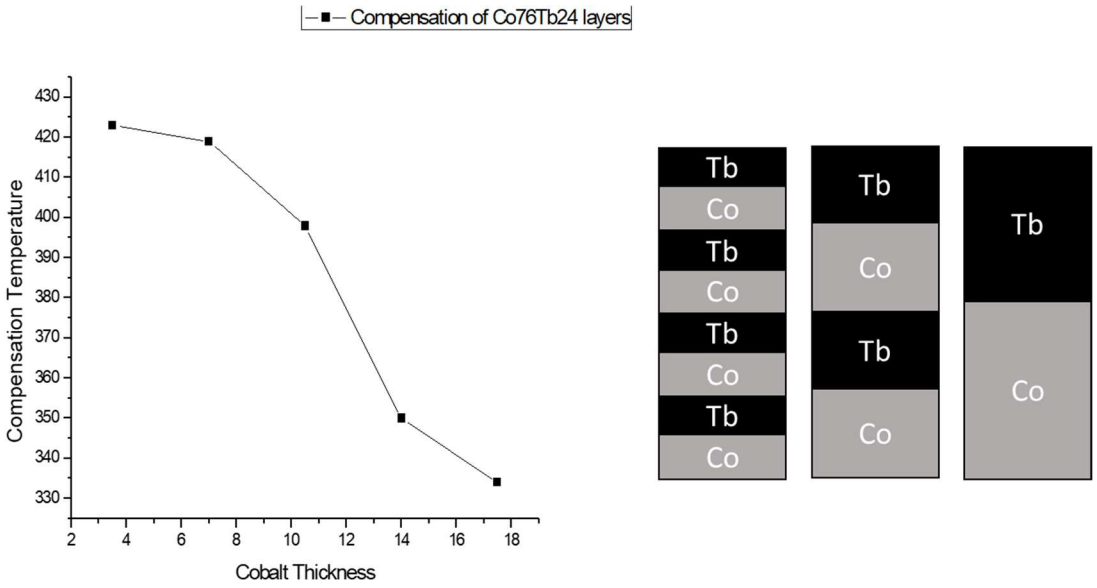

Figure 33: Compensation temperature (T_M) versus layer thickness for $Co_{76}Tb_{24}$. Samples are indexed by the layer thickness of the Cobalt layer to help with indexing. The ratio is 3.5nm of Co to 3nm Tb for the $Co_{76}Tb_{24}$ layers.

Using this technique, it is possible to track the T_M versus layer thickness for multiple samples. For the $Co_{76}Tb_{24}$ sample shown above, the compensation point can be affected by around 80C as it transitions from alloy-like multilayers to bulk-like multilayers. This is consistent and predictable across the different material compositions, and shows a clear transition from the high

temperature compensation point of the alloy to a behavior closer to a superposition of the bulk Co and bulk Tb behavior. This is consistent across the different compositions of material.

The interest in the AOS has made the analysis of this behavior useful. More recent evaluation of the AOS and AO-HDS behavior has indicated a strong effect of the fast and ultrafast dichroic heating performing a modification of the sublattice dominance. [24] [35]The system, beginning at room temperature, crosses the composition point due to heating when exposed to the ultrafast laser pulse. Therefore, as an initial basis for the analysis of these samples and the effect, finding the composition that supports a compensation-crossing is important. However, as seen in the data presented above, performing this analysis by VSM technique has a heavy investment in time. Additionally, in some of the AO-HDS and AOS samples, there was a range of behavior. For certain samples that did not exhibit deterministic switching in a blank field, there was the ability to "pull" a nearby domain wall with the application of a laser pulse. [36] For these samples, it was theorized that a short range thermal gradient could cause a domain wall to move.

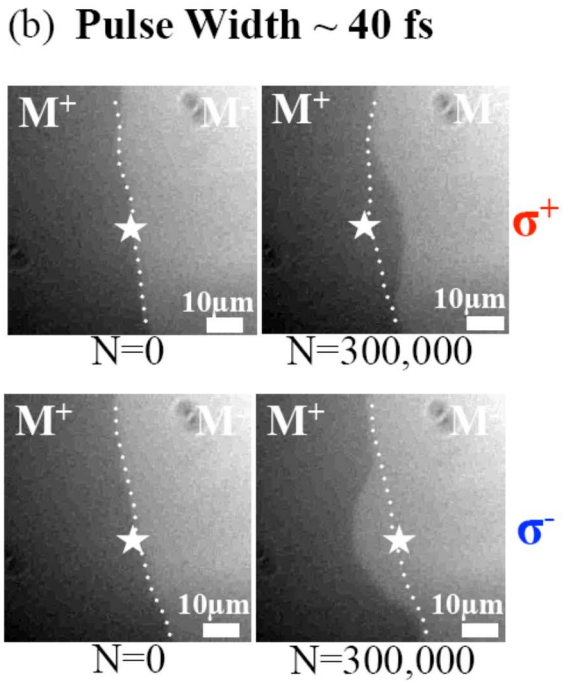

Figure 34: Helicity dependent movement of domain wall in Pt/$[Co/Pt]_{x3}$/Pt. Layers and measurements made by Y. Quessab, et al. This demonstrates a complex effect in moving domain walls in AOS media by both laser helicity and local temperature gradients. *[37]*

Chapter 3, Section 2:
Thermal Domain Wall Propagation

Domain wall motion and logic in thin patterned wires offers significant potential for the future of data storage and processing. A version of domain wall based "racetrack" memory proposed by S. Parkin [17] suggests using spin torque driven domain walls to move stored data. These devices rely upon spin torque phenomena which links the flow of magnetically polarized electrons in a material, and can drive the domain walls within the devices. In order to be efficient, these devices require low domain wall pinning, [38] high domain wall velocity [39], efficient deterministic motion, and annihilation resistant domain walls. For the CoTb system, there was interest in investigating both the potential for this type of system as well as some of the energy-assisted magnetic recording (HAMR/MAMR) phenomena. [24] [40] [41]

Thus, in this chapter, we present small devices that were patterned with e-beam lithography from the $Co_{78}Tb_{22}$ alloy material. These devices were designed in a variety of geometries, but the consistent features of the system are a set of contacts for electrical current, a thermal gradient choke ("nucleation site") at one side of the sample, and a thermal sink ("expansion pad") at the other end of the system. Driving a joule heating current through the system will produce a localized hot spot at the nucleation site. Heat will flow through the wire, creating a thermal wavefront that propagates until it reaches the expansion pad. At this location the lower current density and greater heat dissipation of the increased surface area will provide a heat sink. Domain wall motion due to spin torque was not observed, likely due to the large depinning fields inherent, and the large magnitude of the Joule heating. [30] [42] [43]

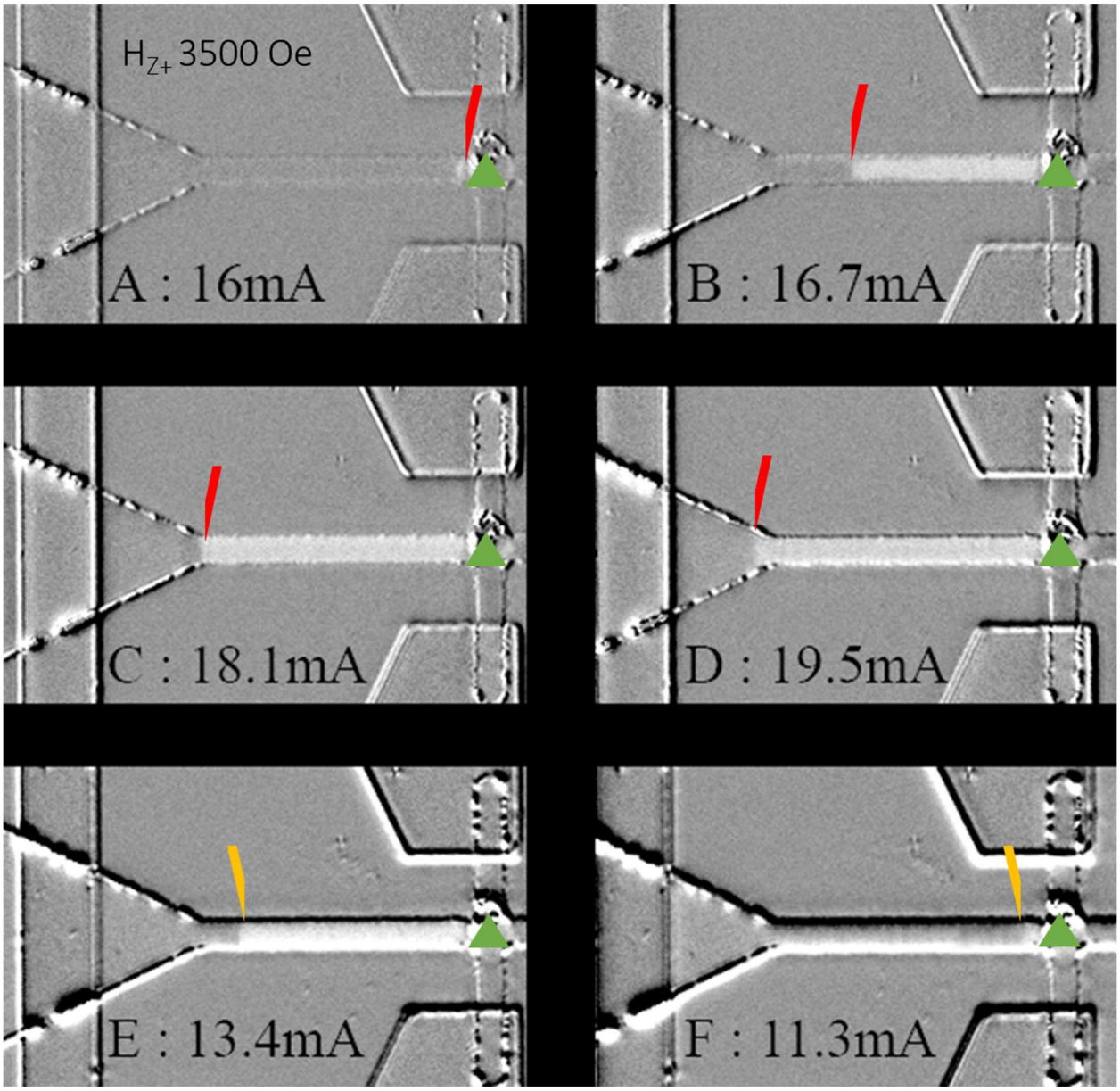

Figure 35: Current application movement of thermal gradient in 2µm $Co_{78}Tb_{22}$ alloy device. 3500 Oe of external magnetic field is applied in the +Z direction, and the current annotated at the bottom of each image flows from the right nucleation site (green arrow) toward the left expansion pad. This shows formation and extension of the thermally driven domain wall (A, B and C), the extension of the thermal gradient into the expansion pad (D), the reduction of power and retraction of the gradient (E) and the complete collapse of the nucleated domain as the system cools below the annihilation temperature (F). An example is shown in Supp. Video 1.

Thus, with an application of a certain power output, the temperature of locations along the wire can be controlled by the thermal gradient. This makes the technique useful for creating a local

heating and driving domain walls by temperature gradients. When used with Kerr microscopy and the CoTb samples, the local magnetization of the Cobalt sublattice can be observed. As the Kerr rotation of Cobalt is much greater than the Kerr rotation of Terbium, the system will be tuned such that the propagation of the thermal gradient is evidenced by the switching of the Cobalt sublattice. [3]

For the experiment, an out-of-plane magnetic field was applied of sufficient magnitude to saturate the net magnetization in the +Z direction (positive out of plane). This resulted in the low temperature dominant Tb lattice controlling the rotation of the film. Thus, the Co sublattice is aligned to the -Z direction (negative out of plane). Upon heating of the sample through the compensation point, the dominance of the two sublattices will switch to where the net magnetization rests along the direction of the high temperature dominant Co sublattice. However, while the net magnetization can be altered by heating the sample through the compensation point, this does not by itself rotate the Cobalt sublattice to which the Kerr microscope is most sensitive.

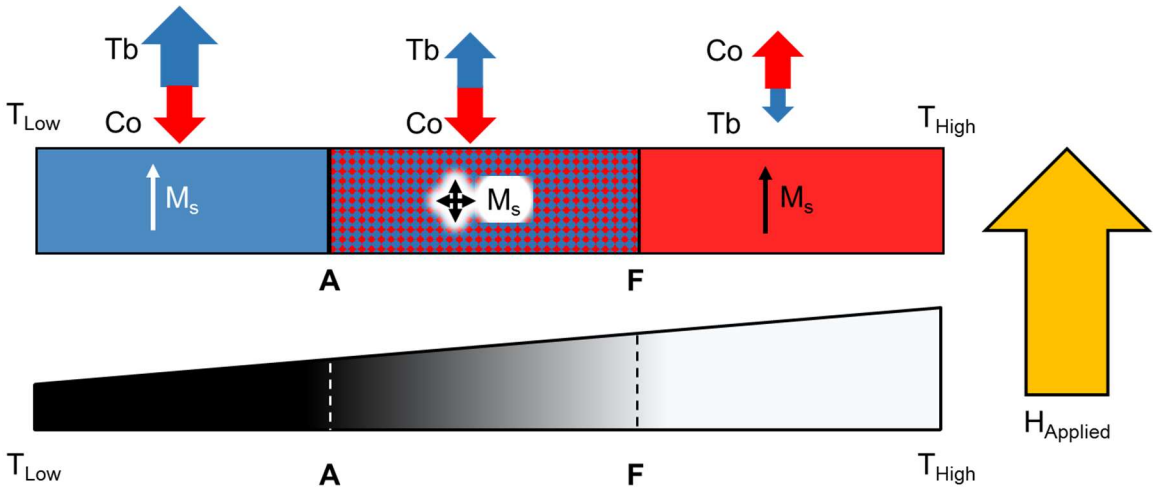

Figure 36: Three regions approximation. At low temperature (left) the Tb dominant region orients the sublattices of the film along the dominant Tb sublattice. At high temperatures on the right, the hot Co dominant region orients the system along the Co sublattice. In the center, the indeterminate region neither sublattice has sufficient dominance to rotate the film, and so it remains in whichever

state it held previously. It is important to note – this switching behavior depends on the strength of the applied field H_z, and a higher field will result in a narrower indeterminate region.

This calls upon the "three regions" approximation as shown above in Figure 36. The first region is the cold, Tb dominant region where net magnetic moment is along the Tb sublattice and the applied field and net magnetic moment of the film are large enough to orient the film along the axis of the field. The third region is the hot, Co dominant regime where the net moment is along the Cobalt sublattice orientation, and the applied field orients the net moment along the axis of the field. The intermediate region close to magnetic compensation, displayed in the center of the figure is the transition between the Tb dominated and Co dominated temperature regimes. In this second region, the net moment of the film is insufficient to orient it along the applied magnetic field.

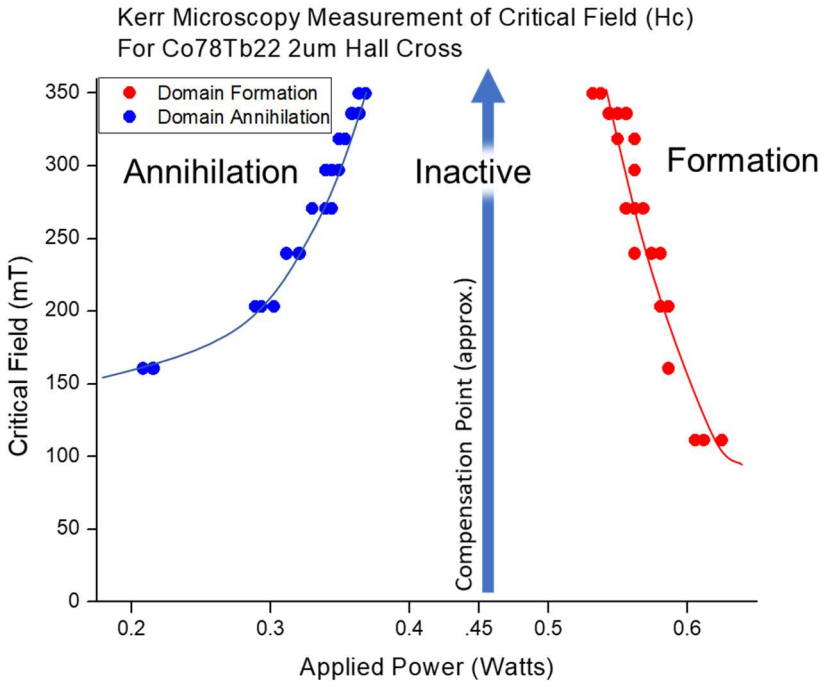

Figure 37: Nucleation and annihilation behavior versus field and heating. The "three regions" approximation can be applied to the motion of the domain wall within the sample. A fixed field was applied, and the current was scanned until the domain wall nucleated at the nucleation site and propagated to the expansion pad. The divergence of the critical field around the compensation point is shown as it requires significantly more field to switch around the compensation point.

Thus, two factors control the propagation of the observed domain wall – the applied external field, and the temperature of the sample. It is important to note again however, that the microscope technique is primarily sensitive to the orientation of the Cobalt sublattice, and is not as sensitive to the net magnetic orientation of the film. Thus, the wall edge as observed traces out the location of the transition from the indeterminate region to either the Cobalt dominant (hot) or the Terbium (cold) regions. The transition from either region into the indeterminate region is not marked by a change in the Kerr image. The width of this effective transition will depend on the strength of the applied field.

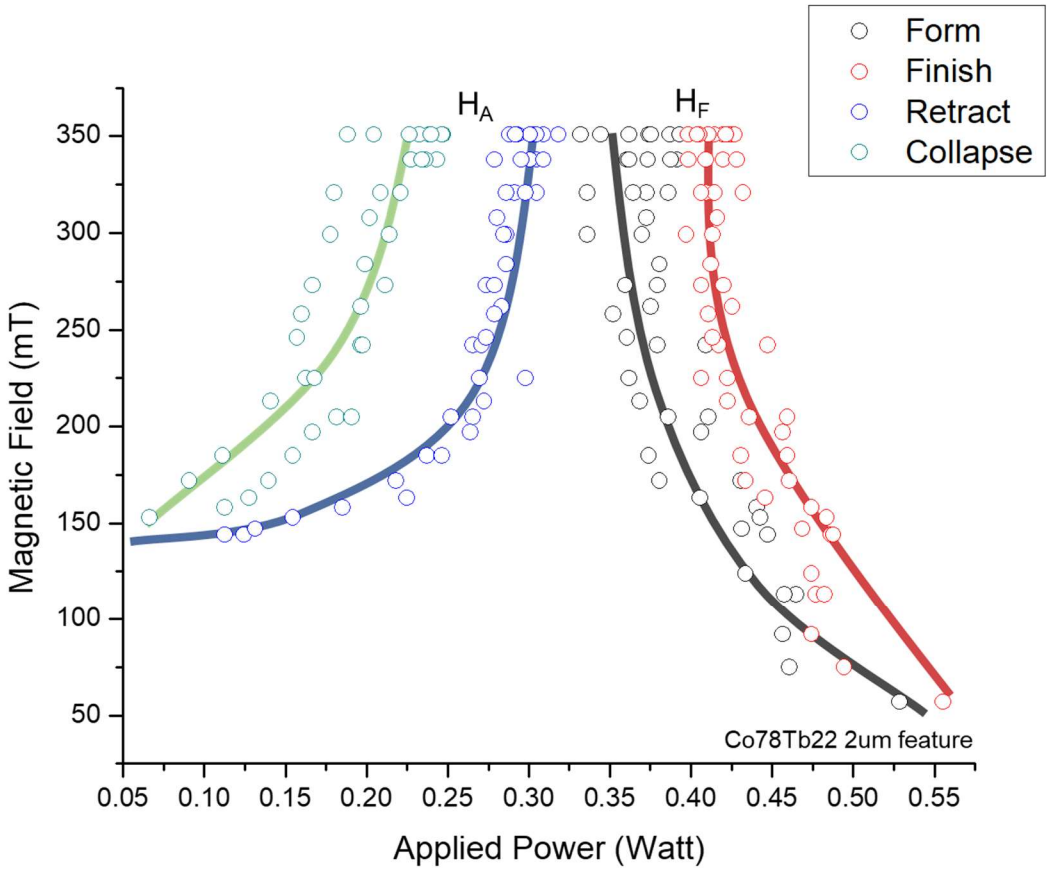

Figure 38: Formation / Annihilation curves for Sample 1. This shows the Form and Finish curves (where the domain wall forms at the thermal gradient nucleation site, and moves into the expansion pad, respectively), and the Retract and Collapse curves where the domain wall retracts from the expansion pad and returns to the thermal gradient nucleation site, respectively.

The temperature of the sample is most well defined at the transition point of the domain wall itself. However, controlling the temperature directly is difficult. In order to provide an effective temperature axis for the measurement, the power applied to the sample was taken as the effective control axis. The measurement was done by increasing the power at a set rate and measuring the position of the domain wall rotation. The position of the domain wall follows the nucleation and annihilation temperatures as seen in the "three regions" approximation, and by moving the domain wall rotation in respect to the power output, a map between applied joule-heating power and domain wall motion is created.

The outcome of a single measurement is a set of points describing the amount of power required to nucleate the domain wall at the engineered defect, the amount of power required to move that domain wall to the end of the expansion pad, and then the amount of power reduction required to trace that domain wall back from the expansion pad to the nucleation site. This set of measurements strongly replicates the domain wall temperature hysteresis curve, except it is done at a single field. By measuring across the field axis as well, it is possible to trace a set of material and feature dependent curves (as shown below) that describe the temperature response of the device and its base material, providing for a fast phase analysis of the system.

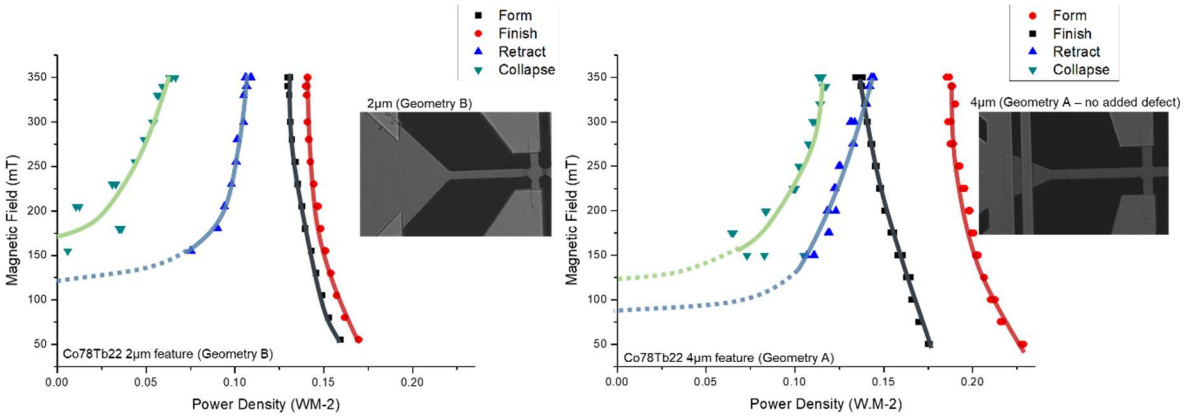

Figure 39: Additional test geometries and curves. The formation and annihilation curves are presented for two additional devices (inset). This shows effects for different expansion pad geometries (left), and larger 4μm wires (right).

This set of curves provides for not only a window into the system, but also the potential of controllably placing a domain wall within the feature. By tracing out a path on the above set of formation curves it is possible to controllably place a domain wall within the feature.

As an example, the for the curve path shown below in Figure 40 heats the system while under applied field. As the nucleation site crosses the field/temperature line shown under "Nucleate", the domain wall moves out from the nucleation site in a manner controllable by the application of power. If the power is reduced before the domain reaches the expansion pad, the domain wall will stop. Then if the field on the system is reduced below the room temperature Retract/Annihilate line, the applied power can be reduced without annihilating the domain wall. Once the system is cooled, the domain wall will set into the Tb dominant direction, providing a true actual domain wall at that location, instead of only the sublattice domain wall.

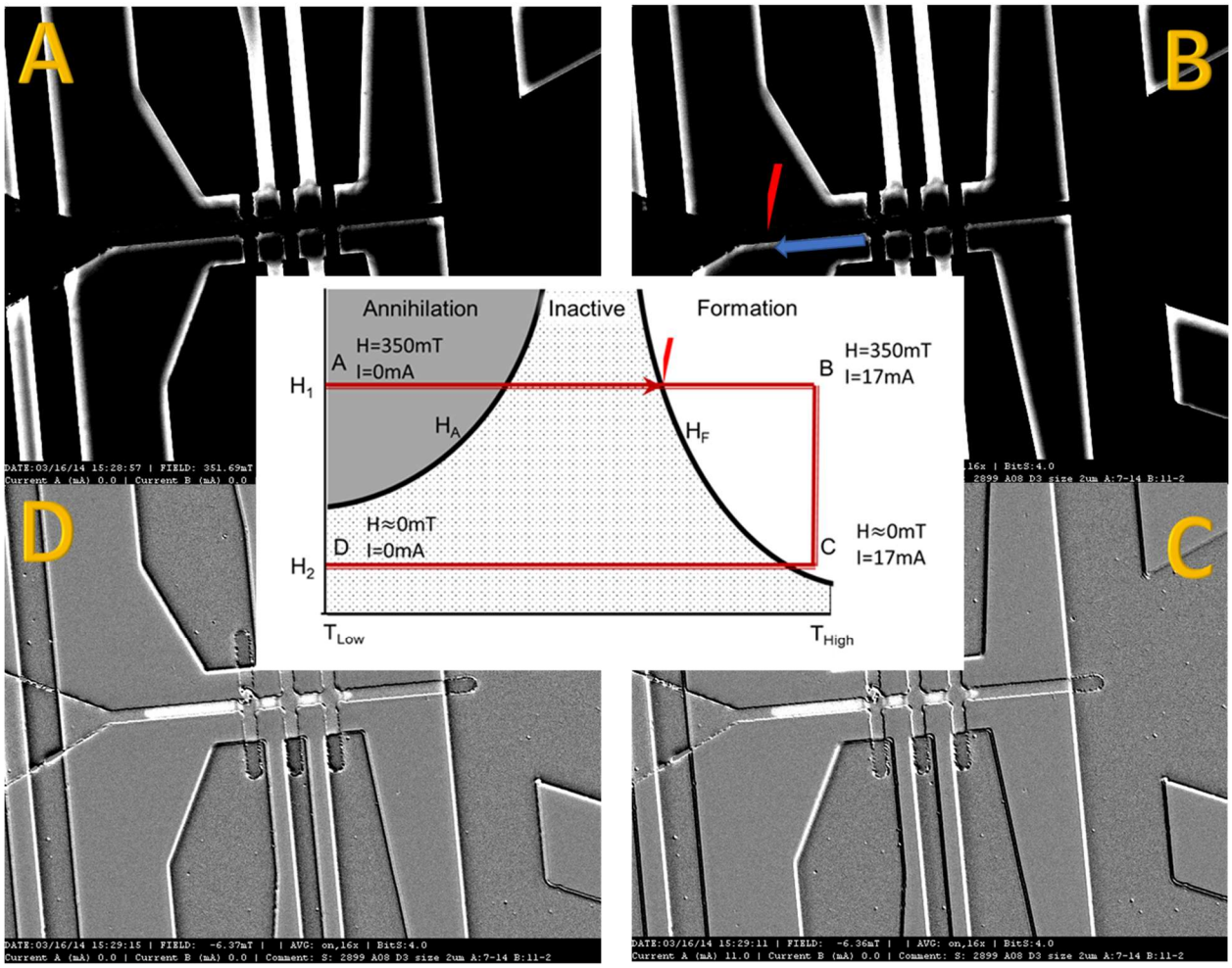

Figure 40: Controllable placement of domain wall using thermal gradients. Background images were taken at 0 applied field, then the field was increased to start with the film in saturation at "A". A and B appear dark because of the large aberrant signal from the lens optics. In "B" current is applied sufficient to move the thermal gradient into the wire, but not into the expansion pad. In C, the field is removed while the current remains on. The domain wall is clearly visible here. In D, the current has been turned off and it is observed that the domain wall has not moved.

This propagation and annihilation behavior can be used to adjust the position of the domain wall – while the system is in a state with the domain wall in the wire, the position of the thermal gradient can adjust the position of the Cobalt or Terbium dominant zones.

While likely unsuitable directly as a memory storage technology (requiring joule heating currents and the application of a localized magnetic field), this is also a demonstration of certain design limitations on future devices. Any domain wall motion type device will necessarily contend

with large currents through small features. A standard domain wall logic system using STT or SOT currently requires somewhere on the order of a current density of 10^{10} A/cm^2 [44]. While later in this dissertation, a new system will be examined with the potential to drastically reduce some of these drive requirements, standard domain wall logic will require design to avoid these kinds of heating effects.

However, this design does offer the potential for use with certain recording media technologies. As has been proven elsewhere [24] the CoTb system possesses features that are significantly interesting for use with a magnetic write head coupled to a local energy source. The current state of the art has limits on the longevity of the write element, but a promising future for areal density.

Chapter 3, Section 4:
CoTb in Review

In conclusion to this chapter, measurements of the ferrimagnetic system of Cobalt – Terbium multilayers and alloys were conducted. These showed a significant controllability of the magnetic compensation temperature through both the average atomic concentration and the period of single-specie multilayers. Devices were patterned from a film with a suitable compensation temperature, and a joule-heating current was used to drive a thermal gradient within the device. This thermal gradient drives a transition within the magnetism of the film. At "low" temperatures, the Terbium sublattice controls the magnetization. With sufficient heating, the Terbium lattice moment is reduced and the Cobalt lattice controls the orientation of the net magnetization. In an applied external magnetic field, the system will undergo a rotation from the Terbium-controlled magnetic orientation to the Cobalt-controlled magnetic orientation at a point across the compensation temperature. A model showing the orientation of the film under applied field and thermal gradient was proposed and tested. By varying the applied magnetic field and joule-heating power, a phase diagram was created of the behavior of the device. This shows the possibility of controllably driving the domain wall within the device through the use of the thermal gradient. Different devices were tested and produced similar results. Using the generated phase maps, it was possible to controllably place and manipulate the domain wall within the device as a function of joule heating current and applied field. While not directly suitable for memory applications, this offers an important look at the local magnetic behavior of the system through a temperature phase change. Combined with the control over film properties including the temperature of the compensation point, this experiment demonstrates the capacity to control the domain wall nucleation and propagation behavior with thermal gradients.

Chapter 3 in part is taken from research published as “Generation and manipulation of domain walls using a thermal gradient in a ferrimagnetic TbCo wire.” R. Tolley, T. Liu, Y. Xu, S. Le Gall, M. Gottwald, T. Hauet, M. Hehn, F. Montaigne, E. E. Fullerton, and S. Mangin in Applied Physics Letters 106, 242403 (2015). The dissertation author was the primary investigator and author of this paper.

Chapter 4:
The Wonderful Wizard of Os.

Novel memory technologiescan be enabled by new materials and/or novel phenomena.One way around the magnetic recording trilemma is to avoid it entirely through the use of new magnetic objects and / or textures. It has been shown that several of these objects may allow for higher storage densities, greater throughput and lower power requirements for magnetic data storage and processing. [45] [46]

One class of magnetic domain that have emerged as potential information carriers is skyrmions. Skyrmions are a type of magnetic soliton – a localized self-reinforcing orientation of magnetic spins. Named after Tony Skyrme, who proposed modeling nucleons as topologically-protected disturbances in field theory. [47] As an apocryphal story, he recalled having observed a swirling orientation of water waves traveling along a canal without dissipating for the over a mile. The observation of a stable orientation of a disturbance in the surface of the water invited a description of a topological object in a field surface. The method was first applied to describe mesons and baryons in a unified field theory, however it has also been used to describe the potential for a winding of a surface that would produce stable objects in an otherwise continuous vector field. Certain objects could be continuously deformed from one state to the other – taxonomically a glass bowl could be continuously deformed to a wine glass. However, a ceramic bowl could not be continuously deformed to a coffee mug with a handle, due to the hole for the handle. In magnetic systems, most domain walls are topologically equivalent – able to be continuously deformed from

one orientation to the other. [48] Skyrmions break this topological equivalency, rendering them distinct from other types of domain walls.

One of the major problems with traditional domain wall logic devices is that many domain walls are strongly affected by pinning and defect sites. Domain walls that are compressed together are inherently unstable and may either be ejected from the film by edge effects, or annihilated as a domain wall becomes too energetically unfavorable. An up/down/up/down pattern when compressed sufficiently will annihilate some of the domain walls and may result in an up/down pattern, which could lead to data loss in a recording application. Additionally, as seen in the CoTb system, some domain walls require large current densities in order to induce motion, leading to disadvantageous Joule heating effects.

To advance the concept of racetrack memory, or solid-state nonvolatile memories and storage in general, there is a need for magnetic structures with high mobility, high stability over time and high durability with respect to fields and pinning defects [39] [49].

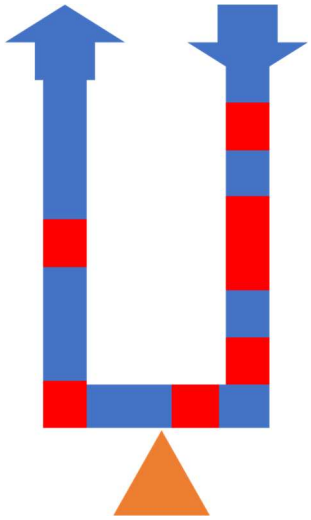

Figure 41: Basic racetrack memory schematic. Magnetic domains and domain walls (blue and red) are moved along a defined wire by current and/or some other perturbation. Read back by a fixed read head (orange triangle), the domain walls can be freely driven in either direction. This is an example of a potential next generation magnetic storage system. *[17]*

With the discovery and development of skyrmions first in bulk materials and more recently in thin-film heterostructures, there is a significant opportunity for racetrack memory architectures, given that skyrmions fulfill a number of the critical features for data storage and processing. Specifically, their theoretical structure creates a topological protection that protects them from defects and annihilation with other skyrmions. Additionally, their spin topology allows for motion using spin torques at much lower drive current densities than traditional domain walls [50] [51] [52] [49].

Structurally, a skyrmion consists of a single domain wall that winds itself into a self-supporting configuration. This structure behaves as a soliton, meaning that it possesses several particle-like characteristics. While normal Heisenberg exchange interactions prefer to orient adjacent spins along the same direction through the $S_1 \cdot S_2$ energetics of the system, if there exists an additional energy term of the form $S_1 \times S_1$ (previously discussed as the Dzyaloshinskii Moriya Interaction or DMI), it is possible that having neighboring spins canted relative to each other may lead to a more energetically-favored state. This has the effect of lowering the domain wall energy of the system. At long ranges, this additional term would significantly reduce the stability of the uniform magnetic ordering. However, with the chiral nature of the DMI term one possible energetically favorable solution is for the spins to form a self-supporting structure by closing their winding, thus forming a skyrmion.

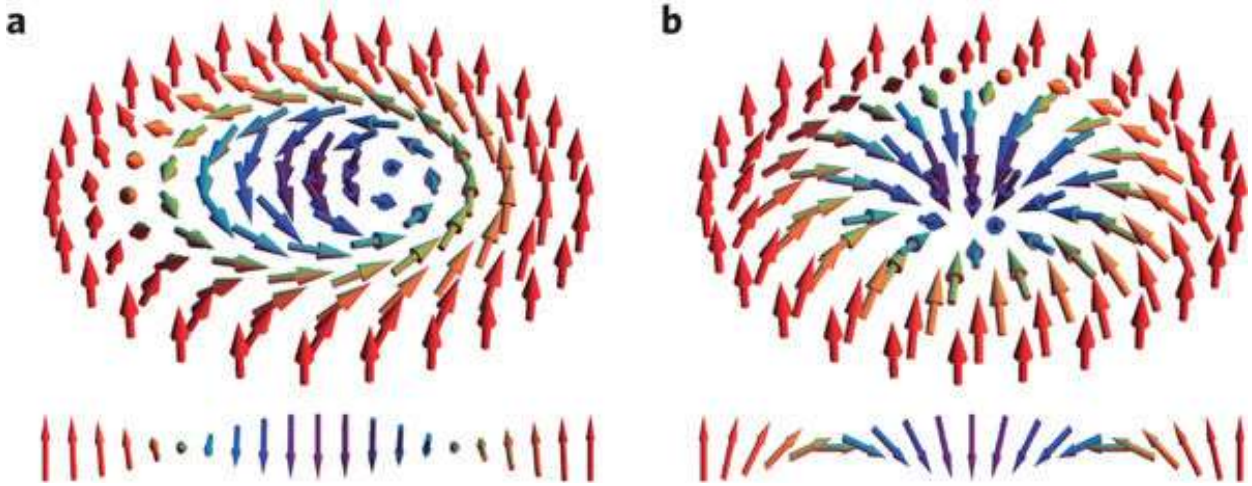

Figure 42: Two types of skyrmion. Bloch type skyrmions (a) typically exist in non-centrosymmetric bulk layers. Néel type skyrmions (b) typically exist in layers with interfacial DMI and thin films. Figure from Kézsmárki et al *[53]*.

Skyrmions exist as a structure with a topological charge – an up domain in the center in a down domain field. The domain wall in a skyrmion is an inherent winding that protects the core from reversal. This winding is characterized by a topological skyrmion number, as defined by Nagaosa and Tokura as: [38]

$$N_{skyrmion} = \frac{1}{4\pi}\iint d^2\boldsymbol{r}\boldsymbol{n}\cdot\left(\frac{d\boldsymbol{n}}{dx}\times\frac{d\boldsymbol{n}}{dy}\right)$$

This equation counts the number of times that the angle of the skyrmion wraps around a unit sphere. When evaluated across the entire space of the skyrmion, there are several available solutions that exist for the voricity of the skyrmions and their phase. If the first equation is put into polar coordinates and solved across the radius, this vorticity of a skyrmion can be defined as a function of φ as:

$$m = \left[\Phi_{(\varphi)}\right]_{\varphi=0}^{\varphi=2\pi}/2\pi$$

Here the m is an integer that describes the orientation of the skyrmion winding. Skyrmions can be of vorticity ± 1, but with an additional term in the equation that describes the helicity of their phase as:

$$\Phi_{(\varphi)} = m\varphi + \gamma$$

This phase γ may be 0, $\pm\frac{\pi}{2}$ or π. The combination of these terms will describe both the shape of the skyrmion (from the nose-to-tail of the Bloch skyrmion as seen in (a) of Figure 42, to the sea anemone texture of the Néel type skyrmion in (b) of the same figure. The Bloch skyrmion as pictured above would have a winding of m=1 and γ=$\pi/2$, while the Néel skyrmion would be identified as m=1 and γ= π.

This math describing their orientation also has important implications for the current driven behavior of the skyrmions. Because of the coupling of the conduction electrons of a metal to the magnetic state of the system, a skyrmion creates a total magnetic flux that is $2\pi N_{skyrmion}$. Thus, they are very susceptible to a spin transfer torque which is driven by the movement of the conduction electrons through the material. This also gives rise to two interesting current driven effects: the Topological Hall effect and the Skyrmion Hall effect. For the topological Hall effect, as current flows through the skyrmion texture, it will be deflected by the Lorentz force due to the emergent effective field of the magnetic winding of the skyrmion. The topological Hall effect will add to the more common anomalous and ordinary Hall effects. For the Skyrmion Hall effect, the action of the spin transfer torque will deflect the skyrmion itself in an analogous motion to the ordinary Hall effect action on conduction electrons [38] [54]. The Thiele equation that describes this interaction is :

$$\vec{G} \times \vec{v} - \alpha\vec{D} \cdot \vec{v} + 4\pi\vec{B} \cdot \vec{J}_{hm} = 0$$

where the $\vec{G} \times \vec{v}$ term is the Magnus force – related to the topological charge of the skyrmion, with $\alpha\vec{D} \cdot \vec{v}$ as the damping term and $4\pi\vec{B} \cdot \vec{J}_{hm}$ as the drive term related to the current in the heavy metal layer. The effect of this equation is to describe the motion of the skyrmion that is both collinear with the current (due to drive) and at cross angles to the current flow (due to the skyrmion Hall effect and Magnus force).

As of this writing, two major types of skyrmions have been found. Bloch type skyrmions are named for the orientation of the winding of their domain walls and exist in non-centrosymmetric crystals like MnSi arising from bulk DMI and typically are of very small diameters (on the order of 20-200 nanometers) [38] [55] [56] [57] at temperatures below room temperature. Néel type skyrmions exist as a result of a broken-symmetry interface between two material layers (due to interfacial DMI), and may exist at room temperature but are typically larger on the order of several hundred nanometers to several micrometers. [58] [59] [60]

A key parameter of the formation of skyrmions is the strength of DMI. DMI exists in materials with high spin orbit coupling and a lack of inversion symmetry. The first materials displaying skyrmions have been bulk non centrosymmetric materials in a wide variety of materials [61] [62] [63] [64] [65] [66] [67] [68] [69]. Proposed by A. Fert, a mechanism called the 3-site interaction has been demonstrated to result in the existence of DMI in thin films at the interface with a magnetic material and a material with a high spin orbit coupling [70]. This interfacial DMI potentially allows the existence of skyrmions in thin films. Two decades after this theoretical prediction, observations of thin film skyrmions were made but at low temperature [6] [71]. However, this low temperature requirement is prohibitive for industrial scale applications. Room temperature skyrmions [72] [73] obtained in thin film materials have improved that outlook. The current-induced motion of skyrmions has also been a significant topic of interest for low

temperature skyrmions and has developed at a significant pace since the discovery of the room temperature skyrmions. Some of the modern challenges currently being addressed are the creation, manipulation and detection of these skyrmions [74] [75] [76], the reduction of their size to 10 nm or below, and the reduction of the damping constant of the material systems. [40]

There are increasing research efforts to develop thin-film hetero-structured materials that form skyrmions at room temperature and are controllable with electrical currents. The observation of a sizeable interfacial DMI resulting from interfacing thin ferromagnetic films with a non-magnetic layer that possesses high spin-orbit coupling (*e.g.* 5-*d* transition metals such as Ta, W, Pt, Ir, *etc*.) [77] [78] [60] [79] provides a pathway to engineer material properties to form skyrmions in thin films. Trilayer ferromagnetic heterostructures exploiting interfacial DMI and asymmetric interfaces are particularly attractive materials systems. The principle is to sandwich a magnetic layer between two different layers of high spin-orbit coupling material. This heterostructure is constructed such that that the DMI contributions due to the top and the bottom interface will add to enhance the value of the DMI. Examples of reported materials systems where skyrmions are observed in these multilayers at room temperature include Ta/CoFeB/TaOx [80], Ta/CoFeB/MgO [81] [82], Pt/Co/Ta [82], and Pt/Co/Ir multilayers [83].

This research focuses on the typical type of layer stack used to generate the Néel skyrmions – a multilayer system that uses different top and bottom interfaces across a ferromagnetic layer to break inversion symmetry. A typical set of materials include materials with a strong spin-orbit coupling Pt, Ir, W, Ta along with strong ferromagnetic materials Fe, Co. [79] The simplest form of layer stack uses the differential growth of one specie on the surface of the other – for example, a Pt/Co/Pt stack would have a slightly different bottom Pt/Co interface from the second top Co/Pt

interface. Tuning of this interfacial geometry and growth parameters offers a way to induce the antisymmetric exchange necessary to eventually generate skyrmions.

The interfacial DMI that will be used for these systems comes from the strong interaction of the spin orbit coupling across the layer to layer interface. The strongly ferromagnetic Co atoms link through the high spin-orbit coupling of the Pt layer. This creates the next-to-nearest-neighbor interaction discussed briefly in Chapter 0. This $(\vec{S}_1 \times \vec{S}_2)$ orientation of the cobalt spins is generated by the induced orbital moment generated from both the cobalt moment and the moment that is induced in the Pt layer by the cobalt atoms [6] [84]. The effective induced magnetization in the Pt layer helps to drive the canting of the Co moments. The top and bottom layers will each have their own contribution to the systems, and by summing the interfaces, the net DMI can be either enhanced or reduced [79] [85]. Contributions from the top and bottom interfaces sum, but will have opposite directions for the same sign (resulting in a net zero DMI for the system if the two interfaces are identical). In practice, the two interfaces will be different due to the growth direction of the materials, but a stronger net DMI can be found by replacing one of the interfaces with a different type of system.

What the trilayer stack discussed above possesses in simplicity, it lacks in versatility. Therefore, it is common to incorporate a thin layer of another heavy metal at one of the heavy metal/ferromagnetic interfaces. As this additional layer can have a severe impact on spin-orbit coupling across the interface, DMI may strengthen, leading to the formation of skyrmions. [86] For these stacks, DMI improvement has been reported in stacks of the form HM/FM/X/HM where HM is the heavy metal, FM is the ferromagnetic layer, and X is the symmetry breaking interlayer. [87] As of late, Pt/Co/X/Pt stack structures have garnered significant attention in attempts to strengthen DMI, given that the Pt/Co interfacial DMI is well-understood. [82] [88] The research

discussed in this chapter not only confirms the presence of DMI in this stack type, but also that a unique skyrmion regime occurs Pt/Co/Os/Pt layers at the spin reorientation transition of the Co film due to the DMI.

Chapter 4, Section 1:
Probing DMI via Asymmetric Domain Wall Growth

One method proposed for determining the presence or absence of interfacial DMI in a thin film material is to check the symmetry of the domain walls. Bubble domains are previously known types of structures that while they display some regularity in size and shape, are not chirality driven. Thus, it is important to be able to differentiate from achiral fixed size bubble domains, and the DMI driven skyrmions. To do so, a symmetry breaking perturbation is first applied, and then the propagation dynamics of the wall are observed – a susceptibility to this technique indicates presence of a chiral wall. [89] [90] [91]

The rationale for using asymmetric domain growth to determine whether chirality is present in magnetic textures is as follows. A non-chiral domain wall, when subjected to an out-of-plane magnetic field will expand without a preferential directionality. For a nucleation site in a film without directional anisotropy, and with no or few pinning sites, applying an out of plane magnetic field will result in isotropic circular domain expansion. This isotropic expansion can be linked to the fact that at all points along the domain wall, the system is energetically equivalent. For a chiral domain wall in the absence of an applied field, the system is likewise energetically equivalent across its length. However, if a symmetry breaking field is applied (as presented for a pair of Néel walls in Figure 43 below), the domain walls that are canted will have an in-plane component to their magnetization, which in concert with the applied field, can alter the energetics of the chiral domain wall depending on their orientation. Local magnetizations oriented in the direction of the symmetry breaking field will have a lower energy than those oriented antiparallel

to the symmetry-breaking field. Consequentially, upon application of a non-symmetry breaking out-of-plane field, those regions of the domain wall with magnetization parallel to the symmetry breaking field will expand faster than those oriented in opposition. For a circular domain wall created from a nucleation site, this will instead result in an elliptical expansion of the domain wall. [92]

To illustrate these energy considerations, we may consider a Néel wall existing within a symmetry breaking field oriented along the X axis, and a pulsed field along the Z axis. Due to the Néel character of the domain wall, it is expected that an asymmetry in the propagation rate would develop for right versus left (depending on the chirality of the domain wall), while the top and bottom walls (propagating mainly along the Y axis) would propagate at an equal rate. For a Bloch wall, the twisted nature of the domain wall would lead to asymmetry in Y-direction growth, while the X axis propagation would be symmetric. [90] Experimental results regarding the effect of broken symmetry in Néel-type structures will be discussed later in this chapter.

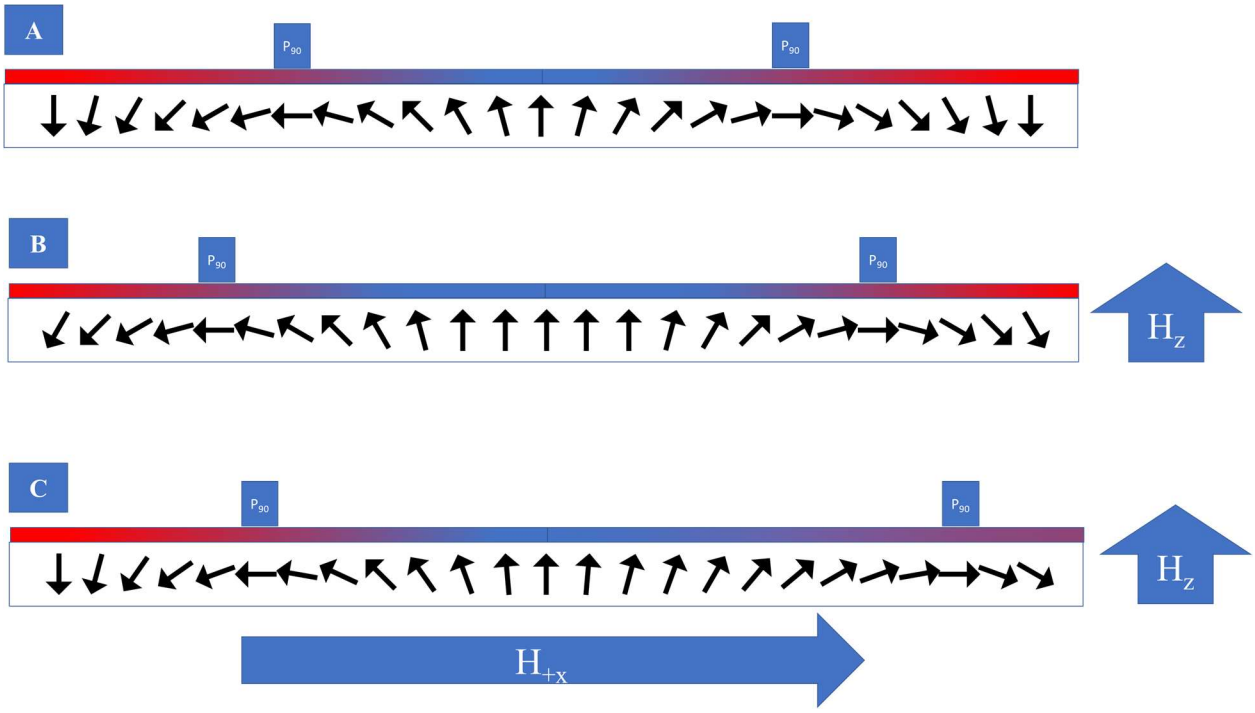

Figure 43: Symmetry breaking of a Néel wall. Spins in a down-up-down pair of domain walls are represented by a set of black arrows. The position at which the wall is in-plane is marked by the P_{90} mark. Sub figure A shows the initial state of the system with no applied field. In sub-figure B, an out-of-plane magnetic field has been applied, expanding the center up domain and moving the domain walls equally. In sub-figure C, a symmetry breaking field has been applied in the +X direction. The spins that are aligned in the direction of the symmetry breaking field will have an enhanced propagation, while the spins antiparallel to the symmetry breaking field will be retarded.

This symmetry breaking by in-plane field can be done in the Kerr microscope with a vector field setup. In this case, it is necessary to modify the system, as seen in Special Section 1. The addition of an independently driven pulsed field coil in the out of plane Z direction allows the system to have a constant in-plane field for symmetry breaking, along with a pulsed out-of-plane field for propagation. By tracking the different domain wall propagation velocities, it is possible to compare both the broken symmetry walls and the unbroken symmetry walls. While this technique is not suitable for determining the magnitude of the DMI field (although the suitability would increase if the wall was driven at higher velocities into the flow regime), it is still an excellent method for finding the relative strength of the symmetry breaking field that serves as a qualitative evaluation of the presence of DMI.

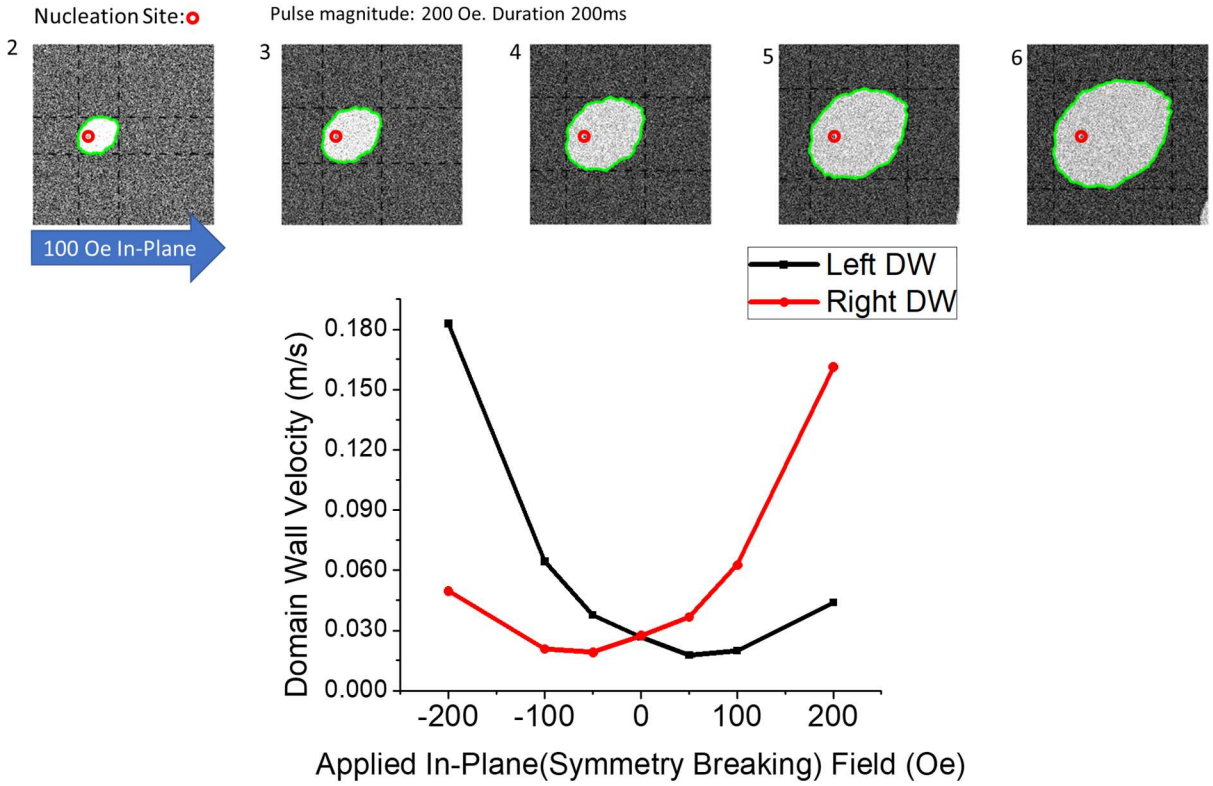

Figure 44: Symmetry-broken domain wall propagation in Pt/Co/Ir/Pt. An in-plane 100 Oe field was applied in the +x direction to break the symmetry, and a 200 Oe field was pulsed for 200ms in between each snapshot. The left and right domain wall position from the top images is tracked and plotted for different values of the in-plane field, and fit to find the domain wall velocity. Velocity figures for the left and right domain wall are plotted as a function of in-plane field.

In Figure 44, prospective outlines of the domain walls are shown for an increasing number of out-of-plane field pulses. With the in-plane field along the X direction and the pulse in the Z direction, it is apparent that the field will act to affect the left-hand and right-hand domain walls in a different way than the top and bottom domain walls. While the top and bottom domain walls are affected equally by the symmetry breaking field, the left and right domain walls both have a component that is modified by the in-plane field. As in the above image, if an out of plane +Z direction field is applied simultaneously to the + X direction in-plane field, the rightmost domain wall will have an enhanced propagation velocity, while the leftmost domain wall will have a

retarded propagation velocity. Of note, that due to the limited low-end field duration, that these domain walls are moving within the creep regime for their velocities.

Short pulsed fields allow the domain wall to be propagated in multiple steps. By comparing the symmetry-broken domain walls to the unbroken domain walls, a factor of asymmetry can be calculated. Fitting across many small pulses give significant confidence to the value of this asymmetry. By applying different in-plane fields, the asymmetry can adjusted by modifying the strength of the domain wall canting.

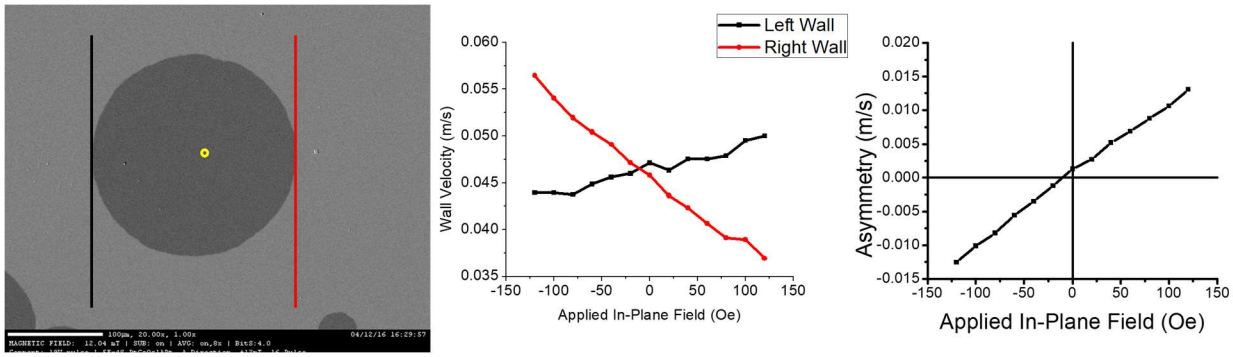

Figure 45: Finding asymmetry in one direction for Pt/Co/Os0.1nm/Pt. Left shows the tracking of left and right domain walls versus the nucleation site as a function of pulse. This is used to find a domain wall velocity (center) that is plotted versus the applied in-plane field. Note that the left and right wall propagation are not symmetric about field – suggesting a tilt in the axis of the sample.

Other studies have used a tilted coil setup to evaluate asymmetric domain wall propagation. [93] [94] However in this case, it was significant to have an independent set of in-plane and out-of-plane components. Pulsing only the out-of-plane component while the in-plane component is kept constant offers more control over the timing of the pulses. This also provides a method to correct for aberrant tilt of the sample or coilsets. For a single coil, the in-plane component and the out-of-plane component are inextricably linked. In the example shown below, a field along the +X axis will also produce a +Z field and the Z field will be related to the X-axis field by a sine relation.

Adjusting the pitch of the coil will allow adjustment of the Z field, but will also change the X axis field field.

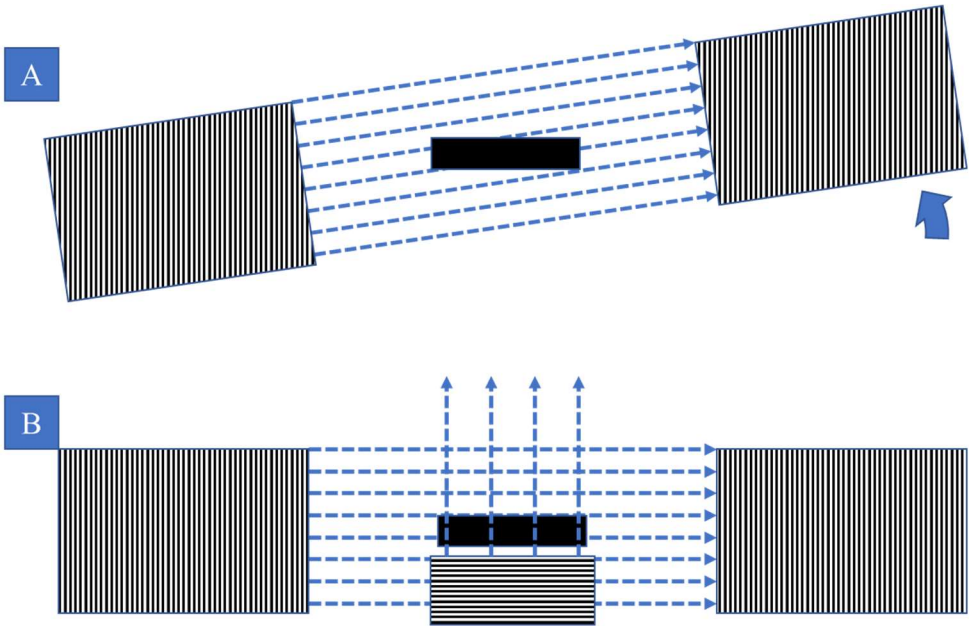

Figure 46: Coilset systems for symmetry breaking measurement. Tilted (A) versus separate (B) coilset systems to be used in the Kerr microscope. Of note that in A, any tilt in the sample will be present in at the same magnitude in both orientations. In addition, the magnitude of field in A is linked for both in and out of plane directions. For B however, any tilt in the sample can be corrected by examining all 4 field pairings. In addition, a wider range of in-plane and out-of-plane field magnitudes and durations is available.

As shown above in Figure 46, adding an independent out-of-plane pulse coil allows the Z field to be controlled separately from the in-plane field. This allows for a wide range of pulse durations from 1 second to 10^{-5} seconds with the lower bounds determined by the pulse coil inductance. Additionally, a range of field amplitudes is available to a maximum around 200 Oe with smaller fields at short timescales due to the coil rise time. Independent control of the magnetic field in the X and Z direction makes the system suitable for studying films with a wide variety of anisotropies possible, allowing the domain wall propagation to be more precisely controlled for better fitting.

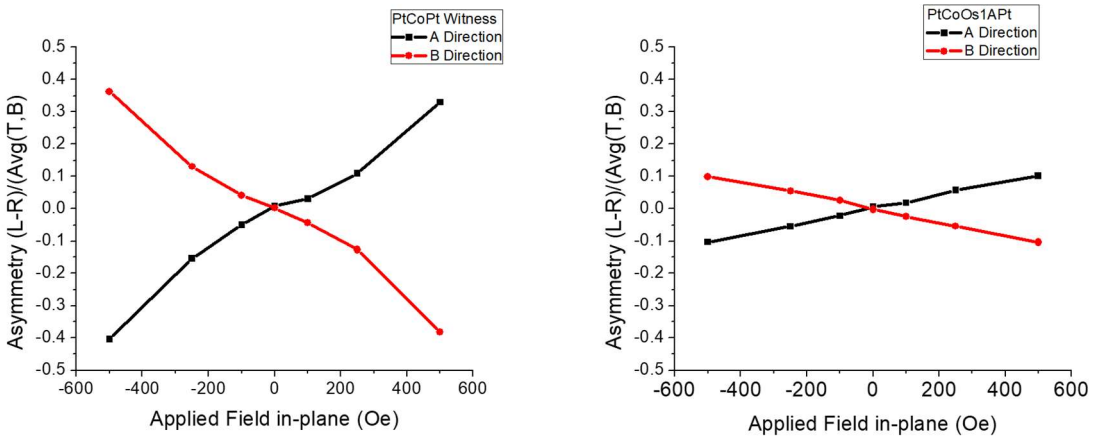

Figure 47: Asymmetry in all 4 field pairings for Pt/Co/Pt and Pt/Co/Os0.1nm/Pt. This result plots the normalized asymmetry ((Left wall propagation – Right wall propagation)/(average of unbroken top and bottom wall)) versus applied in-plane field. The pulsed out of plane field magnitude is kept constant, but the lower coercive field of the Osmium containing film results in greater DW propagation.

By examining all 4 field pairings – in both in-plane directions and both out-of-plane directions – it is possible to correct for any tilt or aberration in the field coil alignments without adjusting the hardware position. Any coil misalignment would manifest as an offset in the zero position of the asymmetry, apparent where the two curves cross.

Using this symmetry breaking asymmetric domain wall growth comparison technique, multiple samples of the four-layer stack type were evaluated. The overall format of the samples was Ta(5nm)/Pt(3nm)/Co(1.1nm)/X(var)/Pt(3nm)/Ta(5nm). The top and bottom Ta layers were used as capping and seed layers, respectively, and do not contribute significantly to the magnetic characteristic of the sample. From this point, the Tantalum layers will not be mentioned in the sample configuration, but they can be assumed to be present. The Pt/Co/Pt stack with no X interlayer provides a high moment around 1400 emu/cc with a coercivity around 160 Oe. Adding in the X interlayer at the top interface modifies the top interface and will change the properties of the system. The presence of DMI has been established in a wide variety of these types of films. For certain heavy metal materials inserted as the X interlayer, there is some modification of the

interface creating either a positive or negative DMI. Materials evaluated in this way were Iridium (Ir), Platinum of a different growth pressure (Pt), and Osmium (Os) with the special properties of Osmium receiving special attention [60]. While some structures were grown with the interlayer added at the bottom interface, this produced lower modification of properties than at the top interface.

Without access to certain high frequency techniques, Brillouin light scattering [60], or high resolution techniques such as MFM, it is difficult to make a precise measurement of the DMI strength. However, the observation of induced antisymmetric growth in the films as studied complements the later observation of interfacial driven chiral bubble structures. The velocity-corrected asymmetry in the Pt/Co/Pt structures is stronger than that in the Pt/Co/Os0.1nm/Pt structure by approximately 60%, however this does not necessarily indicate strength of DMI interaction.

In order to use this technique, the system must have a well-behaved out-of-plane anisotropy with square hysteresis loops, or an H_c sufficiently above the stray out-of-plane field from the in-plane coils. If the system has a small enough coercivity, the in-plane coil may create sufficient stray field to switch the sample. This technique also relies upon the domain wall expansion being well-ordered and occurring from a defined nucleation site. When this antisymmetric expansion experiment was applied to the Pt/Co/Os/Pt samples with higher Os thickness, there was a significant discovery. While the film with the structure Pt/Co/Os(0.1nm)/Pt exhibited antisymmetric growth as a hallmark of DMI, attempting the same experiment with an Osmium thickness of 0.2nm produced a significantly different result.

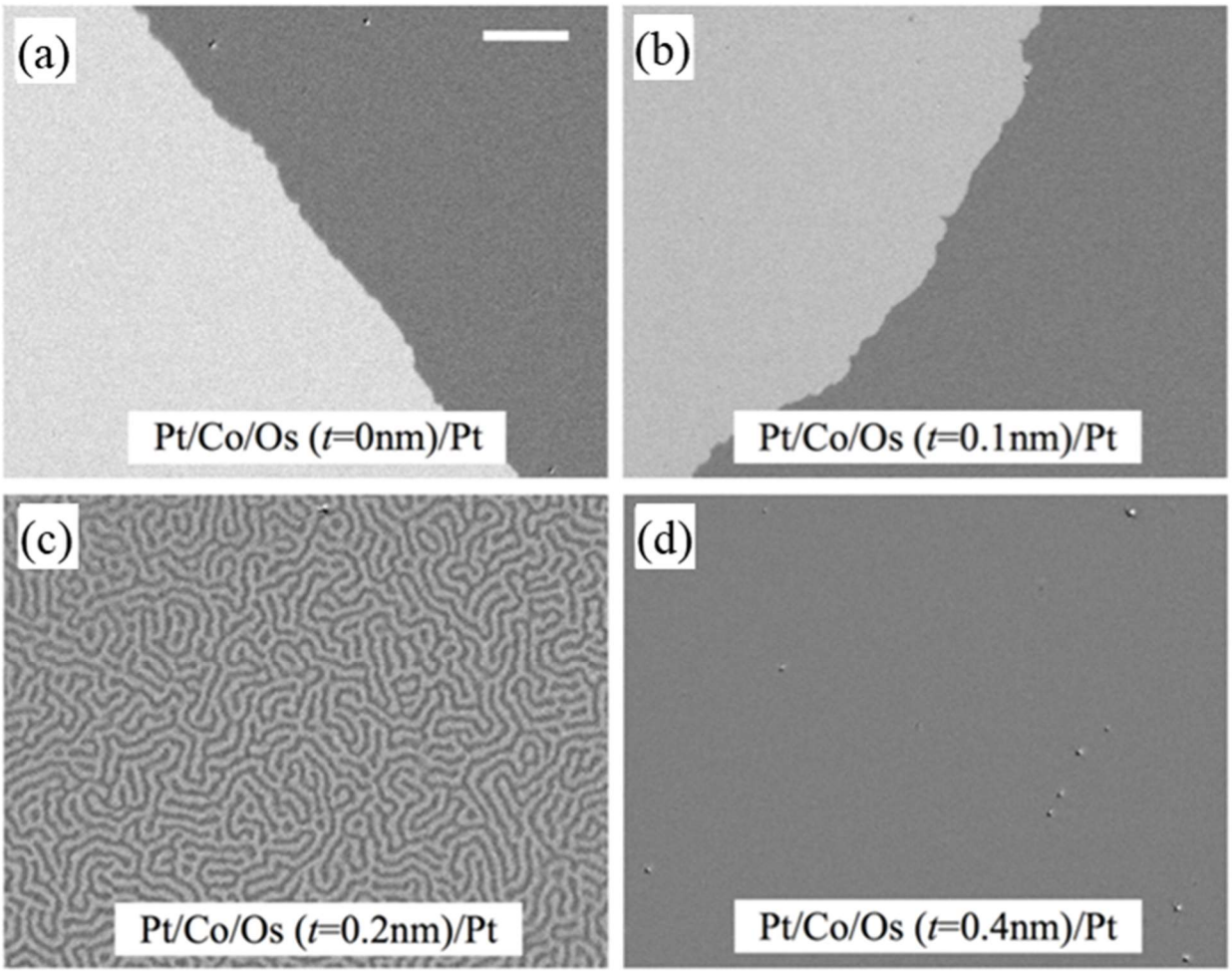

Figure 48: Domain walls at room temperature for Pt/Co/Os/Pt films. Domains were stabilized at zero field in the middle of reversal to illustrate domain shape and behavior. Samples: (a): Pt/Co/Pt (b): Pt/Co/Os0.1nm/Pt (b): Pt/Co/Os0.2nm/Pt (d): Pt/Co/Os0.4nm/Pt. The 0.1 nm Os samples express similar large domain walls to the Pt/Co/Pt system. The stripe phase in (c) is thermally active and fluctuates, while the uniform contrast in (d) is indicative of a uniform (in-plane) magnetization. The scale bar shown in (a) corresponds to 25 micrometers..

The Pt/Co/Os(0.2nm)/Pt film at zero applied external field shows a labyrinth of stripe domains with a period of 3 micrometers. These stripe domains are highly thermally active, fluctuating locally over the course of seconds. The film is magnetically soft, requiring only 2 Oersted of applied field to saturate in the out-of-plane direction. If saturated and returned to 0 applied field, the system immediately relax back to the stripe domain phase again. Compared to the film with a 0.1nm Os thickness at the top layer, the film with 0.2nm of Os has a 70% lower

saturation moment and a 95% lower coercivity. For an Os thickness of 0.4nm, the film no longer has a perpendicular magnetic anisotropy.

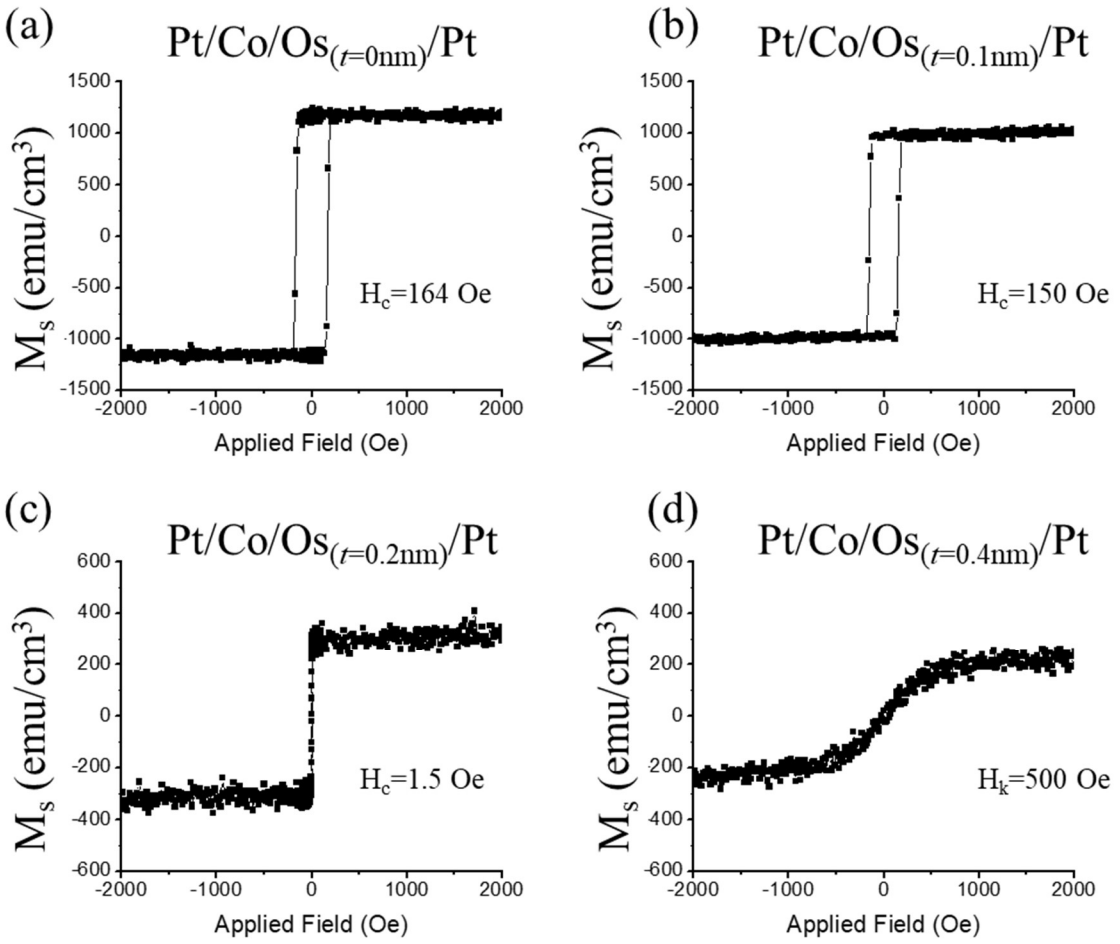

Figure 49: VSM magnetometry loops for various Pt/Co/Os/Pt films. (a): Pt/Co/Pt (b): Pt/Co/Os0.1nm/Pt (b): Pt/Co/Os0.2nm/Pt (d): Pt/Co/Os0.4nm/Pt. All measurements were done at room temperature. Note the shift in axis from (a) and (b) to (c) and (d).

VSM based hysteresis loops shown above in Figure 49 indicate the dramatic shift in the loop shape with increasing Osmium thickness. At 0.2nm of Osmium as the top interlayer, the large square loop shape gives way to a much smaller loop, and then in-plane. This is consistent in VSM measurements of samples as well, but even more important is the significant reduction of moment as the Osmium thickness is increased.

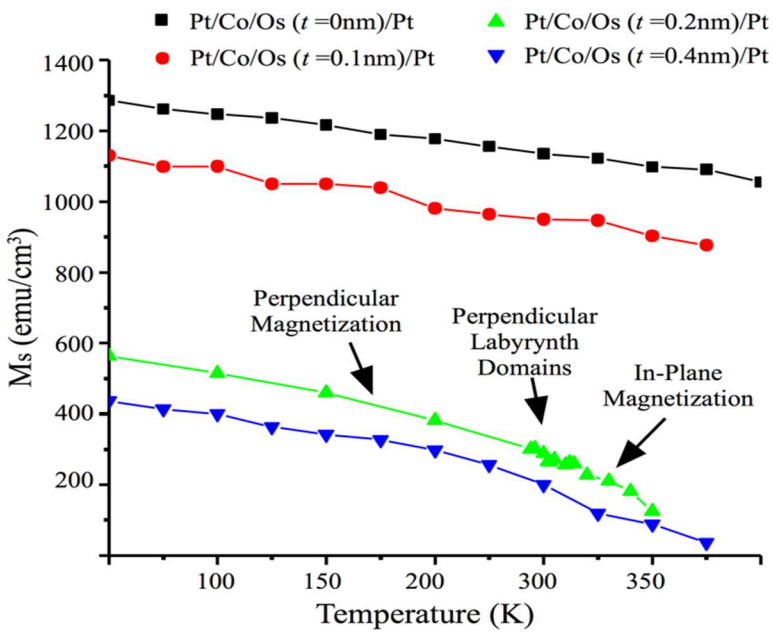

Figure 50: OOP VSM magnetometry data showing saturation moment for Pt/Co/Os/Pt films. This illustrates the difference between low Os thicknesses (0 and 0.1nm), and higher Os thicknesses (02.nm and 0.4nm). Note that the volume moment has decreased significantly, and the shape of the higher Os thicknesses indicates they are approaching the Curie temp around room temperature.

VSM measurements of the net moment of the sample in Figure 49 and Figure 50 show a significant shift between the low/no Osmium samples and the higher thickness samples. This confirms the in-plane nature of the 0.4 nanometer sample, and shows that the 0.2 nanometer sample is nearing an in-plane transition. By performing VSM measurements along a wide range of temperatures, the temperature evolution of each sample's magnetic behavior can be compared. As can be seen from the above chart, the sample with no Os layer and 0.1 nm sample perform in a very similar manner versus temperature. The sample with an Os thickness of 0.1 nm has a slightly lower moment by (~15%) than the sample without Os across the range of temperatures studied. As Os thickness increases, the saturation moment becomes more depressed, and a sharp change in magnetization corresponding to the Curie point begins to develop. While the Curie temperature was above the direct measurement range for samples with a thinner/no Os layer, the transition to in-plane anisotropy for the 0.2 nm and 0.4 nm films occurs between 225 and 250 K and 300 and

310 K, respectively. While the Curie temperature is independent of the spin-reorientation transition, the reduction of the magnetism of the sample is partially thermally driven.

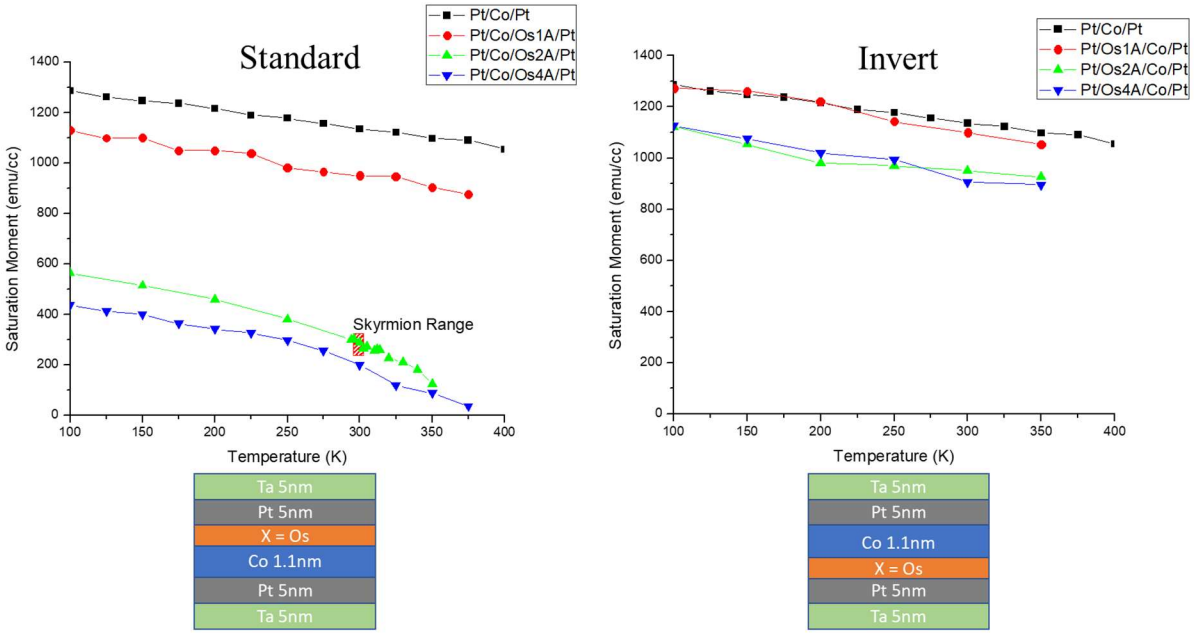

Figure 51: VSM saturation moment versus temperature for standard and invert layers. Standard Pt/Co/Os/Pt films (left) versus inverted Pt/Os/Co/Pt films (right) The data shows less reduction of moment for Os at bottom interface. Pt/Co/Pt (no Os) is shown in both datasets for comparison. Skyrmions are only present in an observable form in the marked region in the Standard geometry.

Another critical factor to mention is that the top interface seems to control this property of the system. The above figure includes samples with an inverted layer stack of Pt/Os/Co/Pt. As can be seen, for these invert layers, there is a small modification of the moment and coercive field, but that the overall modification of the multilayer properties is very small. Thus, while some additional measurements were done on the inverted sample layers, much more attention was paid to the samples with novel behavior.

Chapter 4, Section 2:
Novel Behavior of Pt/Co/Os2A/Pt

With the interesting nature of the Os 0.2nm sample, further analysis was required. With a small applied out-of-plane field, the stripes collapse to small circular textures of approximately 2.3 micrometers in diameter.

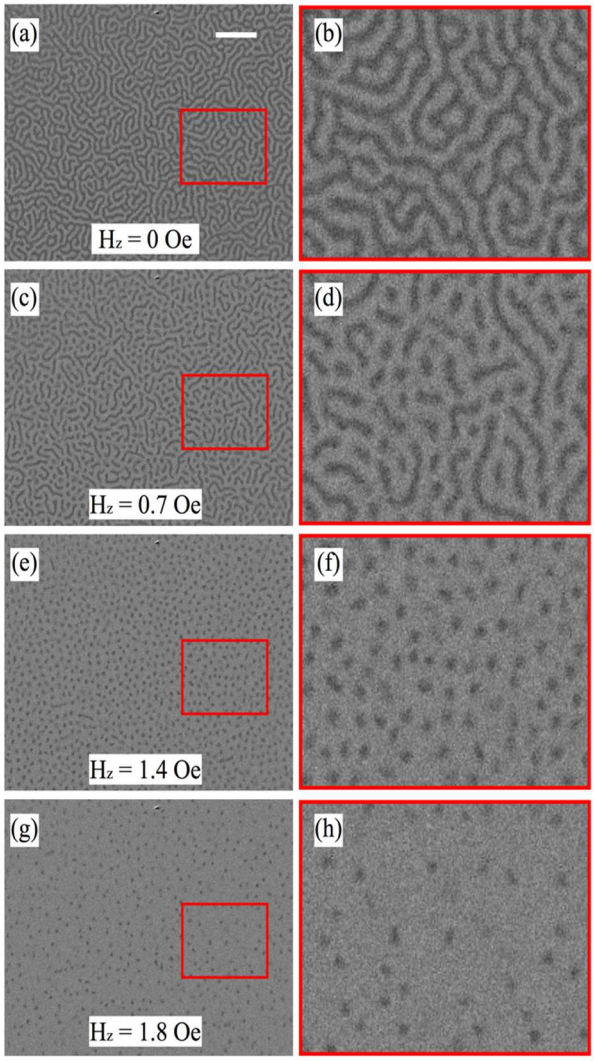

Figure 52: Field-induced stripe collapse to skyrmions in Os=0.2nm films. (a) and (b) show the zero field phase, where (b) is an inset of (a) in the marked region. (c)-(d), (e)-(f) and (g)-(h) are other similar pairs at higher fields. The scale bar for all images is the same, indicated by the 25µm scale bar in (a). The insets (b), (d), (f) and (h) have a field of view of 50µm wide.

Above, Figure 52 details the behavior of the system as stripes collapse into the circular textures as a function of an out-of-plane magnetic field. [95] This collapse occurs in real time, with the domain wall velocity of the collapse proportional to the applied field strength. Of significant interest is the behavior of the small circular textures left by the stripe collapse. While little field is required to collapse the stripes, the cylindrical textures remaining relatively much more stable. The images shown below in Figure 53 demonstrate the different phases, from a completely saturated film, through an empty-field nucleation of cylindrical textures from the uniform film, through the expansion of those textures into stripes, the domination of a complete stripe phase at zero field, and then the collapse of the stripes as the field is increased.

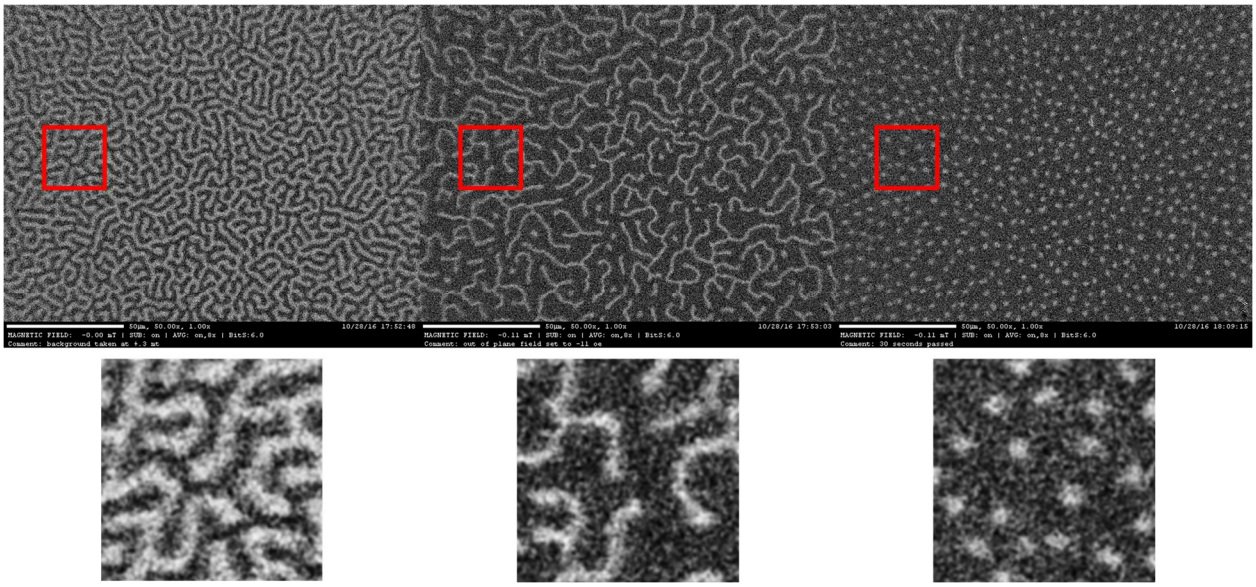

Figure 53: Collapse of stripe phase to close-packed skyrmion lattice at room temperature. Field is increased from zero (left) to 1.1 Oe (center) and the image was taken immediately. Image at right shows same system as in center, but after 30 seconds of elapsed time. This shows how the stripe phase under applied field rapidly collapses to skyrmions, and additional skyrmions will populate the film. Insets (below) from same region have a 25 μm field of view. Examples of stripe and skyrmion phase are shown in Supp. Video 2 and 3.

While these cylindrical textures exhibit certain features characteristic of skyrmions, the existence of resilient circular magnetic domains in a film type that exhibits the DMI-characteristic antisymmetric domain wall expansion does not confirm that they are skyrmions. A skyrmion by

definition must have a chiral domain wall and an integer topological charge– properties which in turn are made evident by novel electronic transport properties. Measurements discussed later in this dissertation will show that these cylindrical textures do indeed exhibit a deflection under applied current due to their inherent chirality (the as previously mentioned skyrmion Hall effect), and thus can be confirmed to be skyrmions. While there is still some debate about the precise taxonomy of regular cylindrical textures with an interfacial DMI driven Néel domain wall that exhibits a resistance to defect pinning and applied field, it is currently accepted that the definition of "skyrmion" covers these textures.

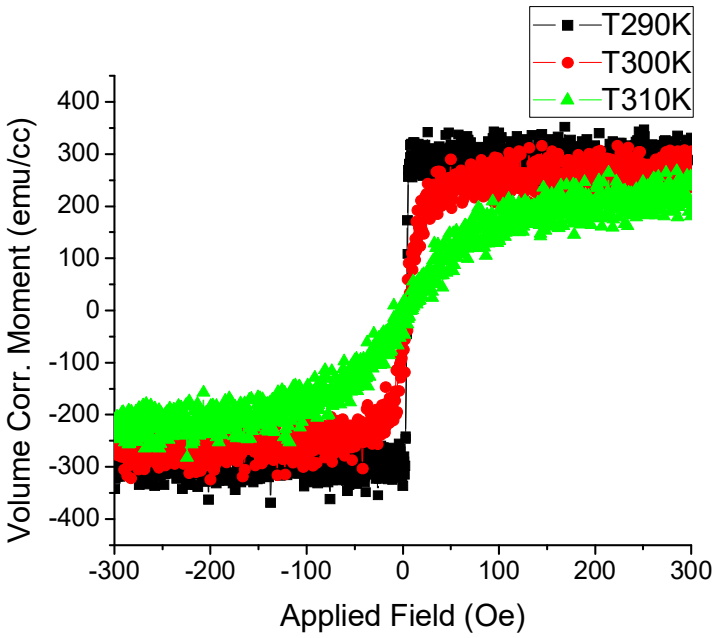

Figure 54: Out of plane VSM loops for Pt/Co/Os0.2nm/Pt around the skyrmion transition. The system transitions from a square loop at 290K, to a slight tilt at 300K, and loses significant (almost 30%) saturation moment by 310K.

As shown in the VSM loops above in Figure 54, for the Os 0.2nm samples (hence referred to as "Skyrmion samples" exhibit a strong dependence on temperature in a range around room temperature. This dependence is strongly related to the Osmium thickness, with differences even across samples deposited at the same time. With the net moment of the sample so strongly related

to temperature as shown in the expansion of Figures 51 and 54, observation of the local domain morphology across the range of temperatures was necessary.

To observe the temperature dependence of the local domain morphology, a heating stage was employed in the Kerr microscope. Since the response of the samples to temperature is so strong, it is possible to observe the transition from bulk domain formation through a skyrmionic phase and finally to a temperature where the sample is magnetically in-plane over the course of 20 Kelvin. Due to the low requirements for this heating, it can be done in open air which allows for transport measurements to be done across this range. For some samples exhibiting the skyrmion phase exactly at room temperature, accessing the large domain phase requires cooling, which can be accomplished by an ice bath in the coolant interchanger. This can lower the temperature of the system to below 18 degrees C, but may lead to condensation issues on the sampele if the temperature is reduced below the atmospheric dew point.

Observing the stripe to skyrmion phase transition in the Kerr microscope provides a real-time, real-space representation of the inherent dynamics. As temperature increases, the domain morphology transitions between large bulk domain walls that propagate in a smooth fashion across the sample, toward large blotchy textures that begin to thermally activate, and finally to a stripe phase that can be collapsed to skyrmions. At temperatures higher than the skyrmion/stripe temperature regime, there is a very brief transient phase that generates “hot” skyrmions that are unstable and too highly driven to be properly observable with the Kerr microscope. For temperatures above this narrow 2K wide phase, the magnetization of the sample becomes in-plane. This transition from PMA to in-plane orientation is matched by the transition of the Kerr hysteresis loop from a square loop with critical field of 1 Oe to a canted loop with a nucleation field at 0.5

Oe. The below figure details this phase transition, as well as the skyrmionic zone for each set of temperatures.

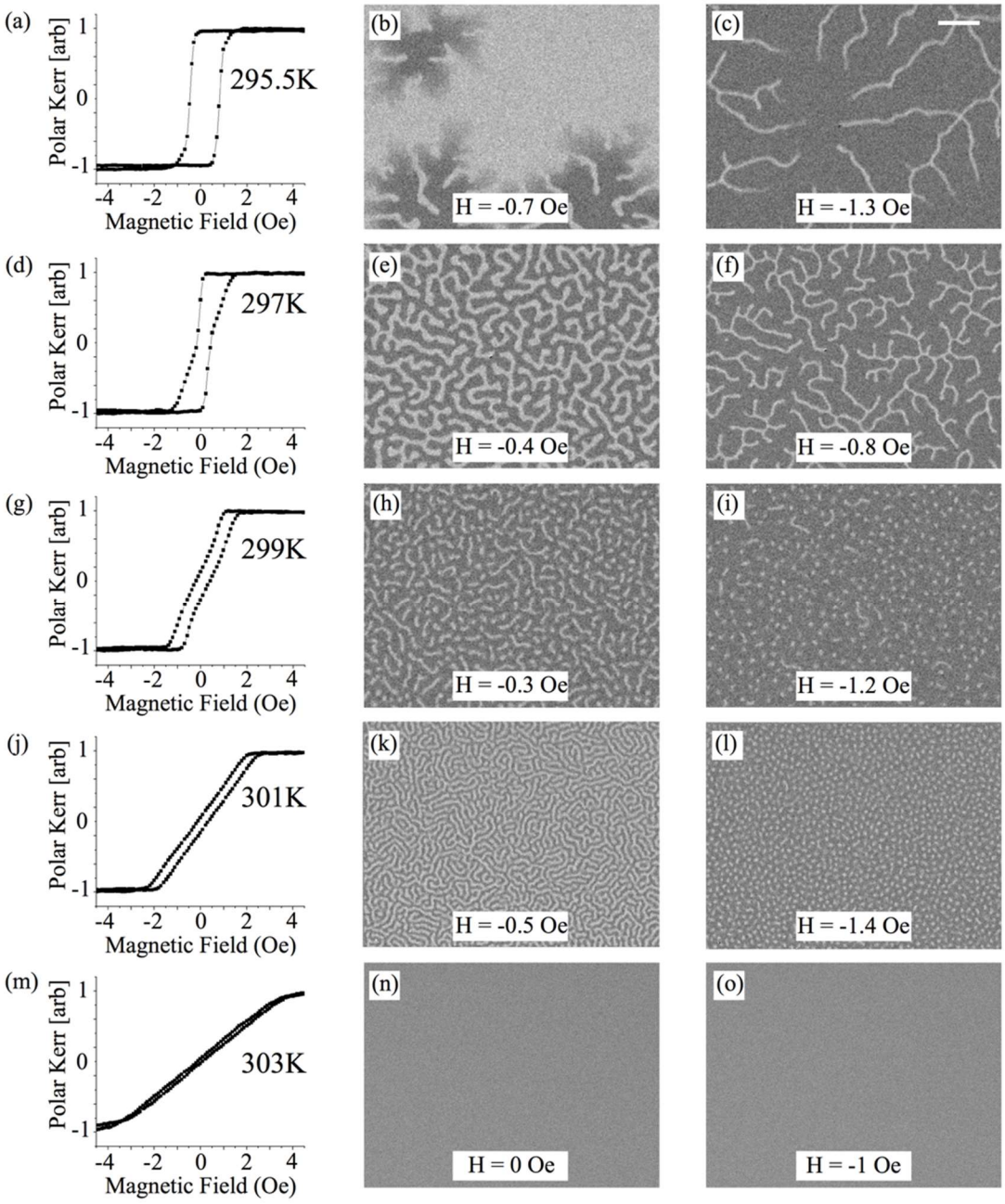

Figure 55: Magnetization and domain behavior of Pt/Co/Os0.2nm/Pt. Kerr magnetization loops (a, d, g, j, m) and domain morphology images at low (b, e, h, k, n) and high (c, f, i, l, o) fields versus temperature (as marked on the loop). This shows the transition from large domain walls just below room temp (a-f), through the skyrmion phase (g-j), and into the in-plane state (m-o).

The phase transition from PMA to in-plane anisotropy corresponds to a spin reorientation transition (SRT) [96] – which occurs at a temperature where the perpendicular magnetic anisotropy and the shape anisotropy are balanced. In general, the magnetic anisotropy will have a stronger temperature dependence than the magnetization in the film. This will lead to a transition from perpendicular effective anisotropy to in-plane anisotropy with increasing temperature through the SRT. Thus, as the effective out of plane magnetic anisotropy drops toward zero, the relative strength of the DMI is sufficiently large to influence the domain walls into forming a chiral shape. These SRT DMI skyrmions are potentially interesting considering their limited phase space. With regards to temperature, it is possible to nucleate a skyrmion within its temperature window and then cool the system down to below the nominal skyrmion temperature. This can result in a large, circular texture expanding from the skyrmion that will retain some of the characteristics of skyrmions. However, these supercooled features will also be destroyed by application of current, and will not reform.

Some of the attractive features of skyrmions for data processing are their high mobility in response to applied electric currents, their particle-like interaction behavior, and their aversion to pinning sites. *Vis a vis* nucleation, several attractive techniques described in the literature thus far show skyrmion formation when a loose stripe phase is passed through a constricted wire with a non-homogeneous current [97] [49]. Other techniques show currents passed across a specially nucleated inhomogeneous region of film texture may generate skyrmions as well. [98]

To initially address the current-induced skyrmion motion, two large contacts were made to the film and some simple qualitative measurements were made about the motion of the skyrmions. With no current applied, skyrmions will move randomly in their lattice due to thermal excitation. This motion occurs in a series of hops, with a frequency determined by the system temperature,

and a hopping distance of around 2 to 3 micrometers (the nominal spacing of the skyrmion and stripe lattice) is observed. When a current is applied, there is still a high degree of random thermal hopping, but also a bias direction in the direction of the electron flow. For a disordered skyrmion state at low steady currents, the motion primarily consists of the individual skyrmions hopping at a semi-fixed distance and random frequency.

Chapter 4, Section 3:
Current Driven Motion of Skyrmions

The nature of the magnetic texture of the skyrmions also gives them interesting behavior and interactions when the same current is applied to a close packed lattice of skyrmions. Due ot the topological nature of the textures, it would be expected that and they do not annihilate each other, [98]. Additionally, while creep regime movement of the skyrmions occurs with a mixture of thermal hopping of individual textures, for sufficiently dense organizations, channels of motion become apparent in this order. These channels resemble the behavior seen in Type-II superconductors under heavy applied field – where a non-superconducting vortex will form to allow magnetic flux to penetrate. These vortices can then flow in the presence of an applied current. The flow behavior of the skyrmions in the close packed lattice mimics this kind of channel forming behavior, where a relatively small number of skyrmions are in motion at a time, and other portions of the lattice are stationary.

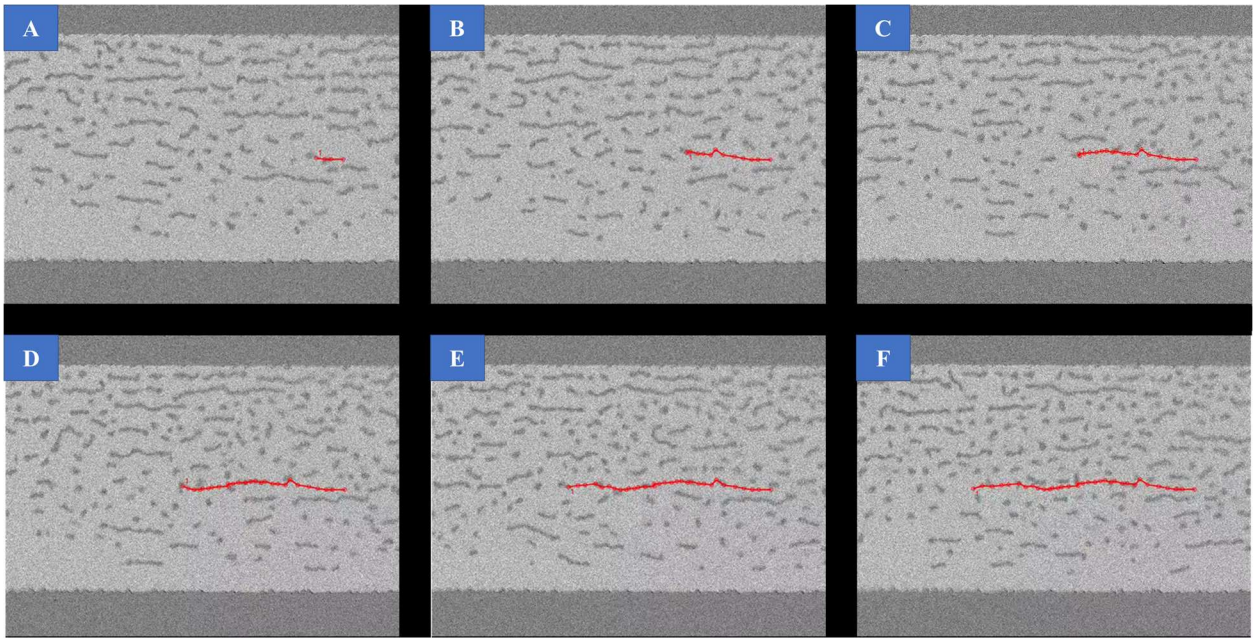

Figure 56: Tracking a skyrmion path. 3mA of current is applied along the wire from left to right. The skyrmion path is plotted by hand, showing the hopping nature of the motion, and the relative linearity of the path in the wire.

There are two general types of behavior for these skyrmions in the creep regime. At low current densities, the aforementioned flow channel effect will be present, where the lattice is largely stationary and only a few localized paths are in motion. However, at high enough current for the close packed lattice, the entire lattice will begin to shift in a cascading flow. This transition comes as the skyrmion lattice loosens somewhat allowing for the formation vacancies that can be filled by skyrmions in the upstream end of the lattice. This can be seen in the supplemental videos: Supp. Video 4, 5, 6.

As previously discussed, the field-nucleated skyrmions in this system exist within a relatively small field regime. The skyrmions can either be formed from a saturated film by lowering the field below the nucleation field, or from the stripe phase by raising the field until the stripes collapse to skyrmions. Previous research has shown that skyrmions can be generated from the stripe phase by driving the stripes through a narrow choke with current. In the Osmium

skyrmion system however, it is possible to perform a current based nucleation of skyrmions without incorporating additional geometry features. As observed in the following figures, and supplemental videos (4-8), the application of current to both a saturated film and stripe phase can lead to the formation of a skyrmion phase.

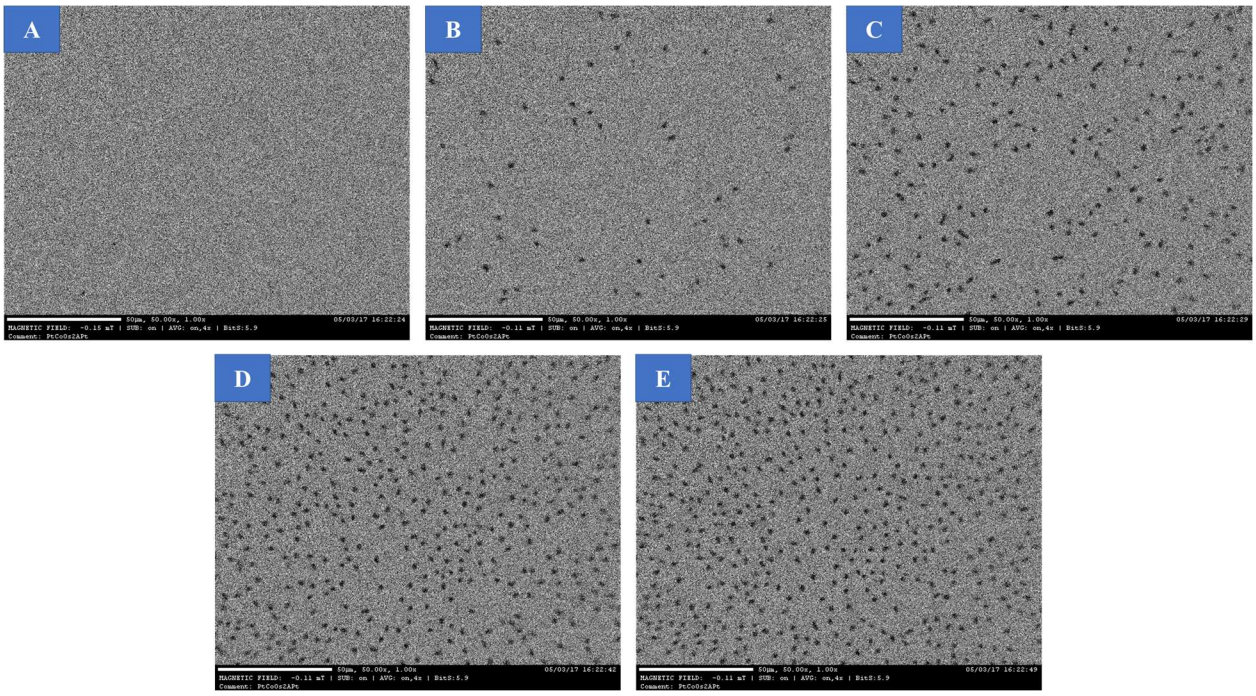

Figure 57: Field induced nucleation of skyrmions from saturated film over time. Field is brought down from saturation to -1.1 Oe out-of-plane field. A shows starting state. Elapsed time between images is varied to observe entire process. Elapsed time from image "A": B =1.25sec, C = 5.75sec, D= 18.75sec, E=26.25sec.

Normally, skyrmions are nucleated within a narrow field range by the slight fluctuations in the system due to temperature as seen in Figure 57. However, nucleation of skyrmions from the saturated state occurs when a current is applied to a saturated film that is slightly above the field for skyrmion nucleation. Above a critical current, skyrmions will begin to form from the uniform state – without well localized defect sites or a constrained current geometry. Stripes can be formed at this point but are quickly annihilated into skyrmions. This can be seen in the difference between Supp. Video 6 and 7. Additionally, a similar behavior can be seen when working at a field slightly

below the skyrmion and stripe coexistence field range. Applying a current causes the stripes to move, and at a certain current density the stripes will break apart and collapse into skyrmions.

As shown in the above Figure 57, Figure 52 and supplemental videos 3, 7 and 8, both field and current nucleation methods result in a close packed skyrmion lattice if left for sufficient time. During field-only nucleation, the lattice sites will slowly fill over the course of several seconds by thermal nucleation. Random fluctuations in the direction of the magnetization of the film will spontaneously form skyrmions. These skyrmions will remain if the field is increased slightly above their nucleation range. Similar to the way the stripes collapse to skyrmions, these skyrmions will remain stable even at higher fields. For current nucleated skyrmions, the current nucleation effects will form a close-packed skyrmion lattice above or below the otherwise nominal formation field range – even forcing out the stripe phase. For both methods, at fields slightly above this window, these skyrmions persist although they may slowly depopulate by thermal activation. At fields slightly below the skyrmion range, some will attempt to expand into a stripe phase, but their population will be blocked by skyrmions until enough skyrmions are thermally depopulated.

It is important to note that in the previous discussions, the sample geometries do not allow for a precise control of the current flow and current density. Given that interest in skyrmions primarily comes from the implications for devices and memory applications, there is an interest in exploring nucleation and motion of skyrmions in geometries that allow control and measurement of drive currents. Thus, two forms of patterning were done to create varied sizes of devices. Both lift-off based photolithography and a photolithography defined etch were used with success. It is worth noting that with the delicate dependence on Os thickness, depositing into a lithographically defined template and performing lift off can produce magnetic inhomogeneity regions at the edges of the film due to shadowing effects from the mask. Using a lithographically defined mask and

performing a plasma etch has a chance of modifying the properties of the interface through annealing, but with precautions this effect can be avoided. While the edges of the etched sample appear rough, the magnetically-altered region is much less significant than in the sample fabricated with the lift-off technique.

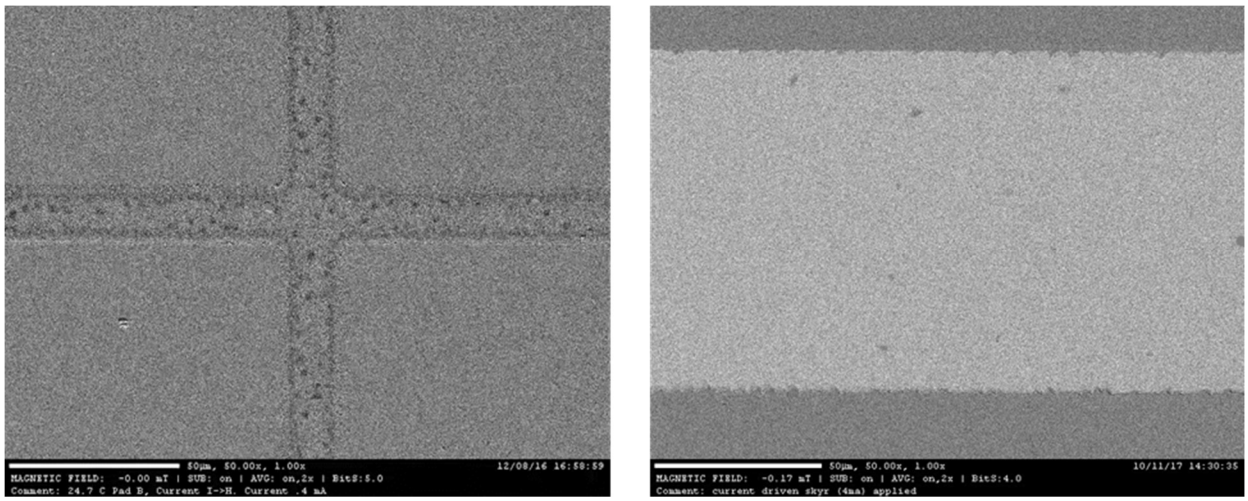

Figure 58: Two methods of lithographically defining geometry. At left is a 20 micrometer wide Hall cross defined by lift off as discussed in the fabrication section. Due to the high sensitivity of the Pt/Co/Os/Pt films to layer thickness, the small change in composition at the edges has damaged the edge, making transport measurements difficult. At right is a 100 micrometer wire from the same cross geometry, patterned by etching. The edges here are visually rougher, but do not experience the same composition gradient.

In order to properly address the motion of the skyrmions with respect to the current, the method of their movement must be addressed. With the skyrmions displacing in the direction of the conventional current, the driving force is suggested as the spin-orbit torque (SOT) arising from the high spin-orbit interaction of the Pt bottom layer. For an electron current traveling in a heavy metal layer with high spin orbit coupling, the conduction electrons will experience a deflection dependent on their spin. This will cause a polarization of the spin current at the interface between Pt and Co dependent on the direction of the current flow. This behavior can rule out spin transfer torque (STT), as the domains do not move in the electron flow direction. This also confirms the nature of the domain walls as Néel walls as SOT does not couple to Bloch type domain walls. The

chirality of the domain walls is also confirmed with the observation of the skyrmion Hall effect later on in this dissertation, as well as the motion of all textures in the same direction with the application of current. In addition, as will be shown later, the topological charge of the system (in the $\vec{G} \times \vec{v}$ term of the Thiele equation) will result in the textures all being deflected in the same direction – an indication that their topological charge is equal.

In Figure 58, the two features used for the current based manipulation of skyrmions in wires are shown. The motion of the skyrmions within the wire is due to the spin-orbit torques arising from the bottom Pt layer, and their chiral nature results in a deflection known as the skyrmion Hall effect. The topological charge due to the winding of the domain wall creates a deflection of the skyrmion as it is moved by a current. This deflection changes based on the chirality of the domain wall – thus it is possible to discern both the presence of chirality and the difference between one circularity and the other. While it is possible to perform this experiment with isolated skyrmions in a wide wire, the high thermal mobility and ease of formation of the skyrmions in our systems makes this difficult. In this case, the structure patterned in Figure59 was used. Tracking the velocity of the skyrmions is critical for the potential of applications, however doing so is dependent on having a well-defined current density and absence of pinning defects. For the 20 micrometer hall cross system, tracking the skyrmion velocity versus the applied current density yields promising results.

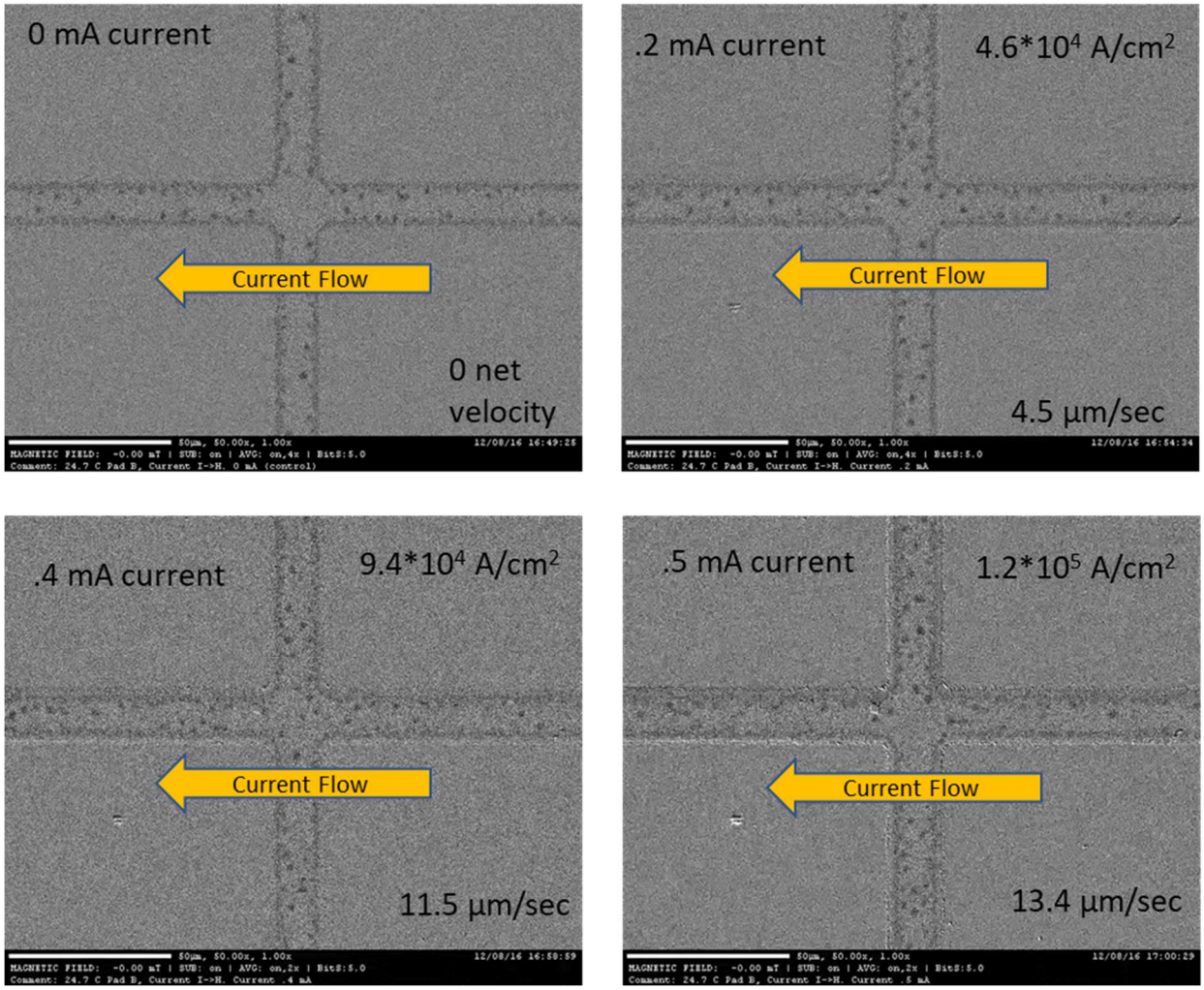

Figure 59: Skyrmion propagation in 20 micrometer hall crosses. The 20 micrometer hall crosses above were patterned with photolithography and defined by lift-off. Contacts were applied, and continuous current was applied from right to left along the long bar of the sample as shown in the image. 10 skyrmions were tracked by hand for each current and velocity was calculated from the frame by frame average.

Another enticing characteristic of skyrmions is that high-velocity motion can be obtained using current densities several orders-of-magnitude smaller than those needed to move domain walls at comparable velocities. Tracking the skyrmions can be done either by hand or by automated process, and shows a near linear increasing relationship with the current density applied. The experimental setup used to track skyrmion velocity is shown Figure 59 above. By collecting the images of skyrmion motion at a set framerate, the displacement of a skyrmion between frames can

be used to calculate the velocity. However, due to the well-defined geometry of the Hall crosses discussed in the previous section and the fact that we didn't observe a prohibitive number of pinning sites, the Os skyrmion samples meet the requirements for velocity measurements.

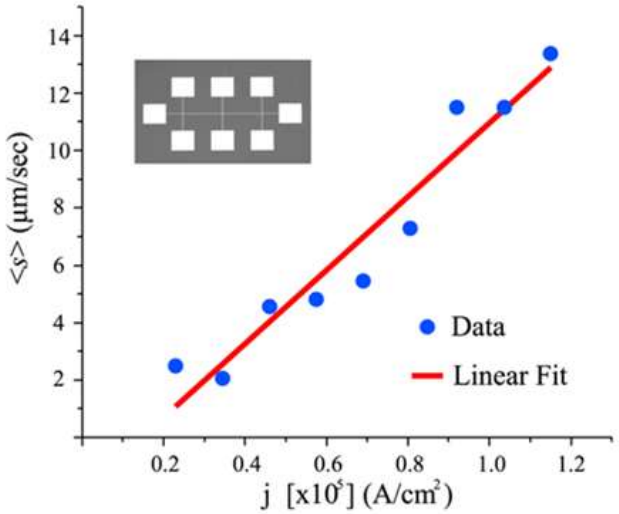

Figure 60: Velocity of skyrmions in 20 micrometer hall cross versus applied current density. 10 skyrmions were tracked manually for each current setting under a single field value.

The velocity of the skyrmions in this experiment relatively is low, within the creep regime. If we drive the skyrmions with higher currents we encounter difficulty in definitively tracking the skyrmions at high velocities and currents. Additionally, as seen in the full film samples there is a current nucleated cascade of skyrmion formation at high currents. This limits the possibility to track a single skyrmion in high-pulsed-current cases. Edge effects in the small lift-off defined hall cross create a damaged region that does not support skyrmions, which can reduce the path length of an individual skyrmions. The width of this inhospitable region was observed at around 2 micrometers wide for each side, which reduces the available skyrmion area to around 16 micrometers. For 2.3 micrometer (around 3 micrometer) skyrmions with an average lattice spacing of around the same size, this corresponds to between 3 and 4 possible skyrmion channels in the device, with the channels at the edge possibly hopping to the inhospitable regions. Thus, larger

devices were required to properly track and observe skyrmions in long path lengths. However, it was still possible to use these devices to test for the chirality and topological charge of the skyrmion system via the skyrmion Hall effect. Since the textures have been seen to all move in the same direction with the application of current, they have the same chirality – but in order to check for a uniform topological charge, their deflection due to the Magnus force needs to be evaluated. If the skyrmions are all deflected in the same direction by the $\vec{G} \times \vec{v}$ term determined by their topological charge, they will be confirmed as having the same winding number.

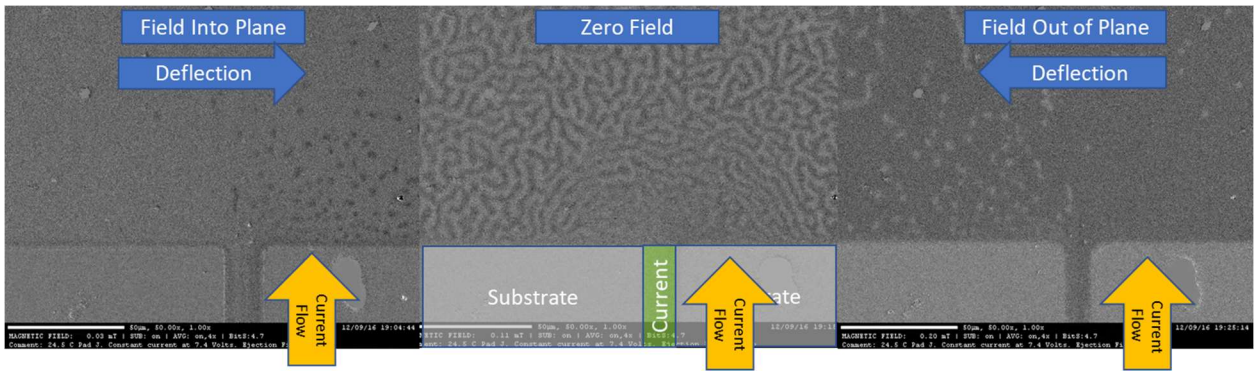

Figure 61: Observation of skyrmion chirality-based deflection. Current flow from the 20 micrometer wire into the expansion pad, driving stripes and skyrmions from the wire. Into plane field (negative field) results in dark skyrmions while out of plane field (positive field) results in light phase skyrmions. Stripes at zero field (center) are not deflected by a chiral structure, and expand in a circular wavefront from the current source. Skyrmions are deflected depending on their chirality – to the right for the dark phase skyrmions, and to the left for the light phase skyrmions.

In order to further confirm that the features seen are skyrmions, the chirality of the skyrmions can be examined by searching for the skyrmion Hall effect. In this orientation, current flow is vertical from the wire into the expansion pad. The current in this segment of the wire is above the forced stripe and skyrmion nucleation current, and the result is that this 20 micrometer section of wire acts as a skyrmion "gun". The field is scanned from complete saturation through the dark skyrmion phase, then the stripe phase, and then the light skyrmion phase. As can be seen from the images, the dark skyrmions are deflected to the right, while the light skyrmions are

deflected to the left. The balanced stripe phase is not deflected at zero field. This shows a clear distinction between the dark and light skyrmions – the two different orientations (corresponding to different charges due to field orientation) are deflected in different directions as per the skyrmion hall effect. In the absence of direct imaging of the domain wall via BLS, MFM, Lorentz TEM, or synchrotron imaging techniques, this is a significant signature of the presence of skyrmions as opposed to achiral bubble domains. [99]

Chapter 4, Section 4:
Tracking Nucleation Dynamics of Current-Forced Skyrmions

In order to measure the current induced effects of skyrmions in a larger system, a 100-micrometer wide hall cross geometry was patterned by etching as in Figure 58. Several critical observations were made from the device. Hysteresis loops were taken at a number of closely spaced temperatures, which showed again the strong effect of heating on the sample. Due to the slight difference in composition between samples, this sample exhibits skyrmions at the slightly higher temperature of 34 degrees C. Once on the heater stage, current leads were applied to supply current along the long axis of the sample. A sequence was used to control the field history and application of current, while current and field were varied in sequence. This provides a wide observation of the skyrmion formation across both field and current parameters with comparable results. Current applied was from 0.5mA (for a current density of 2.27×10^4 A/cm^2) to 4mA (1.81×10^5 A/cm^2) with data shown at 2mA (9.08×10^4 A/cm^2) and 3mA (1.36×10^5 A/cm^2).

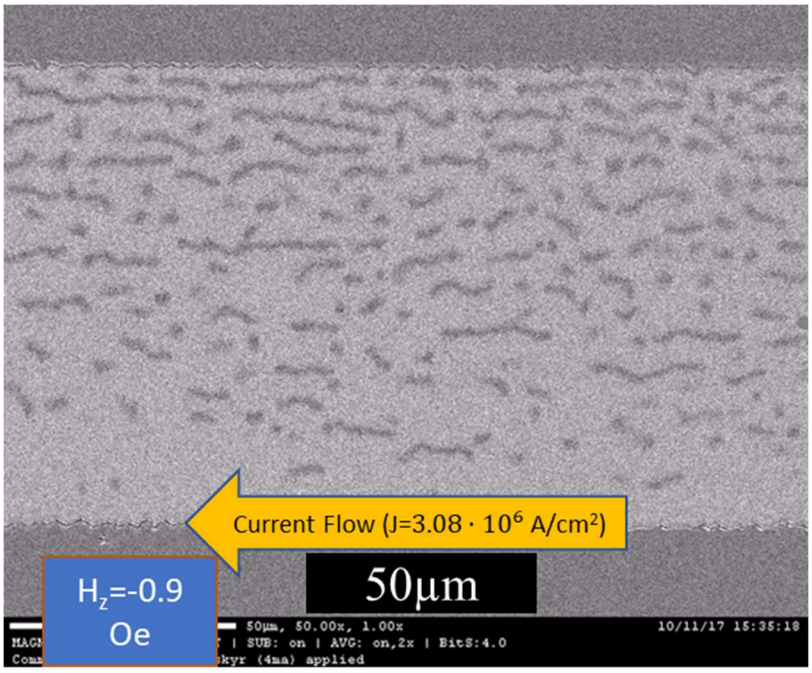

Figure 62: Skyrmions in 100 micrometer hall cross lead, patterned by etching. Skyrmions are in motion under the application of 4mA (1.81×10^5 A/cm^2) of current in the direction specified. As can be seen, stripes and skyrmions are in coexistence, with the stripes extended by the applied current and pinning sites.

The measurement procedure was as follows for a sample with negative field direction: Apply a large (40 Oe) field in the negative direction, apply a large (40 Oe) field in the positive direction, apply a small (2.5 Oe) field in the negative direction and take a background, then go to the final target negative field (between 1.7 and 0 Oe). With the background subtracted, the movie starts and the first 10 seconds of field-only nucleation are observed. After 10 seconds of field only, the current of a given amplitude is applied and the propagation and nucleation behavior is observed. After 60 seconds of current, the current is removed and the behavior of the system is observed for 20 seconds. Afterwards, applied field is removed and the system relaxes back to the stripe phase. This produces a cross sectional view of the nucleation behavior in the sample.

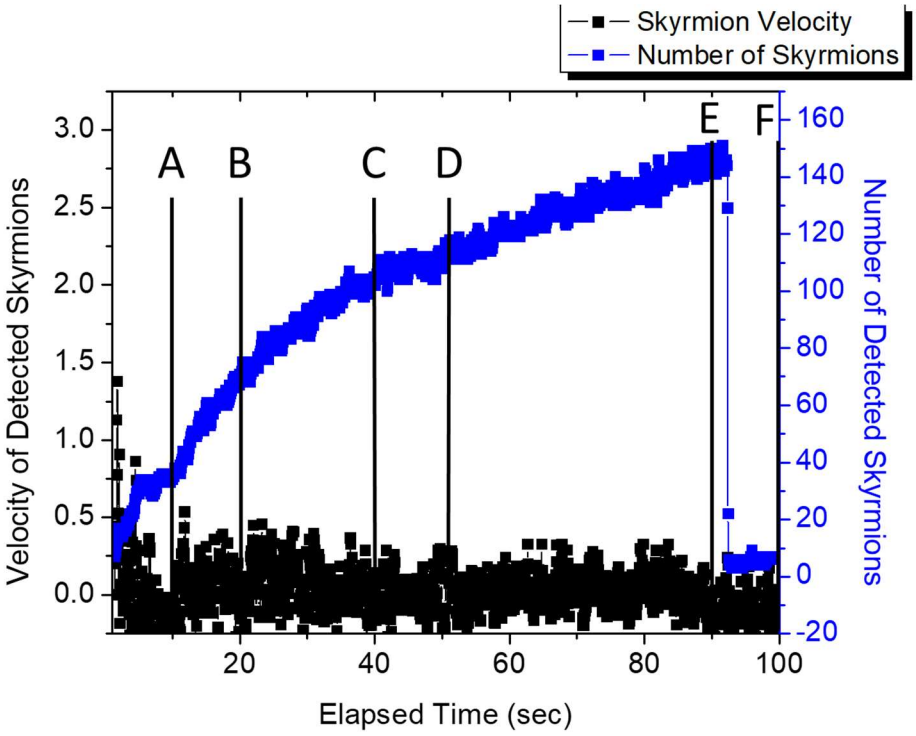

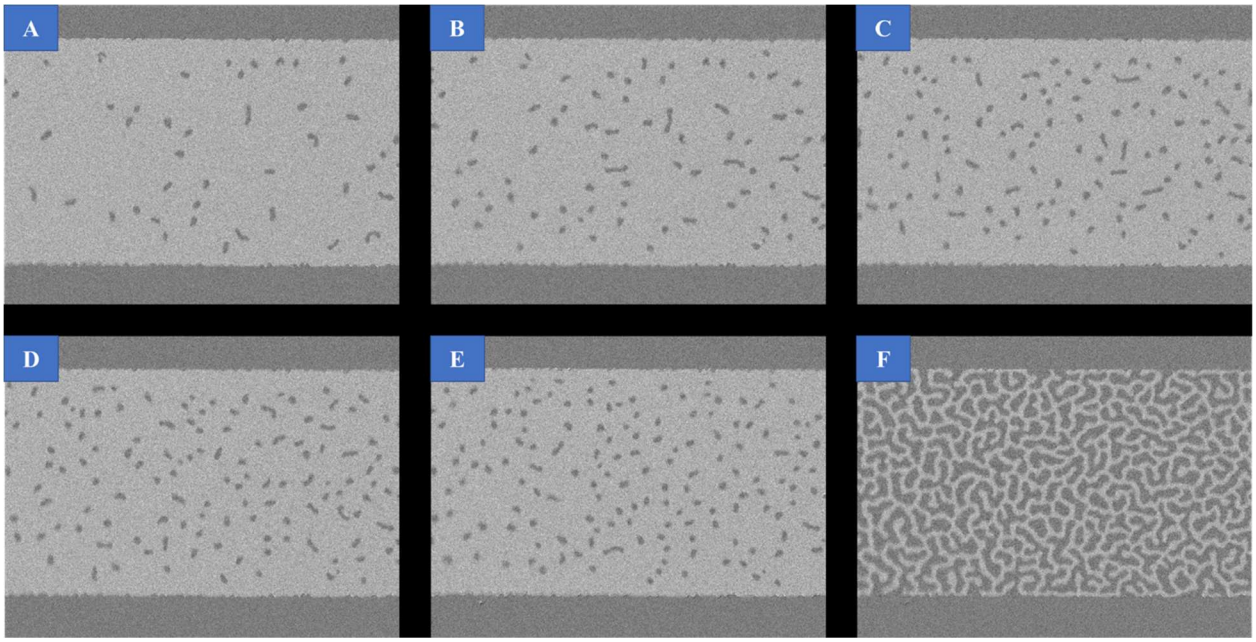

Figure 63: Population and density of skyrmions at low (0.5mA) current. Current density is 2.27×10^4 A/cm^2. Pictures (lower) are taken from corresponding points labeled on the graph (above). Times for images are 10 sec, 20 sec, 40 sec, 50 sec, 90 sec, and 100 sec from video start. Current is applied at 12 seconds, and removed at 70 seconds elapsed time. Field is removed at 94 seconds elapsed. This behavior is similar to that seen in Figure 57 of purely field nucleated skyrmions.

In Figure 63 above, the nucleation and propagation behavior at low current density is demonstrated. The net velocity of the skyrmions with 0.5mA of current is nearly zero, and there is not a significant change in the nucleation behavior when the current is applied. The skyrmion lattice fills the wire as a result of field induced random nucleation of skyrmions and stripes, and as the skyrmion phase becomes more dense the stripes collapse due to population pressure. Stripes and skyrmions nucleate from observed defect sites, as well as from the empty field. The defect sites were tracked and a map of the defect sites was created.

As previously noted, the skyrmions move in the direction of the applied current due to spin-orbit-torque (SOT) [100] [101]. However, with the constrained geometry, it is possible to observe additional effects including defect induced nucleation and the skyrmion Hall effect [101]. Again, it is possible to move the skyrmions with relatively low current densities of around mid 10^{-4} A/cm^2 to low- 10^{-6} A/cm^2, with speeds from 2-14 micrometers/second. At low current densities, field nucleated skyrmions have a thermally driven random hopping motion that combines with a relative bias due to the current flow. The combined stripe and skyrmion phase moves with the same relative velocity. In a field range where both stripes and skyrmions are stable, current does not have a significant effect on the population of either magnetic object.

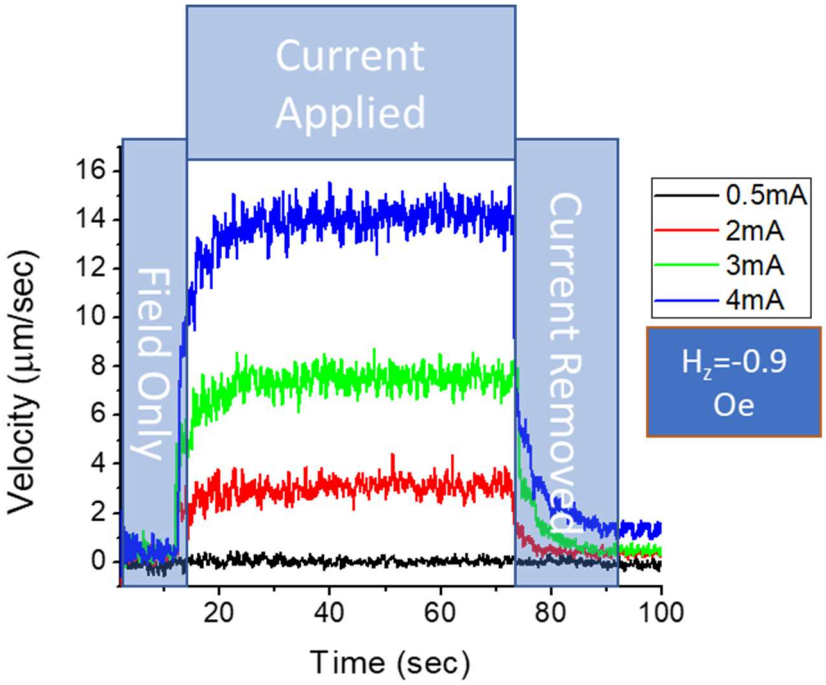

Figure 64: Velocity tracking of skyrmions. Current is applied around 10 seconds after the field is applied, and removed 60 seconds after application. Skyrmions are tracked by the APREX TRACK software. Average velocity of all skyrmion objects is displayed – noise comes from thermal hopping as well as nucleation events.

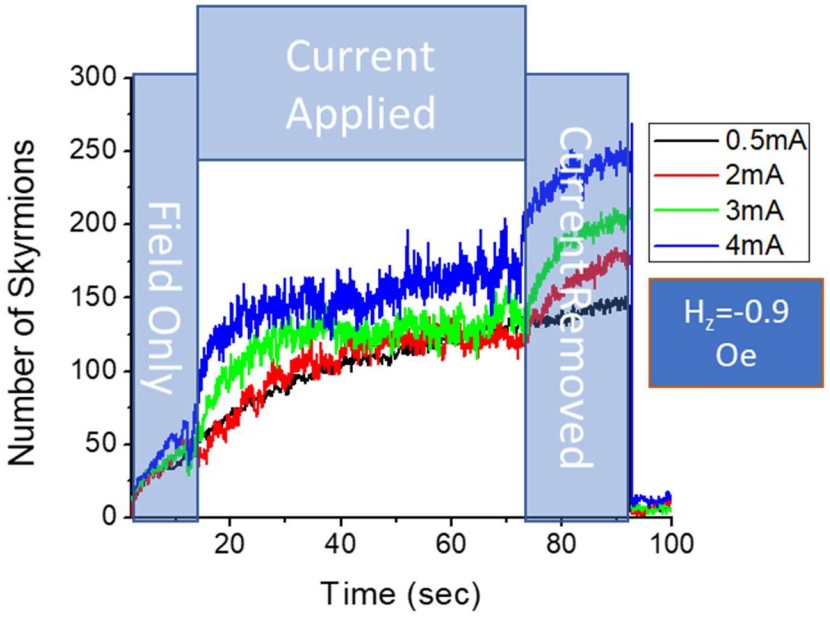

Figure 65: Example current induced nucleation of at multiple current amplitudes. This shows the similarity of the behavior in the field nucleated case at the beginning of the video, diverging when the current is applied (causing skyrmion and stripe nucleation), and removed (due to stripe collapse).

When higher currents and fields were applied to the system, there was an increase in the propagation velocity as expected, and as shown in Figure 65. There was also a significant change in the nucleation behavior of the system. Figure 63 stands in sharp contrast to Figure 66, where a higher current density was used at the same relative field. Before the application of current, the two nucleation behaviors are nearly the same, as would be expected. However, immediately after the application of the current, the skyrmions and stripes begin to move and align along the current flow direction. For the first few frames after current is applied, stripes move rapidly by extending their front wall into empty space. Skyrmions can be either driven as whole units, or can be broken into a stripe pair of half-skyrmions connected by a long wall. [97] The system reaches a roughly plastic flow model where skyrmions and stripes move in flow channels defined by the width of the

lattice. Pinning sites are observed and interact with the stripes by pinning the rear wall of the stripe. The entire lattice moves by a combination of biased thermally driven hopping amplified by the current flow. This measurement restricted itself to low current amplitudes in order to continuously observe the motion of the skyrmion lattice, as well as to control any potential effects of resistive Joule heating, given how sensitive this system is to temperature.

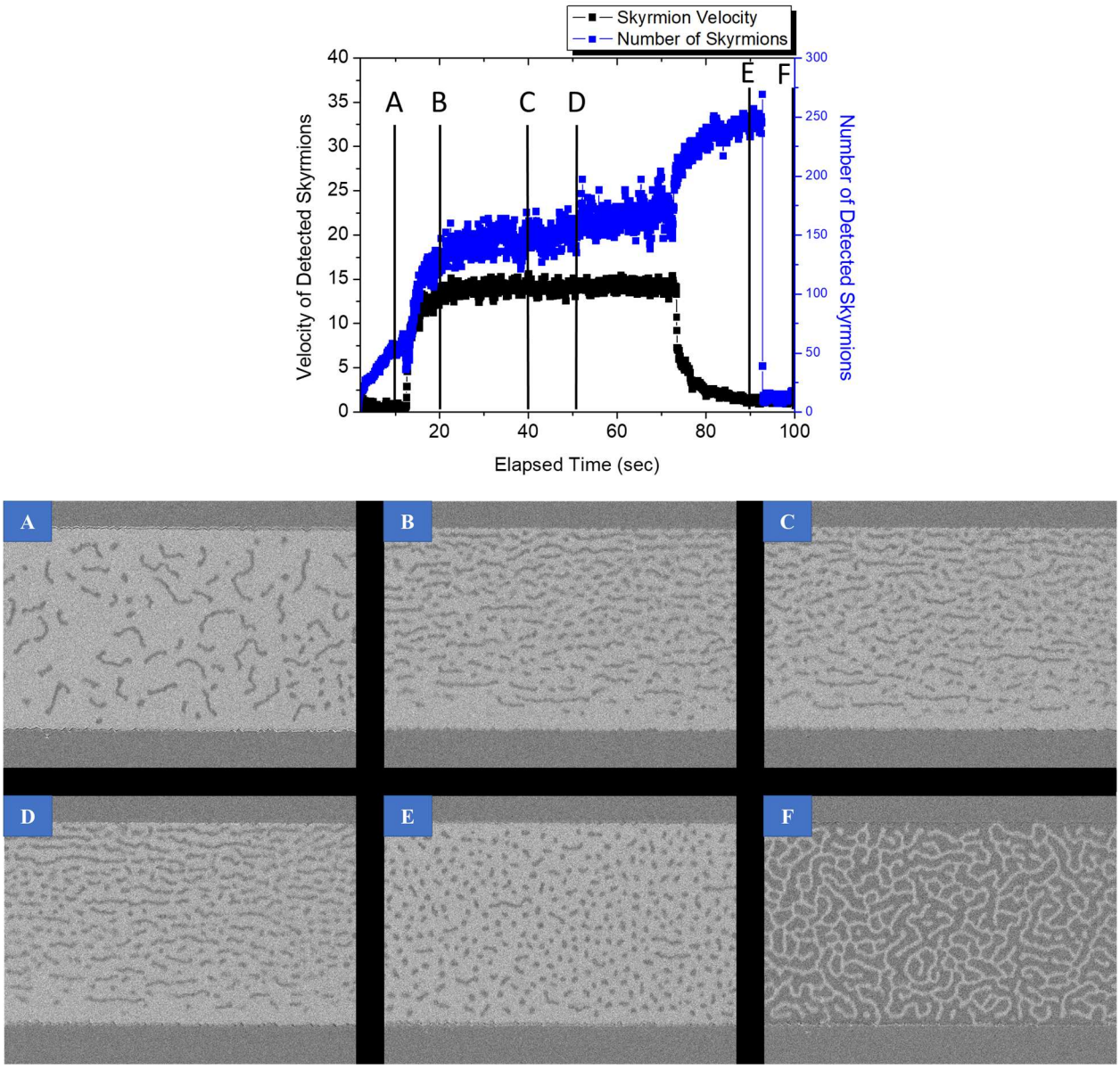

Figure 66: Current nucleated behavior for an applied current of 4mA. This sample uses the exact field history and current history to that found in Figure 63.

As the above figure shows, there is a direct relationship between the creation of additional skyrmions and the current driven through the system. Taking place with the same field history, the creation of these skyrmions is related directly to the driving current. It is apparent that there are two regimes, for the current induced formation. As seen in Figure 63, at low currents, there little to no induced nucleation. For the 0.5 mA (2.27×10^4 A/cm^2) case, the formation rate of the skyrmions is almost flat, and does not change appreciably as the current is switched on and off. At 2mA (9.08×10^4 A/cm^2), there is not a significant number of skyrmions immediately nucleated by the applied current, but once the current is removed, stripes that were extended by the current will collapse under field (in the "Current Removed" highlight). However, upon reaching 3mA and 4mA (1.81×10^5 A/cm^2 and 1.36×10^5 A/cm^2 respectively) of current, there is a sudden increase in the number of skyrmions as the current is turned on, as well as a sudden increase in the number of skyrmions when the current is turned off. The first event is due to the current induced nucleation of skyrmions and stripes from defect sites and current-broken stripes. When the current is on, stripes are nucleated and extended from defect sites, but are excluded from tracking by the software.

Two primary types of nucleation occur above a critical threshold current. First, stripes are formed from defect sites, as seen in the example filmstrip below in Figure 68. These defects are caused by localized inhomogeneities in the film and local non-homogenious magnetic order. These point defects can be caused by small debris on the film surface during deposition, or by local roughness in the film surface. However, independent of their source several such defects have been marked in the above system by observing where skyrmions initially form. A local inhomogeneous field, combined with an inhomogeneous current, can give rise to either a skyrmion or stripe domain. If a skyrmion is modeled as a continuous distortion of a domain wall that is topologically

protected, it is possible to model a stripe as two half-skyrmions at each end combined with two "straight" Néel walls. These walls, while energetically unfavorable, lack the energy required to drag one half-skyrmion to the other. Stripe collapse behavior as seen in field-nucleated events, indicates the structural stability of the endcaps over the rest of the stripe. However, it also becomes apparent that there is a possibility for the stripes to undergo different forms of breaking and collapse. When driven in current, stripes that are parallel to the current will be driven at both ends and will largely continue to flow parallel to the current. However, stripes that are perpendicular or cross to the current direction will experience a shearing along the length of the stripe. With this same hopping behavior that is observed in the skyrmions, the stripes will develop local discontinuities and curvature. With sufficient change in he curvature, a distorted stripe will break at the point of distortion and form a pair of half-skyrmions that are matched to their partners on the new ends of the stripe. The shattered stripe behavior can be seen additionally, when one end of a stripe pins to one of the localized defects [97].

At higher currents, forced nucleation of stripes and skyrmions from both uniform magnetized areas and nucleation sites is observed. Previously, in an unpatterned film system, the nucleation of a skyrmion lattice was observed with the application of an electric current. However, without the confined geometry the relative direction of current flow and skyrmions was difficult to analyze. In the patterned wire, a similar cascade effect is observed at sufficiently high currents, however only on one side of the sample – corresponding to the skyrmion Hall deflection angle.

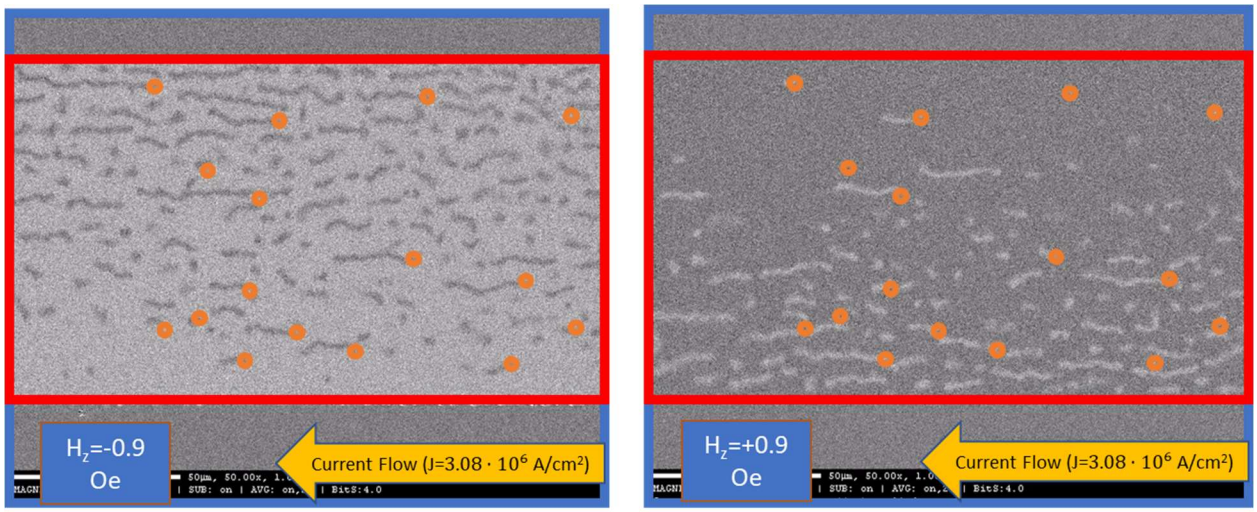

Figure 67: Skyrmion Hall alignment of different chirality of skyrmions. Dark phase (down field) skyrmions align to top of wire, while light phase (up field) skyrmions align to bottom of wire. Interestingly, defect sites (marked in orange circles) are most active when nearby population is high.

This effect as shown in Figure 67 is interesting, as it implies the presence of skyrmions and stripes enhancing the nucleation of stripes and skyrmions from defect sites as well as the breaking of stripes into skyrmions. In the above example, defect sites already within a high population skyrmion zone are more active than those in low population areas. This is true for the high current regimes (3 and 4mA of applied current). This effect is suggested to come from triggering of the defect sites and extended stripes by the inhomogeneities in current and blocking from magnetic textures. These current effects can arise from local film texture, as well as the deflection of the current due to the effective moment of the skyrmion (causing a topological Hall effect within the texture).

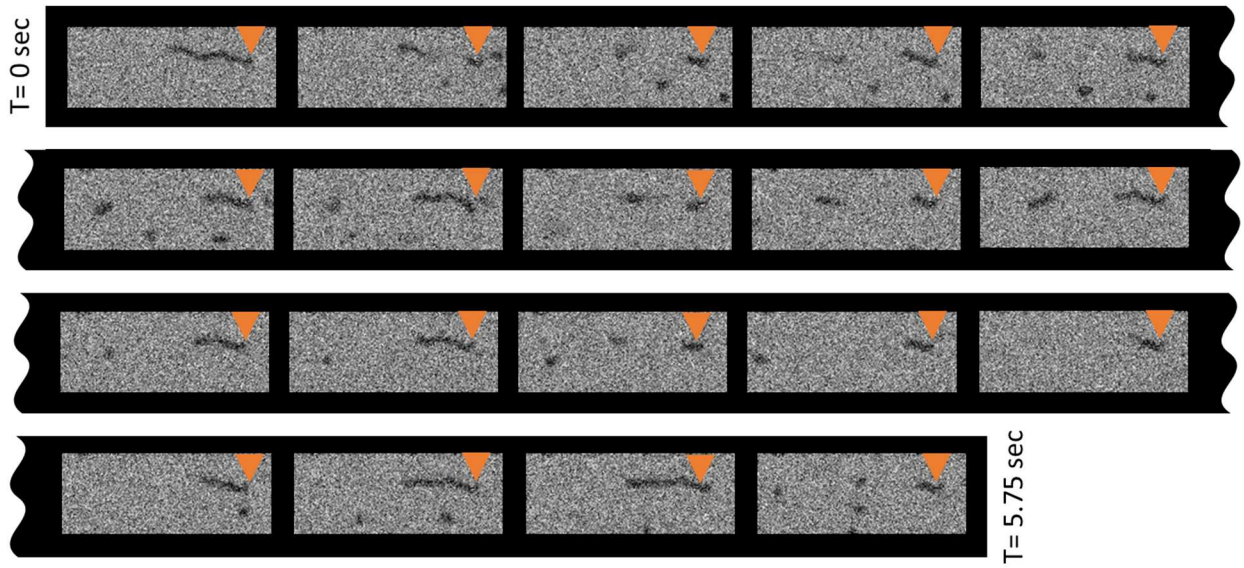

Figure 68: Stripes and skyrmions formed from defect site (tip of orange triangle). Applied field is -1.7 Oe with 4mA of current applied from right to left. Stripes extend from the defect site, pulled by current. The stripe can break along its length, giving rise to a skyrmion.

The method of nucleation of skyrmions and stripes from these defect sites is also interesting. At high currents and low fields, the stripe phase dominates and long stripes are formed at the nucleation sites. The stripes have no preferential orientation, and thus are evenly spread through the film. At high currents and high fields (significantly above the survivable field for the skyrmions), transient stripes are nucleated and stretched by their lead wall from the nucleation site. A stripe that breaks from its nucleation site quickly collapses to a skyrmion, and at sufficiently high field the skyrmion itself will have a very brief lifetime before being annihilated. In the intermediate phase, however, it is possible to create skyrmions and stripes via current even outside of their nominal survivable phase.

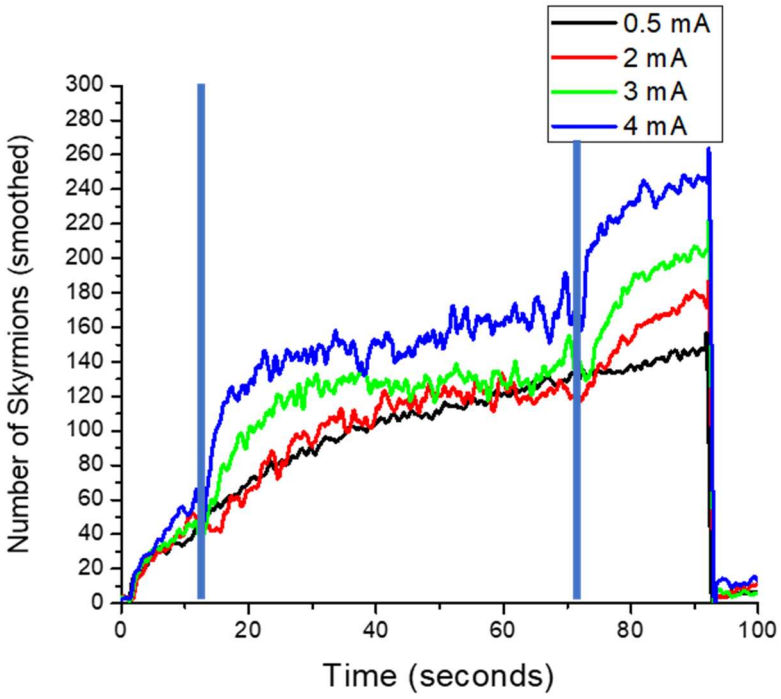

Figure 69: Skyrmion tracking at -0.9 Oe across application of current. First blue line marks current turning on, while the second marks the current being turned off. This shows the different behavior between the low (0.5mA) and high (4mA) current cases (2.27×10^4 A/cm^2 and1.81×10^5 A/cm^2 respectively).

Tracking the number of skyrmions at the same field, with a low and high applied current, two significant differences can be easily seen. At low currents, below the forced stripe and skyrmion nucleation from defects, the rate of skyrmion formation is not significantly affected by the current being turned on or off. However, for high current amplitudes, two significant skyrmion nucleation events are seen. The start of the first nucleation event comes with the current being turned on, where the film will fill with stripes and skyrmions nucleated by the defect sites and by breaking propagating stripes. At the tail end after the system has filled with stripes and skyrmions, the current is turned off. This results in a jump in the number of skyrmions as the stripes which had previously been stabilized by the pulling of the current are now unstable under field. These stripes will collapse along their long walls, producing another set of skyrmion nucleation events.

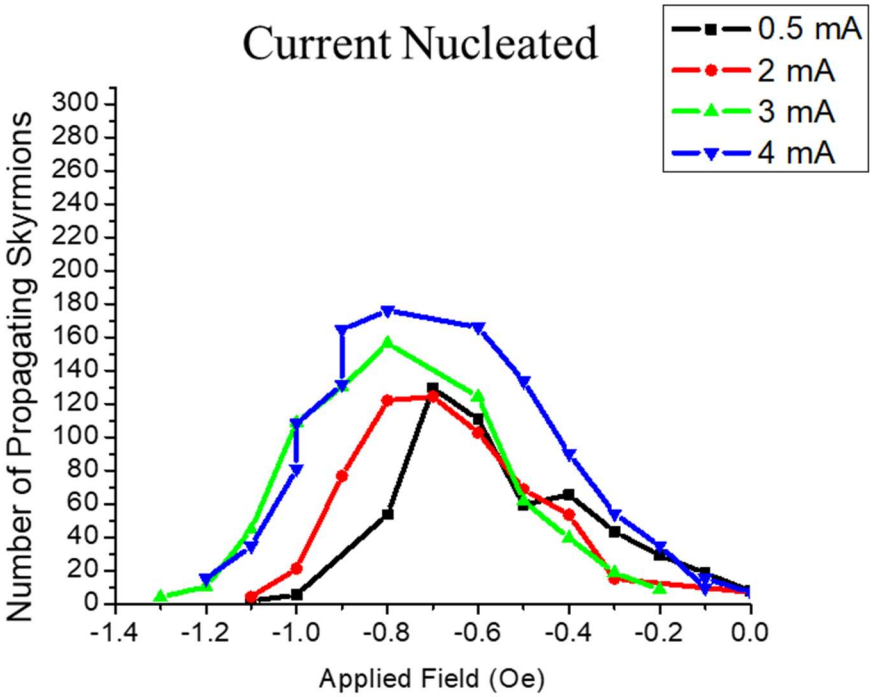

Figure 70: Current induced nucleation of skyrmions during the application of current. Data for this figure was taken and averaged for 10 seconds after point "D" noted in Figures 63 and 66.

The nucleation behavior for a variety of currents and fields are shown above in Figure 70, where the number of skyrmions nucleated by current (averaged for 10 seconds after the first 30 seconds of applied current) is shown as a function of both applied field and current. At small currents of 0.5 and 1 mA, the system is primarily field nucleated, and nucleation primarily occurs in an 0.5 Oe wide range around 0.75 Oe. However for larger currents, the current induced skyrmions exist both in larger numbers and survive at higher fields during the application of current. As the current is applied, the survivable field range expands to around 1 Oe wide, with 1.3 times more skyrmions formed for high current densities (4mA) over the non-forcing currents (0.5 mA).

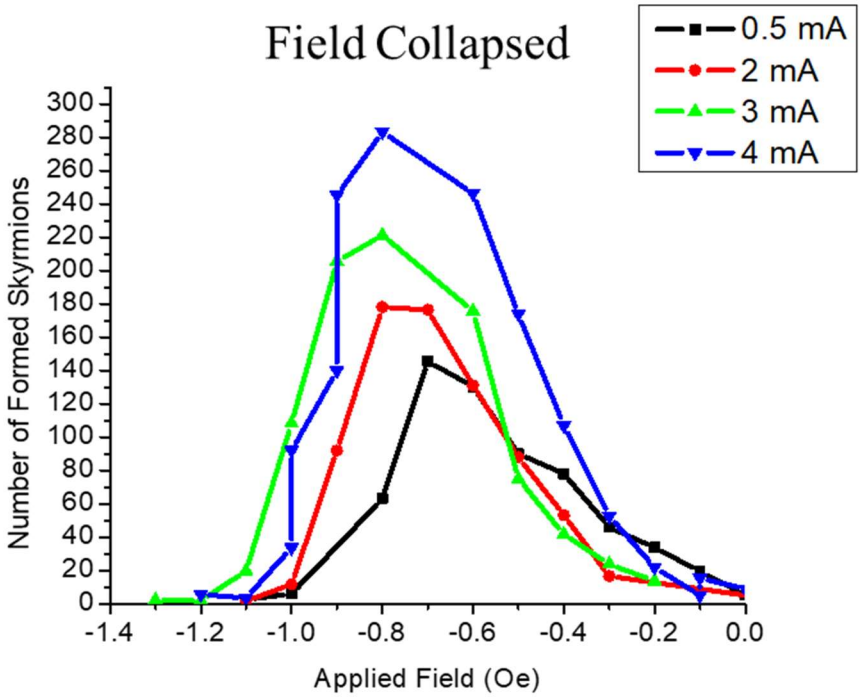

Figure 71: Field based collapse of stripes to skyrmions. Stripes previously extended by the current will collapse once field is removed. This is in comparison to Figure 70. Data was taken for 5 seconds before field removal, point "E" in Figures 63 and 66.

This effect is even more pronounced after the current is removed. Figure 71 shows the number of skyrmions in the film after the current has been removed for 15 seconds. As can be seen, the current induced nucleation behavior of the system is even more pronounced with the stripes that had been extended by current instead collapsing down to skyrmions. This suggests several phenomena. First, that for high and low fields (toward saturation and stripe phase respectively), that current flow stabilizes a skyrmion phase within the wire, as well as nucleating and driving stripes. Secondly, that for fields within the skyrmion zone, that high current densities increase the number of stripes within the film, and that collapse of these stripes happens at short timescales under field. Performing the experiment under steady currents for the observation of all of these regimes, and suggests a mechanism for the system behavior during high current density pulses.

Chapter 4, Section 5:
Theories of Stripe to Skyrmion Transition

The experimental observation of coexisting stripes and skyrmions and the manner in which stripes collapse to skyrmions allows for the evaluation of theoretical treatments of skyrmion formation. Theorists [1] [95] have modeled skyrmions and their partner stripe systems in a variety of ways. One way is as a pair of half-skyrmion "endcaps" with a pair of long Néel walls connecting them. If this were the case, there could be several methods that a skyrmion could be nucleated from a stripe. First, at high fields the long stripe wall is much more energetically unfavorable than the wound endcap. Thus when combined with the random thermal hopping of the endcap, at high fields the stripes will slowly collapse due to their instability. This is primarily due to the strength of the applied field, and can be seen in the sequence of Figure 72 below.

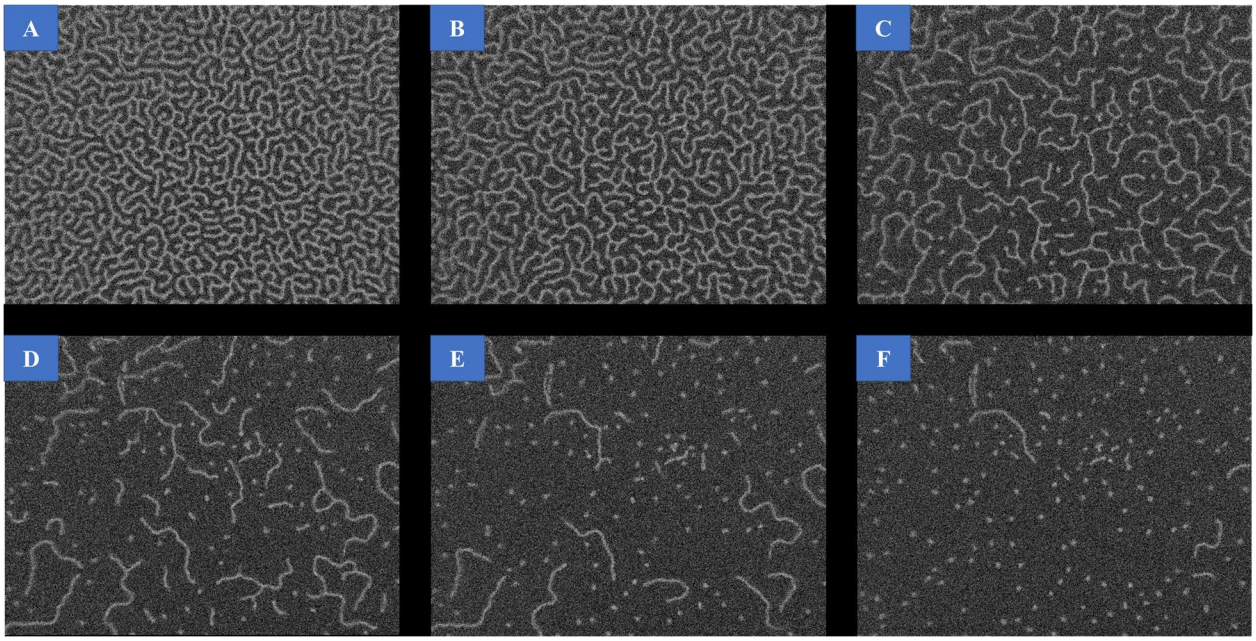

Figure 72: Stripe phase collapsing into skyrmions due to field. Field is increased from 0 Oe to -1.3 Oe from A to D. System is then allowed to relax at -1.3 Oe from D to F. Elapsed time from to D is 13 seconds and from D to F is 5 seconds.

Under higher fields, this shrinking of the long straight wall is the primary way that stripes collapse to skyrmions. However, there is also a population-driven method for reducing the size of stripes until they form a close packed skyrmion lattice. Shown in Fig 73 below, a stripe that is bordered on its sides by skyrmions is very unlikely to extend its wall further. To do so would require it to displace a skyrmion and the surrounding lattice. It is far more likely for one endcap to move in a direction that shrinks the wall, as it does not need to displace the lattice. This is observed in the more close-packed lattice systems at relatively lower fields, or with current driven stripe transitions.

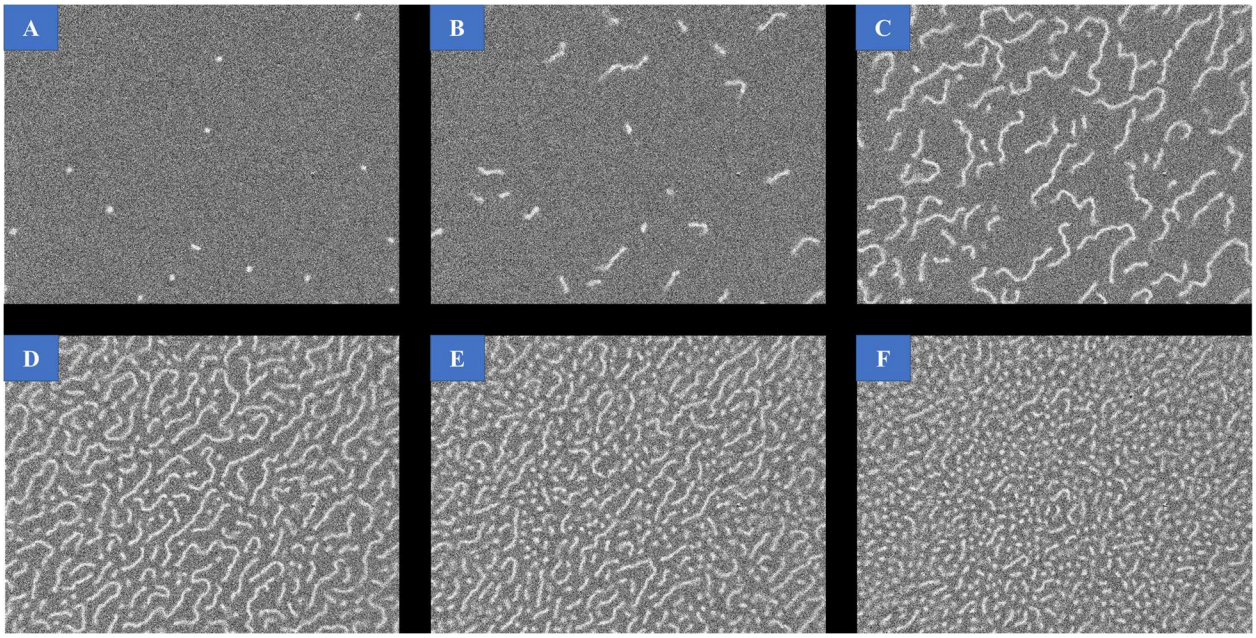

Figure 73: Stripe collapse as driven by population density. Field is steady at -1.1 Oe, which allows stripe and skyrmion coexistence. Constant current is applied to the unpatterned film from top right to bottom left, starting with A, sufficient to drive stripes within the film (but not induce ellipticity events). Elapsed time from A is given for each frame. B = 4 sec, C = 8 sec, D = 16 sec, E = 23 sec, F = 35 sec.

Both of these methods discussed above are primarily field-based, relying upon the combination of thermal activation of the system and applied field. However, as shown by [80] it is possible to nucleate skyrmions by the application of current. When driven by an electric current,

the Néel walls experience a spin torque that will drive the wall in the direction of the current flow (counter to the electron flow direction). This spin-orbit torque is suggested to arise from the bottom Pt/Co interface. As previously shown, a sufficiently high current can drive skyrmions into formation from empty field regions and drive the collapse of stripes. This relies upon a combination of current and field parameters, but is driven primarily by induced distortion in the stripes. Transverse stripes are broken quickly along the induced ellipticity events as they propagate in response to the current, as shown in Figure 75 below.

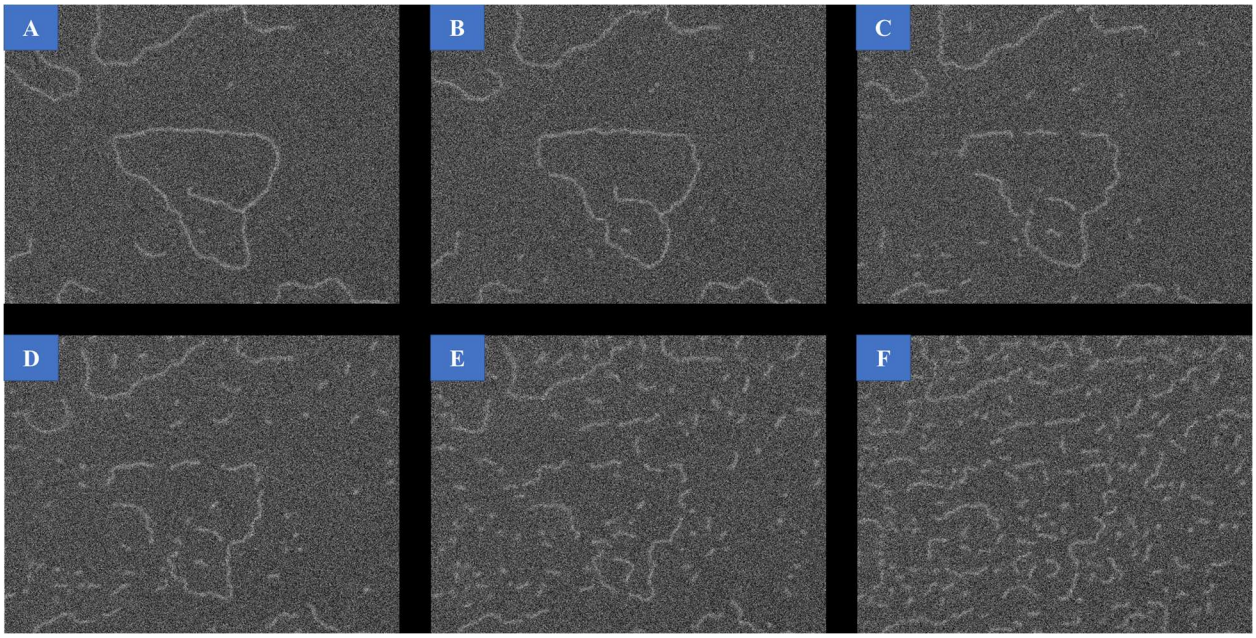

Figure 74: Transverse stripe shattering in open film. Current is applied from top right to bottom left, starting at image A. Elapsed time from A for each frame. B = 4 sec, C =7 sec, D = 8 sec, E = 9 sec, F = 11 sec.

For pinned stripes, the behavior in current is significantly different as seen in the wires (Figures 63 and 66). For the pinned stripes in a heavily populated film, they will extend by their lead wall along the direction of the current flow. This stripe will extend straight from the defect site, but is perturbed by the adjacent stripes and skyrmions traveling past. The current inhomogeneity and exclusion zone crated by the traveling stripe and skyrmions will generate a

kink or loop in the pinned stripe that will travel down its length. If sufficiently excited or of a sufficient curvature, the stripe will snap at the bend and the freed stripe or skyrmion will propagate down the wire. This excitation can be driven by the presence of additional skyrmions moving nearby the nucleation site or stripe.

This may serve to explain some of the crowding effect seen at the sides of the wire. Stripes and skyrmions will initially nucleate by field and current. As the skyrmions move, they will pile up due to the deflection caused by the skyrmion Hall effect [101]. The crowding of the nucleation sites may cause stripes to dislodge from the pinning sites, which would cause them to collapse under drive to form skyrmions. Alternately, the extended stripes will be driven by the current to form induced ellipticity events and may break at points along their length. This is enhanced by the passage of other magnetic textures along the length of the stripe. As indicated in the videos, the presence of skyrmions driven past the nucleation sites causes additional skyrmion or stripe textures to form.

The formation events of the stripe and skyrmion systems discussed in this dissertation are not yet well understood. Clearly the current exerts a driving effect on the defect sites with lowered anisotropy, causing one of the endcap walls to extend. This extension, combined with the instability of the straight wall and the pinning of the other endcap on the defect site results in the formation of more magnetic textures that in turn will propagate down the wire. As the straight wall is unstable, the system will generally favor the more stable skyrmion state. However, the drive supplied by the current may cause the two endcap walls to become separated if they pin on a defect site. As additional skyrmions and stripes nucleate from the defect sites and fill the wire, stripe states will become less probable as the more stable skyrmions occupy the available area. As observed in the population density map in Figure 69, there is a sharp initial increase in the skyrmion

density, before a final maximum population size is reached. The final relaxation density shows the process of how the stripes relax into skyrmions.

Overall, several valuable conclusions can be drawn from using steady current (rather than short duration pulsed currents) to nucleate and drive the skyrmions. This allows a clear observation of the active dynamics of the stripe and skyrmion motion and nucleation during the nucleation events. This also allows the system to come to a controllable steady state thermal equilibrium. Finally, there is a clear distinction between the current applied nucleation events and their driving effects on the skyrmions, and the relaxation event present when current is removed.

Chapter 4, Section 6:
Skyrmions in Review

The presence of skyrmions in the Pt/Co/Os0.2nm/Pt layers at room temperature is both intriguing and novel. While other interface-driven skyrmion systems are stable across a wide range of temperatures, and/or require cooling to below room temperature, the optimally designed Os-interface driven skyrmions exist in a narrow window around room temperature. The presence of Os at the top interface of the Pt/Co/Pt stack has a significant effect on the net moment and anisotropy of the system, driving the layer toward a spin reorientation transition with just 0.2nm of Os. That the system switches from out-of-plane to in-plane for such a small amount of Os implies that the Co/Os interface plays a strong role in controlling the properties of the system. The system has a thermally active stripe phase around room temperature due to the spin reorientation transition. This transition occurs over a temperature range of around 10-20 degrees C, and the skyrmion phase is contained within this temperature region. The skyrmions formed by field and/or current from this phase are also thermally active. Their characteristic hopping behavior due to thermal excitation gives clues as to their mode of motion while driven in the creep regime by current. While a characteristic feature of skyrmions is the low current density required to move them, these skyrmions show a combination of the thermally induced hopping behavior and the current driven bias even at low relative current densities. At higher current densities, the current driven nucleation behavior of the skyrmions provides a rich series of behaviors that manifest in real-time. The system is optimal for the observation of this nucleation and drive behavior in the Kerr microscope, allowing for the direct observation of skyrmion nucleation and dynamics over reasonable timescales. While the Osmium skyrmion systems will likely not be used for device and memory applications, due to their instability outside of a very narrow temperature window and

large size, they may continue to serve as an intriguing model system for continued study of skyrmion nucleation and manipulation.

Chapter 4 in part is taken from research submitted to be published as “Room-temperature observation and current control of skyrmions in Pt/Co/Os/Pt thin films.” R. Tolley, S. A. Montoya, and E. E. Fullerton in Physical Review Materials, (ML10007) (arXiv 1711.07101), and is currently under review. The dissertation author was the primary investigator and author of this paper.

Special Section 1:
3D Printing in Instrumentation Applications

As of the end of 2017, consumer applications of 3D printing have been significantly overhyped. The ability for fast prototyping and manufacturing is significant, but the bottleneck for many consumers is the design of the object to be printed. The quality and finish of the custom object is generally significantly below commercial injection molding and mass production. In addition, the care and maintenance of the 3D printer itself can be a significant factor in and of itself. For the enthusiast or a laboratory however, a 3D printer can open up the possibility of custom built components at a fraction of the cost of traditional machining.

3D printing or additive manufacturing in and of itself is not necessarily new. However, the development of low cost consumer grade microcontrollers with sufficient processing power to run the systems has provided significant advantages. Three major techniques of 3D printing exist, but most consumer grade machines are of one type. Fused Deposition Modeling (FDM) type machines are the most common, followed by Selective Laser Sintering (SLS) and Stereolithography systems respectively. FDM type systems rely on an extruded bead of thermoplastic that is translated through an XYZ tool path. SLS machines rely upon thermally fusing successive layers of powdered base material. Stereolithography systems rely upon exposure of a surface of photosensitive resin that hardens, with the surface moving along the Z axis of the sample.

For all systems, the first step is starting with a 3D volumetric model of the desired object. This computer model will be converted into a file type that can be read by a slicing program. The purpose of the slicing program is to convert the 3D model into a tool path for the 3D printer. It does so by first setting the model in a defined XYZ or R/θ/Z coordinate system, depending on the

coordinate of the printer. In most FDM type printers, the tool path is scanned along the XY plane, and the Z axis is stepped sequentially. Therefore, the slicer program will work by taking cuts or "slices" of the model along the Z axis. Depending on the height resolution setting of the printer, these slices may be between 0.05mm and 0.3mm in height. At each Z step, the slicer program will find the external walls of the model and prepare a path that the tool should follow to create those walls. Then, for enclosed volumes, an infill pattern is added for greater structural integrity. The output of the slicer program is a file of machine-readable code (typically "gcode") that tells the printer the path of the tool head through XYZ space, and how much plastic to extrude as it travels along that path. The gcode is then given to the machine in a file, and it will begin the process of following the tool path.

As an additive manufacturing process, there are several different important steps to consider when designing a model especially for printing. First, in choosing a growth (Z) axis, it is important to consider that the file will be printed from that axis up. While each printer is different, the FDM type printers typically have difficulty in printing overhangs, and printing separate suspended pieces is possible only by generating a supporting structure. While designing the model, it can be important to ask "How will this be built?" Avoiding overhangs when possible, or designing multiple part systems can be advantageous. If structural integrity may be an issue, avoid orienting long fins along the Z axis – the print is much stronger in the XY plane due to the continuous nature of the extrusion. A long, thin wall printed along the Z axis will be many individual layers that may snap at the layer point if pressed too hard. Additionally, check on tolerances of the printer before committing to too tight a design – while oversized parts can easily be shaved down or adjusted with a hobby knife, they may not be perfectly square or true. 3D printing offers significant advantages for quick manufacturing for certain applications.

Special Section 1, Subsection 1: Design and Fabrication of Kerr Microscope Pulser

One major advantage of 3D printing lies in the fast prototyping and fabrication of systems with relatively low tolerance. For small one-off projects, it is possible to design a base-system and then iterate over the course of hours or days, rather than weeks or months. In addition, the cost of producing a part or prototype is a few cents worth of thermoplastic rather than paying a machinist. This lends itself well to one-off semi-disposable additions to equipment that do not require vacuum compatibility, high structural loads or tight tolerances. It is perfect for designing add on parts for the Kerr microscope.

As previously discussed in Chapter 4 of this dissertation, the evaluation of DMI in a thin film can be approximately performed by measuring the asymmetry in the expansion of a domain wall. To perform this measurement, two elements are required. The first element is a strong in-plane symmetry breaking field, and the second is an out-of-plane field for the nucleation and propagation of the out-of-plane domain wall. While this can be accomplished by simply tilting the in-plane coil, this system lacks flexibility. A more advanced setup can use a pair of magnetic cols – keeping the large coil for the in-plane symmetry breaking, and using a smaller pulsed coil for more controllable nucleation and propagation of the domain wall.

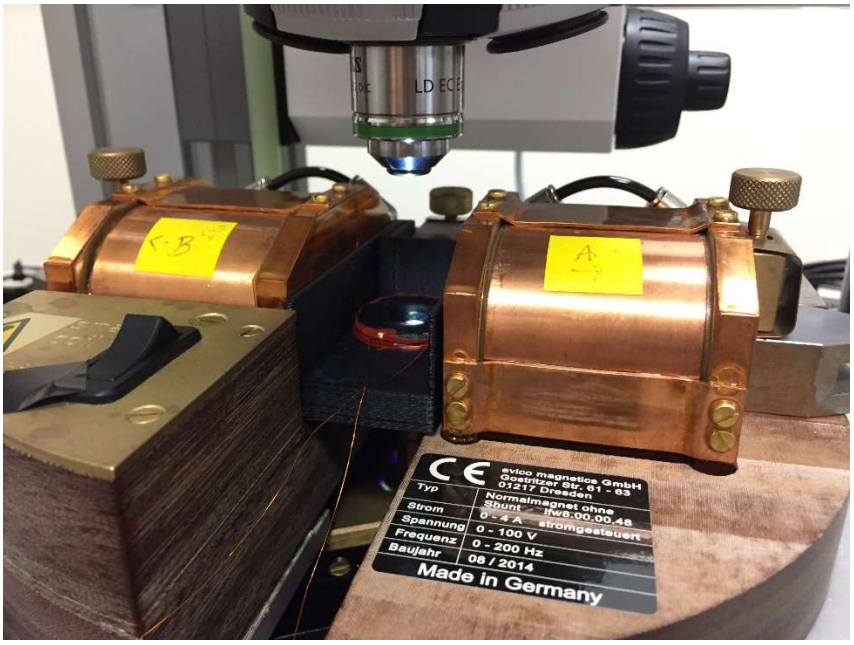

Figure 75: Pulse coil setup (center) installed in Evico Magnetics in-plane coilset.

In the Evico Kerr Microscope, this approach was partially limited by the design geometry of the in-plane coil. With only 36 mm between the coils used for the in-plane field, space is limited. In addition, if the sample rests within the coil (for best uniformity of field), then the system is even more constrained. An early version of the system attached a small hard drive voice coil to the sample mounting stage. At low in-plane field amplitudes, the system worked, but at higher in-plane amplitudes the pulse of the coil would create force that would move the sample holder and sample.

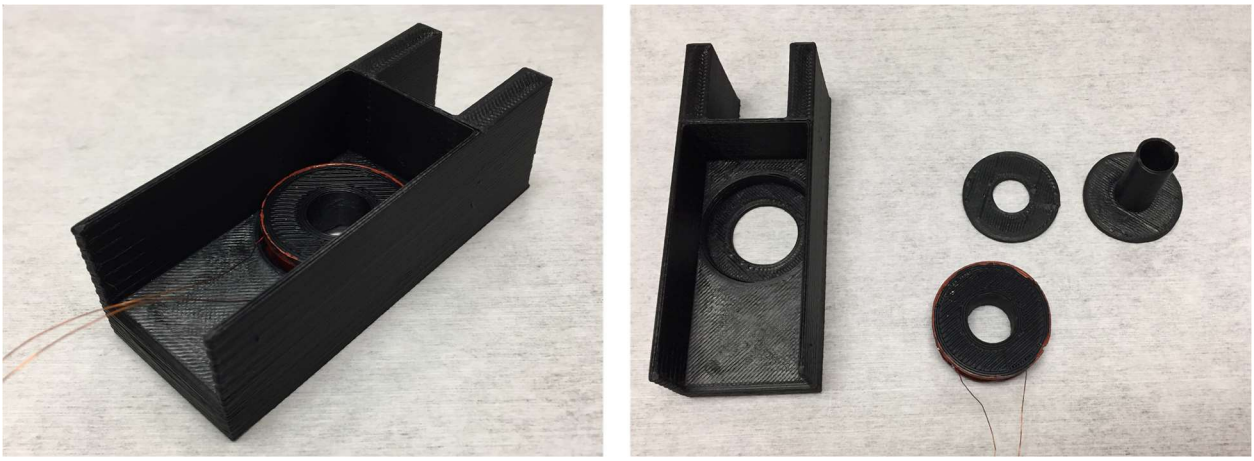

Figure 76: Pulse coil system for the Kerr microscope. Completed pulse coil installed in sled (left), and all component parts (right). Of note: the long tube on the coil core (upper right) is significantly longer than will be in final use – it is designed to be trimmed before winding the coil.

A series of designs were developed and prototyped, eventually settling on a combination of a mounting sled and a series of easily wound magnetic coils. As shown above, there are three critical elements to the design. The first is the mounting sled which is designed to fit within the in-plane coil system. This takes advantage of the relative softness of the plastic to achieve a press fit between the sled and in-plane coil system. The mounting sled design makes it possible to easily swap the package into the microscope. The sled places the centerline of the pulse coil directly beneath the microscope objective, and allows a large platform in front of the coil for easily mounting electronics packages.

The coil component is separate from the sled so that multiple coils could be partnered to a single sled for different pulse magnitudes or areas. The coil design is initially in two parts – a flat stop and thimble ("coilcore") as one component and the other matched flat stop ("coilstop") end at the other. Multiple pairs of these components were designed with different interior diameters so that different sizes of samples could be accommodated. Additionally, the coil core system is much longer than ever could be used to wind a coil. This is by design and takes advantage of the vertical layering effect of the 3D printing. Once a user selects the desired height of their coil, they attach

the stop to the core at that height. Before winding the wire around the coil, the excess center can be removed by sliding a scalpel blade in between the layers of the excess. This means that for any reasonable height of coil required, only one model need be made.

These two components combine to create the out-of-plane pulsed coil used for measurements of DMI. With the independent in-plane coilset of the microscope, and the 3D printed out-of-plane coilset, it is possible to undertake the symmetry breaking domain wall expansion measurements with a versatile system. And if a new diameter or winding of coil is required, then a new sled can be printed in about two hours, and a coilset pair in about 30 minutes.

Special Section 2:
Lithography Mask Design

Lithography design for sample fabrication is a critical step in the preparation of patterned samples. Multiple factors control the design of the lithography patterns, and care must be taken in order to ensure that the designs are suitable for the selected experimental technique. Patterned wires for transport measurements on large (8mm by 10mm) samples were optimized for large contact pads and simple contact wiring. With a single sample per substrate, these features were built to provide multiple contacts and multiple Hall cross points per sample.

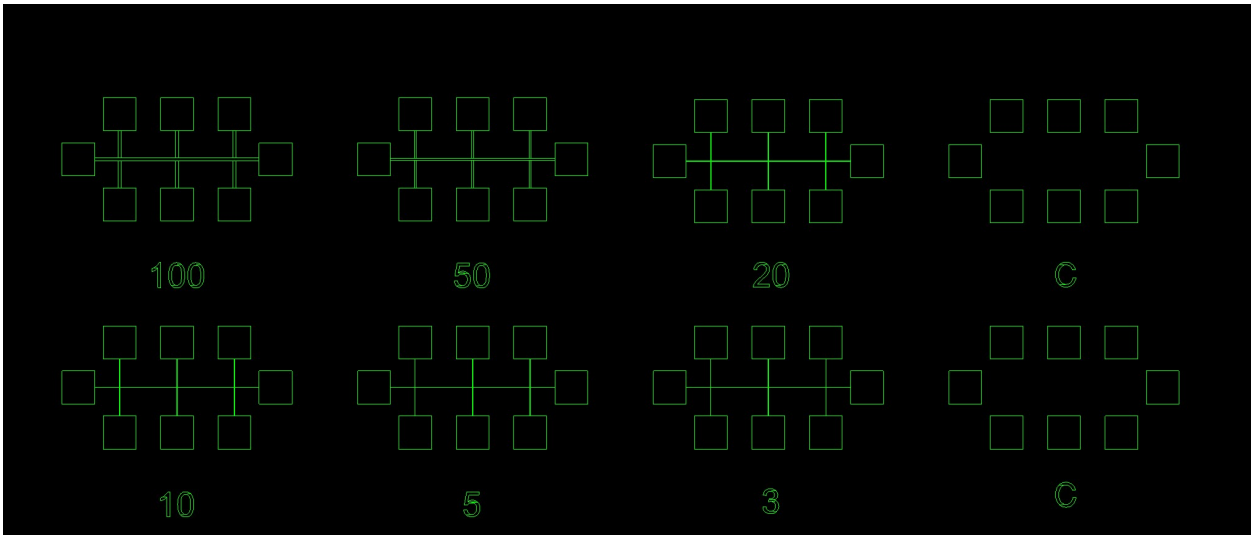

Figure 77: Standard large hall crosses for transport measurement. Wire sizes are listed below the feature in micrometers. “C” are dedicated contact pads.

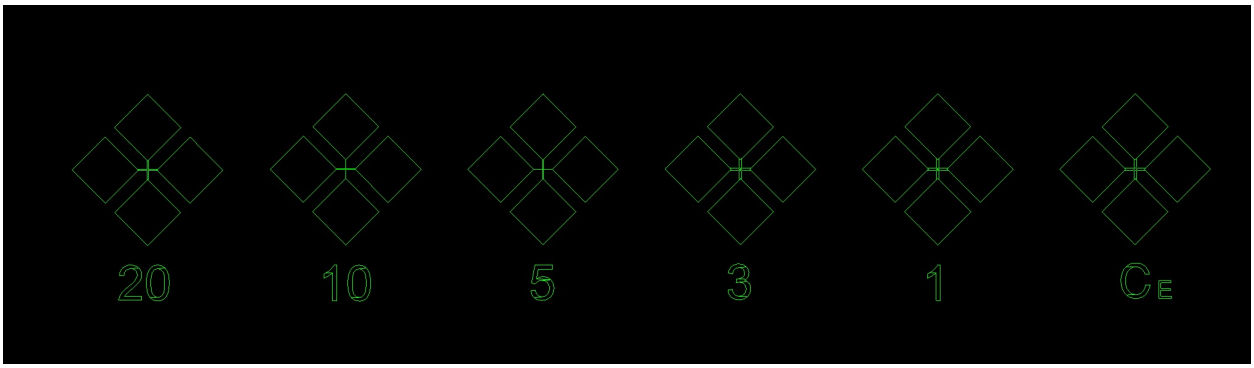

Figure 78: Small hall crosses for confined geometries and VSM sized samples. Contact pads are the same size as the larger hall crosses, but the feature is served by smaller wires that then neck down to the feature size. C is a dedicated contact.

For these patterns, the contact spacing was kept constant while the wire width was varied. Each wire is centered around the midpoint of the contact pad, with spacings at 1500 micrometers. While acceptable for large wire widths and low sample resistivity, certain small features at 10 to 1 micrometers wide could have prohibitively large device resistance. As spin orbit torque and spin transfer torque driven devices require current densities on the order of 10^8 - 10^{11} amps/cm^2 and skyrmion devices require current densities on the order of 10^4 – 10^9 amps/cm^2, this can lead to a voltage requirement that is significant for pulsed or steady current systems. In addition, pulsed current and ultrafast pulses will typically have a hardware limited voltage supply. Thus, to maintain compatibility with the contact pad geometry, a different shape with angled leads was designed.

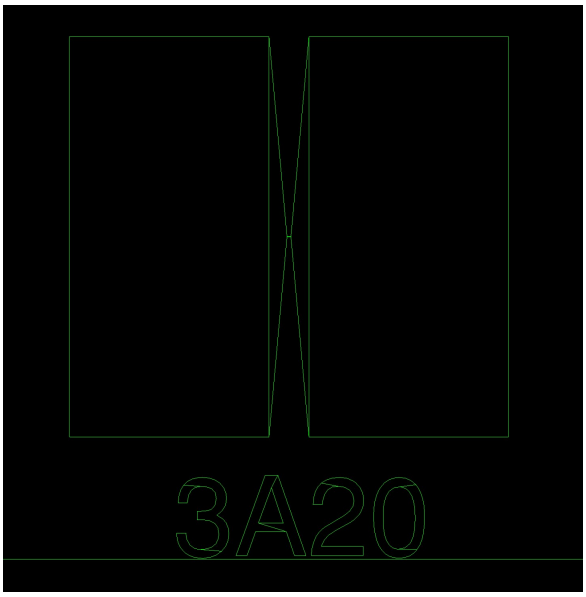

Figure 79: Angled lithography mask geometry for membrane design. This provides high current density at the choke (center) while preserving large contact pads. The angle allows for fewer sharp acute corners, reducing overall membrane stress.

While these devices were optimized for making contacts with silver paste and wire, wire bonding can also be used. However, wire bonding parameters are often material specific with poor adhesion to a range of the deposition materials. Thus, a set of contact pads compatible with all of the above device layers was designed with the intent of having a two-step deposition process. As discussed in the section on lithography and sample deposition techniques, first the sample film is deposited and lithographically defined. Then, as a second lithography and sample deposition step, a set of gold or silver conductive contacts are applied to the sample for use in either reducing device resistance or in improving contact adhesion.

Additionally, with the research done on thermal gradients in CoTb samples, there is a need for wires with a lithographically well defined choke. By applying the lessons learned from the French experiment, where engineered defect sites were used to generate hot spots, a set of thermal gradient features was designed. These features are intended to be placed either singly to a small substrate, or multiple on a large substrate. With large contact pads for ease of use as well as serving

as thermal sinks, these features range from 100 micrometers wide to 5 micrometers wide, with a choke point that ranges from 25% to 75% of the total width. In addition, feature geometry was adjusted to study the different pinning sites and effects driven by the current direction. Thus, variants exist with the choke at the midpoint and the endpoint of the wire, and the choke either from one side or both sides of the wire.

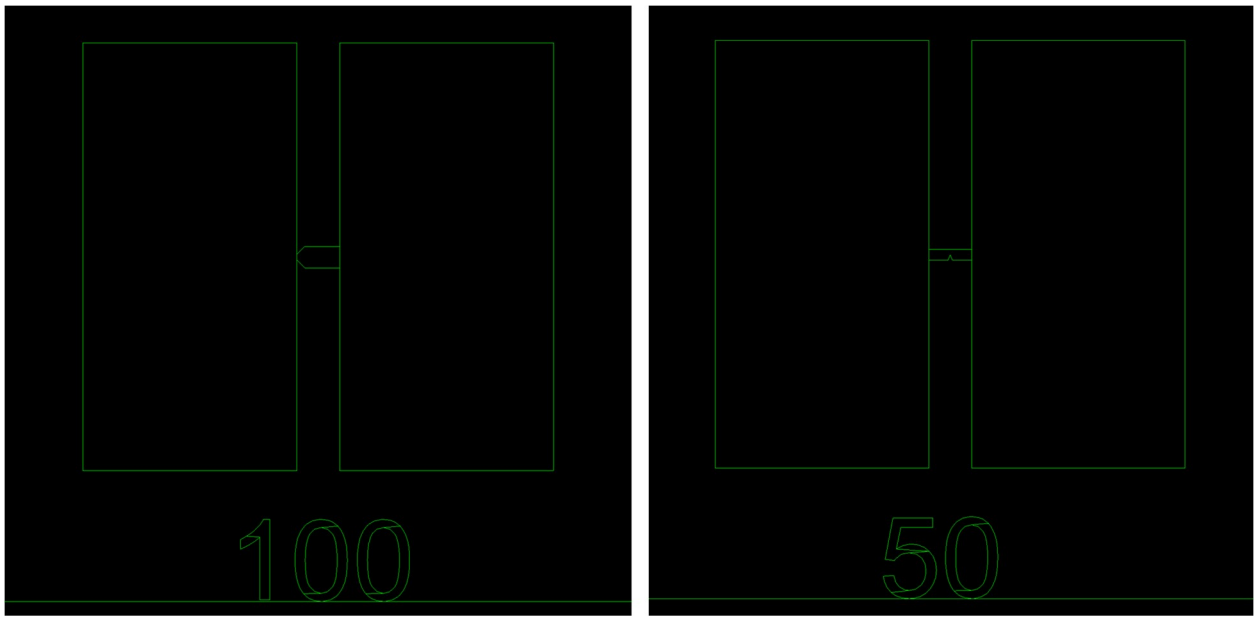

Figure 80: Sample thermal gradient chokes. These show different wire size, feature placement and feature size with 100 micrometer wire and 75% choke width located on the end of the sample (left) and a 50 micrometer wire with 50% choke width (right).

The size and positioning of the samples also makes them available for use on a silicon membrane window. Additional photomask features were designed specifically for these critical samples. For X-Ray beamline experiments, a 1mm by 1mm window is etched into a 5mm by 5mm frame. This window houses a 100 nanometer thick SiN membrane which is transparent to the X-Ray beam. This makes the beam window incredibly fragile, and is challenging for lithography. Thus, special photomask features were designed to provide good contacts for current driven experiments, while minimizing the strain of the material on the window. These patterns, as shown below were also optimized for quick and easy alignment on the windows and a minimized strain

on the membrane itself. For large current densities patterns similar to the thermal gradient patterns are used with large, high conductivity areas necked down to higher current density zones.

In systems with current or field based issues, smaller devices will yield higher returns. However, there are several major considerations. First, the smaller the device, the more difficult it will be to make electrical contact. Having large contact pads will help reduce the need for wire bonding, and can allow the system to be contacted by either pogo pins or silver paste and wire.

Conclusion:

This dissertation highlights the richness of the phenomena observed in meso-scale magnetic systems and the manipulation of these systems by controls including structure, light, heat, electric current, spin current, and magnetic field.

Thermally induced changes in magnetization in ferrimagnetic systems create new opportunities for control over domain walls. Cobalt-Terbium multilayers and alloys, also evaluated for optically induced control of magnetization, show interesting compensation controlled thermal effects. These effects, linked to the exchange of dominance of sublattices in the material can be used to controllably propagate domain walls within the material under applied field.

Novel magnetic structures in thin-film multilayer systems allow for the observation of skyrmions. Platinum/Cobalt/Osmium/Platinum thin magnetic films, evaluated as a structure to create chiral magnetic domain walls via the Dzyaloshinskii-Moriya interaction, also show the presence of skyrmions at the spin reorientation transition of the material. These skyrmions exhibit a host of interesting heat and current driven effects, allowing for observations of skyrmion nucleation and propagation behavior via Kerr microscopy.

In conclusion, the discoveries and observations outlined here in this dissertation expand the range of knowledge of magnetism and magnetic materials. The control of magnetism and magnetic textures has been of significant importance for the development of the information age, and will continue to drive data storage and processing for years to come.

Special Section X:
Quick Reference Card

Photolithography NR9 Conditions (Standard substrate)

Spin 1 minute 4500 RPM, Accel 1000
Bake 150C 1 minute
Expose 13sec, Hard contact mode
Bake 100C 1 minute
Develop 13sec Futurrex RD6 developer, rinse 13 sec water.
Dry

Photolithography NR9 Conditions (SiN Membrane)

Attach to larger sacrificial substrate
Spin 1 minute 4500 RPM, Accel 1000
Bake 150C 1 minute 30 seconds
Expose 13sec, Hard contact mode
Bake 100C 1 minute 30 seconds
Develop 13sec Futurrex RD6 developer, rinse 13 sec water.
Dry (GENTLY), once out of cleanroom, remove from substrate

THANKS TO THE READER

"Because he said he would."

BIBLIOGRAPHY

[1] F. Hellman, A. Hoffman, Y. Tserkovnyak, G. S. D. Beach, E. E. Fullerton, C. Leighton, A. H. MacDonald, D. C. Ralph, D. A. Arena, H. A. Durr, P. Fischer, J. Grollier, J. P. Heremans, T. Jungwirth, A. G. Kimel, B. Koopmans, I. N. Krivorotov, S. J. May, A. K. Petford-Long, J. M. Rondinelli, N. Samarth, I. K. Schuller, M. D. Stiles, O. Tchernyshoyov, A. Thiaville and B. L. Zink, "Interface-Induced phenomena in magnetism," *REVIEWS OF MODERN PHYSICS,* vol. 89, 2017.

[2] M. A. Ruderman and C. Kittel, "Indirect Exchange Coupling of Nuclear Magnetic Moments by Conduction Electrons," *Phys. Rev.,* vol. 96, p. 99, 1954.

[3] A. Hubert and R. Schäfer, Magnetic Domains: The Analysis of Magnetic Microstructures, Heidelberg: Springer, Berlin, Heidelberg, 1998.

[4] F. Hund, "Zur deutung der Molekelspektren," *I. Z. Phys.,* vol. 40, p. 742–764, 1927.

[5] H. A. Lorentz, "La Théorie electromagnétique de Maxwell et son application aux corps mouvants," *Archives néerlandaises des sciences exactes et naturelles,* vol. 25, pp. 363-552, 1892.

[6] I. Dzyaloshinsky, "A Thermodynamic Theory of "Weak" Ferromagnetism of Antiferromagnetics," *J. Phys. Chem. Solids,* vol. 4, pp. 241-255, 1958.

[7] T. Moriya, "Anisotropic superexchange interaction and weak ferromagnetism," *Phys Rev,* vol. 120, pp. 91-98, 1960.

[8] P. Weiss, "La variation du ferromagnetisme du temperature," *Comptes Rendus,* vol. 143, pp. 1136-1149, 1906.

[9] C. Kittel, "Theory of the Structure of Ferromagnetic Domains in Films and Small Particles," *Physical Reveiw,* vol. 70, no. 11,12, pp. 965-971, 1946.

[10] K. Wasa, M. Kitabatake and H. Adachi, Thin Films Materials Technology: Sputtering of Compound Materials, Norwich, NY: William Andrew Publishing, 2004.

[11] S. Foner, "Versatile and Sensitive Vibrating-Sample Magnetometer," *Review of Scientific Instruments, Volume 30, Issue 7,* pp. 548-557, 1959.

[12] D. O. Smith, "Development of a VIbrating Coil Magnetometer," *Rev. Sci. Instr,* vol. 27, p. 261, 1956.

[13] Quantum Design Corporation, "VersaLab Free User's manual," 2009.

[14] E. P. Lewis, The Effects Of A Magnetic Field On Radiation Memoirs By Faraday Kerr And Zeeman, New York: American Book Company, 1900.

[15] P. Weinberger, "John Kerr and his effects found in 1877 and 1878," *Philosophical Magazine Letters,* pp. 1-11, 2008.

[16] J. L. D. Kerr, "On rotation of the plane of polarization by reflection from the pole of a magnet," *The London, Edinburgh, and Dublin Philosophical Magazine and Journal of Science,* vol. 3, no. 19, pp. 321-343, 1877.

[17] S. S. P. Parkin, M. Hayashi and L. Thomas, "Magnetic domain-wall racetrack memory," *Science,* vol. 320, pp. 190-194, 2008.

[18] D. A. Allwood, G. Xiong, C. C. Faulkner, D. Atkinson, D. Petit and R. P. Cowburn, "Magnetic Domain Wall Logic," *Science,* vol. 309, p. 1688, 2005.

[19] J. D. Gurney, "Platinum Cobalt Multilayers The Next-Generation Magneto-Optic Storage Medium," *Platinum Metals Rev.,* vol. 31, p. 130, 1993.

[20] S. Mangin, M. Gottwald, C. H. Lambert, D. Steil, L. Pang, M. Hehn, S. Alebrand, M. Cinchetti, G. Malinowski, Y. Fainman, M. Aeschlimann and E. E. Fullerton, "Engineered materials for all-optical helicity-dependent magnetic switching," *Nat. Mater.,* pp. 286-292, 2014.

[21] C. D. Stanciu, F. Hansteen, A. V. Kimel, A. Kirilyuk, A. Tsukamoto, A. Itoh and T. Rasing, "All-Optical Magnetic Recording with Circularly Polarized Light," *Phys Rev. Lett,* vol. 99, p. 047601, 2007.

[22] M. S. El Hadri, P. Pirro, C. H. Lambert, S. Petit-Watelot, Y. Quessab, M. Hehn, F. Montaigne, G. Malinowski and S. Mangin, "Two types of all-optical magnetization switching mechanisms using femtosecond laser pulses," *Physical Review B,* vol. 94, p. 064412, 2016.

[23] C. D. Stanciu, F. Hansteen, A. V. Kimel, A. Kirilyuk, A. Tsukamoto, A. Itoh and T. Rasing, "All-Optical Magnetic Recording with Circularly Polarized Light," *Phys. Rev. Lett,* vol. 999, p. 047601, 2007.

[24] S. Alebrand, M. Gottwald, M. Hehn, D. Steil, M. Cinchetti, D. Lacour, E. E. Fullerton, M. Aeschlimann and S. Mangin, "Light-induced magnetization reversal of high-anisotropy TbCo alloy films," *Appl. Phys. Lett. 101,* p. 162408, 2012.

[25] R. Medapalli, I. Razdolski, M. Savoini, A. R. Khorsand, A. Kirilyuk, A. V. Kimel, T. Rasing, A. M. Kalasnikova, A. Tsukamoto and A. Itoh, "Efficiency of ultrafast laser-induced demagnetization in Gd(x)Fe(100-x-y)Co(y) alloys," *Physical Review B,* vol. 86, p. 054442, 2012.

[26] R. Moreno, T. A. Ostler, R. W. Chantrell and O. Chubykalo-Fesenko, "Conditions for thermally induced all-optical switching in ferrimagnetic alloys: Modeling of TbCo," *Physical Review B,* vol. 96, p. 014409, 2017.

[27] W. C. Thoburn, S. Legvold and F. H. Spedding, "Magnetic properties of terbium metal," *Phys. Rev.,* vol. 112, p. 56, 1958.

[28] A. V. Kimel, "All-Optical switching: Three rules of design," *Nature Materials,* vol. 13, pp. 225-226, 2014.

[29] M. Mansuripur and M. Ruane, "Mean-field analysis of amorphous rare earth-transition metal alloys for thermomagnetic recording," *IEEE Transactions on Magnetics,* vol. 22, no. 1, pp. 33-43, 1986.

[30] D. Banga and H. Awano, "Domain wall motion in Tb/Co multilayer wires with a large domain wall depinning field," *J. Appl. Physics,* vol. 115, p. 17D512, 2014.

[31] P. Hansen, C. Clausen, G. Much, M. Rosenkranz and K. Witter, "Magnetic and magneto-optical properties of rare-earth transition-metal alloys containing Gd, Tb, Fe, Co," *Jour. Appl. Phys,* vol. 66, p. 7560767, 1989.

[32] S. Alebrand, M. Gottwald, M. Hehn, D. Steil, M. Cinchetti, D. Lacour, E. E. Fullerton, M. Aeschlimann and S. Mangin, "Importance of Co in determining magnetism at room temperature in CoTb," *Appl. Phys. Lett.,* vol. 101, p. 162408, 2012.

[33] K. Ueda, M. Mann, P. W. P. de Brouwer, D. Bono and G. S. D. Beach, "Temperature dependence of spin-orbit torques across the magnetic compensation point in a ferrimagnetic TbCo alloy film," *Phys. Rev. B,* vol. 96, p. 064410, 2017.

[34] C. W. Cheng, W. Feng, G. Chern, C. M. Lee and T. Wu, "Effect of cap layer thickness on the perpendicular magnetic anisotropy in top MgO/CoFeB/Ta structures," *Journal of Applied Physics,* vol. 110, p. 033916, 2011.

[35] S. Alebrand, U. Bierbrauer, M. Hehn, M. Gottwald, O. Schmitt, D. Steil, E. E. Fullerton, S. Mangin, M. Cinchetti and M. Aeschlimann, "Subpicosecond magnetization dynamics in TbCo alloys," *Phys. Rev. B,* vol. 89, p. 144404, 2014.

[36] R. Medapalli, I. Razdolski, M. Savoini, A. R. Khorsand, A. M. Kalashnikova, A. Tsukamoto, A. Itoh, A. Kirilyuk, A. V. Kimel and T. Rasing, "The role of magnetization compensation point for efficient ultrafast control of magnetization in Gd(24)Fe(66.5)Co(9.5) alloy," *European Journal of Physics B,* vol. 86, p. 183, 2013.

[37] Y. Quessab, R. Medapalli, M. S. El Hadri, M. Hehn, G. Malinowski, E. E. Fullerton and S. Mangin, "Helicity-dependent all-optical domain wall motion in ferromagnetic thin films," *Condensed Matter (arXiv),* p. 1709.07645, 2017.

[38] N. Nagaosa and T. Yoshinori, "Topological properties and dynamics of magnetic skyrmions," *Nature Nanotechnology,* vol. 243, pp. 899-911, 2013.

[39] D. A. Allwood, G. Xiong, C. C. Faulkner, D. Atkinson, D. Petit and R. P. Cowburn, "Magnetic domain-wall logic," *Sceince,* vol. 309, p. 1688, 2005.

[40] S. Alebrand, A. Hassdenteufel, D. Steil, M. Cinchetti and M. Aeschlimann, "Interplay of heating and helicity in all-optical magnetization switching," *Phys. Rev. B,* vol. 85, p. 092401, 2012.

[41] T. A. Ostler, J. Barker, R. F. L. Evans, W. Chantrell, U. Atxitia, O. Chubykalo-Fesenko, S. El Moussaoui, L. Le Guyader, E. Mengotti, L. J. Heyderman, F. Nolting, A. Tsukamoto, A. Itoh, D. Afanasiev, B. A. Ivanov, A. M. Kalashnikova, K. Vahaplar, J. Mentink, A. Kirilyuk, T. Rasing and A. V. Kimel, "Ultrafast heating as a sufficient stimulus for magnetiztion reversal in a ferrimagnet," *Nature Communications,* vol. 3, p. 666, 2012.

[42] A. Yamaguchi, S. Nasu, H. Tanigawa, T. Ono, K. Miyake, K. Mibu and T. Shinjo, "Effect of Joule heating in current-driven domain all motion," *Appl. Phys. Lett.,* vol. 86, p. 012511, 2005.

[43] H. Nakamura, S. Li, X. Liu and A. Morisako, "Current-Induced Domain Wall Motion in TbFeCO micro wire," *Jour. Phys. Conference Series,* vol. 266, p. 012082, 2011.

[44] M. D. Stiles and A. Zangwill, "Anatomy of Spin-Transfer Torque," *Physical Review B,* vol. 66, p. 014407, 2002.

[45] A. Y. Dobin and H. J. Richter, "Domain wall assisted magnetic recording," *Applied Physics Letters,* vol. 89, p. 062512, 2006.

[46] S. D. Harkness and H. J. Richter, "Media for Magnetic Recording Beyond 100 Gbit/in.2," *Materials for Magnetic Data Storage,* vol. 31, no. 5, pp. 384-388, 2006.

[47] T. H. R. Skyrme, "A Unified Field Theory of Mesons and Baryons," *Nuclear Physics,* vol. 31, pp. 556-569, 1962.

[48] D. C. Ortuno, W. Wang, M. Beg, R. A. Pepper, M. A. Bisotti, R. Carey, M. Vousden, T. Kluyver, O. Hovorka and H. Fangohr, "Thermal stability and topological protection of skyrmions in nanotracks," *Scientific Reports,* vol. 7, p. 4060, 2017.

[49] A. Fert, V. Cros and J. Sampaio, "Skyrmions on the track," *Nature Nanotechnology,* vol. 8, pp. 152-156, 2013.

[50] J. Grollier, A. Chanthbouala, R. Matsumoto, A. Anane, V. Cros, F. N. van Dau and A. Fert, "Magnetic domain wall motion by spin transfer," *Comptes Rendus Physique,* vol. 12, no. 3, pp. 309-317, 2011.

[51] G. Yu, P. Upadhyaya, Q. Shao, H. Wu, G. Yin, X. Li, C. He, W. Jiang, X. Han, P. K. Amiri and K. L. Wang, "Room-Temperature Skyrmion Shift Device for Memory Application," *Nano Letters,* vol. 17, p. 261, 2017.

[52] X. Z. Yu, N. Kanazawa, W. Z. Zhang, T. Nagai, T. Hara, K. Kimoto, Y. Matsui, Y. Onose and Y. Tokura, "Skyrmion flow near room temperature in an ultralow current density," *Nature Comm. ,* vol. 3, p. 988, 2012.

[53] I. Kézsmárki, S. Bordács, P. Milde, E. Neuber, L. M. Eng, J. S. White, H. M. Rønnow, C. D. Dewhurst, M. Mochizuki, K. Yanai, H. Nakamura, D. Ehlers, V. Tsurkan and A. Loidl, "Néel-type skyrmion lattice with confined orientation in the polar magnetic semiconductor GaV4S8," *Nature Materials,* vol. 14, pp. 1116-1122, 2015.

[54] W. Jiang, X. Zhang, G. Yu, W. Zhang, X. Wang, M. B. Jungfleisch, J. E. Pearson, X. Cheng, O. Heinonen, K. L. Wang, Y. Zhou and A. Hoffman, "Direct observation of the skyrmion Hall effect," *Nature Physics,* vol. 13, pp. 162-169, 2017.

[55] D. Liang, J. P. DeGrave, M. J. Stolt, Y. Tokura and S. Jin, "Current-driven dynamics of skyrmions stabilized in MnSi nanowires revealed by topological Hall effect," *Nature Communication,* vol. 6, p. 8217, 2015.

[56] A. Neubauer, C. Pfleiderer, B. Binz, A. Rosch, R. Ritz, P. G. Niklowitz and P. Boni, "Topological Hall effect in the A phase of MnSi.," *Phys. Rev. Lett,* vol. 102, p. 186602, 2009.

[57] C. Pappas, E. Lelièvre-Berna, P. Falus, P. M. Bentley, E. Moskvin, S. Grigoriey, P. Fouquet and B. Farago, "Chiral paramagnetic skyrmion-like phase in MnSi," *Phys. Rev. Lett.,* vol. 102, p. 197202, 2009.

[58] S. D. Pollard, J. A. Garlow, J. Yu, Z. Wang, Y. Zhu and H. Yang, "Observation of stable Néel skyrmions in cobalt/palladium multilayers with Lorentz transmission electron microscopy," *Nature Communications,* vol. 8, p. 14761, 2017.

[59] S. Heinze, K. von Bergmann, M. Menzel, J. Brede, A. Kubetzka, R. Wiesendanger, G. Bihlmayer and S. Blügel, "Spontaneous atomic-scale magnetic skyrmion lattice in two dimensions," *Nature Physics,* vol. 7, pp. 713-718, 2011.

[60] S. Heinze, K. von Bergmann, M. Menzel, J. Brede, A. Kubetzka, R. Wiesendanger, G. Bihlmayer and S. Blügel, "Spontaneous atomic-scale magnetic skyrmion lattice in two dimensions," *Nature Physics,* vol. 7, pp. 713-718, 2011.

[61] S. Mühlbauer, B. Binz, F. Jonietz, C. Pfleiderer, A. Rosch, A. Neubauer, R. Georgii and P. Böni, "Skyrmion Lattice in a Chiral Magnet," *Science,* vol. 323, no. 5916, pp. 915-919, 2009.

[62] A. Neubauer, C. Pfleiderer, B. Binz, A. Rosch, R. Ritz, P. G. Niklowitz and P. Böni, "Topological Hall Effect in the A Phase of MnSi," *Physical Review Letters,* vol. 102, p. 186602, 2009.

[63] C. Pappas, E. Lelièvre-Berna, P. Falus, P. M. Bentley, E. Moskvin, S. Grigoriev, P. Fouquet and B. Farago, "Chiral Paramagnetic Skyrmion-like Phase in MnSi," *Physical Review Letters,* vol. 102, p. 197202, 2009.

[64] X. Z. Yu, Y. Onose, N. Kanazawa, J. H. Park, J. H. Han, Y. Matsui, N. Nagaosa and Y. Tokura, "Real-space observation of a two-dimensional skyrmion crystal," *Nature,* vol. 465, pp. 901-904, 2010.

[65] W. Münzer, A. Neubauer, T. Adams, S. Mühlbauer, C. Franz, F. Jonietz, R. Georgii, B. Pedersen, M. Schmidt, A. Rosch and C. Pfleiderer, "Skyrmion lattice in the doped semiconductor Fe1-xCoxSi," *Physical Review B,* vol. 81, p. 041203(R), 2010.

[66] X. Z. Yu, N. Kanazawa, Y. Onose, K. Kimito, W. Z. Zhang, S. Ishiwata, Y. Matsui and Y. Tokura, "Near room-temperature formation of a skyrmion crystal in thin-films of the helimagnet FeGe," *nature materials,* vol. 10, pp. 106-109, 2011.

[67] S. X. Huang and C. L. Chien, "Extended Skyrmion Phase in Epitaxial FeGe(111) Thin Films," *Physical Review Letters,* vol. 108, p. 267201, 2012.

[68] S. Seki, X. Z. Yu, S. Ishiwata and Y. Tokura, "Observation of skyrmions in a multiferroic material," *Science,* vol. 336, pp. 198-201, 2012.

[69] I. Raičević, D. Popović, C. Panagopoulos, L. Benfatto, M. B. Silva Neto, E. S. Choi and T. Sasagawa, "Skyrmions in a Doped Antiferromagnet," *Physical Review Letters,* vol. 106, p. 227206, 2011.

[70] A. Fert, "Magnetic and transport properties of metallic multilayers," *Materials Science Forum,* Vols. 59-60, pp. 439-480, 1990.

[71] S. Heinze, K. von Bergmann, M. Menzel, J. Brede, A. Kubetzka, R. Wiesendanger, G. Bihlmayer and S. Blügel, "Spontaneous atomic-scale magnetic skyrmion lattice in two dimensions," *nature physics,* vol. 7, pp. 713-718, 2011.

[72] G. Chen, A. Mascaraque, A. T. N'Diaye and A. K. Schmid, "Room temperature skyrmion ground state stabilized through interlayer exchange," *Appl. Phys. Lett,* vol. 106, p. 242404, 2015.

[73] G. Yu, P. Upadhyaya, X. Li, W. Li, S. Kwon Kim, Y. Fan, K. L. Wong, Y. Tserkovnyak, P. Khalili Amiri and K. L. Wang, "Room-Temperature Creation and Spin−Orbit Torque Manipulation of skyrmions in thin films with engineered asymmetry," *Nanoletters,* vol. 16, pp. 1981-1988, 2016.

[74] D. Maccariello, W. Legrand, N. Reyren, K. Garcia, K. Bouzehouane, S. Collin, V. Cros and A. Fert, "Electrical signature of individual magnetic skyrmions in multilayered systems," *Arxiv,* p. 1706.05809v1, 2017.

[75] K. Zeissler, K. Shahbazi, J. Massey, S. Finizio, J. Raabe, F. Al Ma'Mari, M. C. Rosamond, E. H. Linfield, T. A. Moore, G. Burnell and C. H. Marrows, "Direct Imaging and Electrical Detection at Room Temperature of a Single Skyrmion," *arxiv,* p. 1706.06024, 2017.

[76] R. Tomasello, M. Ricci, P. Burrascano, V. Puliafito, M. Carpentieri and G. Finocchio, "Electrical detection of single magnetic skyrmion at room temperature," *AIP Advances,* vol. 7, p. 056022, 2017.

[77] B. Dupé, M. Hoffman, C. Paillard and S. Heinze, "Tailoring magnetic skyrmions in ultra-thin transition metal films," *Nature Communications,* vol. 5, p. 4030, 2014.

[78] H. Yang, A. Thiaville, S. Rohart, A. Fert and M. Chshiev, "Anatomy of Dzyaloshinskii-Moriya Interaction at Co/Pt Interfaces," *Phys. Rev. Lett.,* vol. 115, p. 267210, 2015.

[79] I. Gross, L. J. Martinez, J. P. Tetienne, T. Hingant, J. F. Roch, K. Garcia, R. Soucaille, J. P. Adam, J. V. Kim, S. Rohart, A. Thiaville, J. Torrejon, M. Hayashi and V. Jacques, "Direct measurement of interfacial Dzyaloshinskii-Moriya interaction in X [CoFeB] MgO heterostructures with a scanning NV magnetometer (X= Ta, TaN, and W)," *Physical Review B,* vol. 94, p. 064413, 2016.

[80] W. Jiang, P. Upadhyaya, W. Zhang, G. Yu, M. B. Jungfleisch, F. Y. Fradin, J. E. Pearson, Y. Tserkovnyak, K. L. Wang, O. Heinonen, S. G. E. te Velthuis and A. Hoffman, "Magnetism. Blowing magnetic skyrmion bubbles.," *Science,* vol. 349, p. 283, 2015.

[81] N. H. Kim, D. S. Han, J. Jung, K. Park, H. J. M. Swagten, J. S. Kim and C. Y. You, "Dependence of interfacial Dzyaloshinskii–Moriya interaction and perpendicular magnetic anisotropy on the thickness of the heavy-metal layer," *Applied Physics Express,* vol. 10, p. 103003, 2017.

[82] S. Woo, K. Litzius, B. Krüger, M. Y. Im, L. Caretta, K. Richter, M. Mann, A. Krone, R. M. Reeve, M. Weigand, P. Agrawal, I. Lemesh, M. A. Mawass, P. Fischer, M. Kläui and G. S. D. Beach, "Observation of room-temperature magnetic skyrmions and their current-driven dynamics in ultrathin metallic ferromagnets," *Nature Materials,* vol. 15, pp. 501-506, 2016.

[83] C. Moreau-Luchaire, C. Moutafis, N. Reyren, J. Sampaio, C. A. F. Vaz, N. Van Horne, K. Bouzehouane, K. Garcia, C. Deranlot, P. Warnicke, P. Wohlhüter, J. M. George, M. Weigand, J. Raabe, V. Cros and A. Fert, "Additive interfacial chiral interaction in multilayers for stabilization of small individual skyrmions at room temperature," *Nature Nanotechnology,* vol. 11, pp. 444-448, 2016.

[84] K. Yamamoto, A.-M. Pradipto, K. Nawa, T. Akiyama, T. Ito, T. Ono and K. Nakamura, "Interfacial Dzyaloshinskii-Moriya interaction and orbital magnetic moments of metallic multilayer films," *AIP Advances,* vol. 7, p. 056302, 2017.

[85] A. Fert and P. M. Levy, "Role of Anisotropic Exchange Interactions in Determining the Properties of Spin-Glasses," *Phys. Rev. Lett.,* vol. 44, p. 1538, 1980.

[86] A. Soumyanarayanan, N. Reyren, A. Fert and C. Panagopoulos, "Emergent phenomena induced by spin–orbit coupling at surfaces and interfaces," *Nature,* vol. 539, pp. 509-517, 2016.

[87] A. W. J. Wells, P. M. Shepley, C. H. Marrows and T. A. Moore, "Effect of interfacial intermixing on the Dzyaloshinskii-Moriya interaction in Pt/Co/Pt," *Physical Review B,* vol. 2017, p. 054428, 2017.

[88] A. Soumyanarayanan, M. Raju, A. L. Gonzalez Oyarce, A. K. C. Tan, M. Y. Im, A. P. Petrovic, P. Ho, K. H. Khoo, M. Tran, C. K. G, F. Ernult and C. Panagopoulos, "Tunable room-temperature magnetic skyrmions in Ir/Fe/Co/Pt multilayers," *Nature Materials,* vol. 16, pp. 898-904, 2017.

[89] A. L. Balk, K. W. Kim, D. T. Pierce, M. D. Stiles, J. Unguris and S. M. Stavis, "Simultaneous control of the Dzyaloshinskii-Moriya interaction and magnetic anisotropy in nanomagnetic trilayers," *Phys. Rev. Lett.,* vol. 119, p. 077205, 2017.

[90] J. Yu, X. Qiu, Y. Wu, J. Yoon, P. Deorani, J. M. Besbas, A. Manchon and H. Yang, "Spin orbit torques and DzyaloshinskiiMoriya interaction in dual-interfaced Co-Ni multilayers," *Scientific Reports,* vol. 6, p. 32629, 2016.

[91] S. G. Je, D. H. Kim, S. C. Yoo, B. C. Min, K. J. Lee and S. B. Choe, "Asymmetric magnetic domain-wall motion by the Dzyaloshinskii-Moriya interaction," *Physical Review B,* vol. 88, p. 214401, 2013.

[92] F. Ajejas, V. Křižáková, D. de Souza Chavez, J. Vogel, P. Perna, R. Gurrero, A. Gudin, J. Camarero and S. Pizzini, "Tuning domain wall velocity with Dzyaloshinskii-Moriya interaction," *Appl. Phys. Lett,* vol. 2017, p. 202402, 2017.

[93] E. Jue, C. K. Safeer, M. Drouard, A. Lopez, P. Balint, L. Buda-Prejbeanu, O. Boulle, S. Auffret, A. Schuhl, A. Manchon, I. Mihai Miron and G. Gaudin, "Chiral damping of magnetic domain walls," *Nature Materials,* vol. 15, pp. 272-277, 2016.

[94] M. Vanatka, J. C. Rojas-Sanchez, J. Vogel, M. Bonfim, M. Belmeguenai, Y. Roussigne, A. Stashkevitch, A. Thiaville and S. Pizzini, "Velocity asymmetry of Dzyaloshinskii domain walls in the creep and flow regimes," *Journal of Physics: Condensed Matter,* vol. 27, no. 32, 2015.

[95] I. Lemesh, F. Büttner and G. S. D. Beach, "Accurate model of the stripe domain phase of perpendicularly magnetized multilayers," *Phys. Rev. B,* vol. 95, p. 174423, 2017.

[96] J. E. Bidaux and B. Cao, "Elastic behavior of pure cobalt near the spin-reorientation phase transition”," *J. Phys: Condens. Matter ,* vol. 3, p. 2263, 1991.

[97] S. Lin, "Edge instability in a chiral stripe domain under an electric current and skyrmion generation," *Physical Review B,* vol. 94, p. 020402(R0, 2016.

[98] S. Z. Lin, C. Reichhardt, C. D. Batista and A. Saxena, "Particle model for skyrmions in metallic chiral magnets: Dynamics, pinning, and creep," *Phys. Rev. B,* vol. 87, p. 214419, 2013.

[99] A. Hrabec, J. Sampiao, M. Belmeguenai, I. Gross, R. Weil, S. M. Cherif, A. Stashkevich, V. Jacques, A. Thiaville and S. Rohart, "Current-induced skyrmion generation and dynamics in symmetric bilayers," *Nature Communications,* vol. 8, p. 25765, 2017.

[100] S. Emori, U. Bauer, S. Woo and G. S. D. Beach, "Large voltage-induced modification of spin-orbit torques in Pt/Co/GdOx," *Appl. Phys. Lett.,* vol. 105, p. 222401, 2014.

[101] W. Jiang, G. Chen, K. Liu, J. Zang, S. G. E. te Velthuis and A. Hoffman, "Skyrmions in magnetic multilayers," *Physics Reports,* vol. 704, pp. 1-49, 2017.

[102] G. S. Lim, T. C. Huang, D. C. Bullock and G. Castillo, "X-ray structures and magnetic properties of sputtered osmium-doped iron oxide thin films," *J. Appl. Phys. ,* vol. 59, p. 3543, 1986.

[103] R. Soucaille, M. Belmeguenai, J. Torrejon, J. V. Kim, T. Devolder, Y. Roussigné, S. M. Chérif, A. A. Stashkevitch, M. Hayashi and J. P. Adam, "Probing the Dzyaloshinskii-Moriya interaction in CoFeB ultrathin films using domain wall creep and Brillouin light spectroscopy," *Physical Review B,* vol. 94, p. 104431, 2016.